Atomic Scale Characterizations

of Two-dimensional Anisotropic Materials

and Their Heterostructures

by

Bin Chen

A Dissertation Presented in Partial Fulfillment
of the Requirements for the Degree
Doctor of Philosophy

Approved July 2018 by the
Graduate Supervisory Committee

Sefaattin Tongay, Chair
Mariana Bertoni
Lan-Yun Chang

ARIZONA STATE UNIVERSITY
August 2018

ABSTRACT

There has been a surge in two-dimensional (2D) materials field since the discovery of graphene in 2004. Recently, a new class of layered atomically thin materials that exhibit in-plane structural anisotropy, such as black phosphorous, transition metal trichalcogenides and rhenium dichalcogenides (ReS_2), have attracted great attention. The reduced symmetry in these novel 2D materials gives rise to highly anisotropic physical properties that enable unique applications in next-gen electronics and optoelectronics. For example, higher carrier mobility along one preferential crystal direction for anisotropic field effect transistors and anisotropic photon absorption for polarization-sensitive photodetectors.

This dissertation endeavors to address two key challenges towards practical application of anisotropic materials. One is the scalable production of high quality 2D anisotropic thin films, and the other is the controllability over anisotropy present in synthesized crystals. The investigation is focused primarily on rhenium disulfide because of its chemical similarity to conventional 2D transition metal dichalcogenides and yet anisotropic nature. Carefully designed vapor phase deposition has been demonstrated effective for batch synthesis of high quality ReS_2 monolayer. Heteroepitaxial growth proves to be a feasible route for controlling anisotropic directions. Scanning/transmission electron microscopy and angle-resolved Raman spectroscopy have been extensively applied to reveal the structure-property relationship in synthesized 2D anisotropic layers and their heterostructures.

DEDICATION

To Xiwu Chen and Shufang Zhuang.

(献给我的父亲母亲)

ACKNOWLEDGMENTS

I am greatly indebted to my advisor and mentor, Professor Sefaattin Tongay, for his continuous support through the past four years. To thank only for his guidance to academic research is an extreme unfairness. His humorous, positive, and creative attitude towards life influences me the most: I see a passion for science and a love for life in him.

It is an honor and luxury for me to be one of the very first generation of PhDs under his guidance. I still remember the days when there were only four of us (Hui, Kedi and me being students). Sef would not mind playing around with screw drivers and wrenches to help setup equipment in lab. A typical Friday afternoon back then consisted of constructive discussions and delicious snacks in his cozy office (read: group meeting). Now it is a group of more than 10 people that maintains the friendly yet productive atmosphere. It has been a wonderful PhD experience (Sef's parties definitely help).

I am grateful to all who I had the pleasure to work with and make this dissertation possible. Each of my committee member has contributed extensive professional and personal guidance. I would like to thank Prof. Shery Chang for her training/teaching me TEM and correcting my numerous mistakes (and authentic homemade Chinese cakes for lunar new year). I also express my gratitude to Prof. Bertoni for her insight into defects in semiconductors and help for my research and career development. I shall give credits to professionals at Eyring Materials Center: Diana Convey, Katia March, Ken Mossman, Manuel Roldan Gutierrez, Toshihiro Aoki, Emmanuel Soignard and Karl Weiss for their help of various fabrication and characterization expertise. I am grateful to collaborators both here at ASU and those around the world.

My acknowledgements also go to my friends at ASU, some of whom happen to be collogues in lab: Hui, Kedi, Sijie, Anupum, Xifan, Wilson, Ashutosh, Ying, Mark, Yuxia, Xiaodong, Meng, Bohan, Shaohao, Shaojiang, Jiuhao, Hanxiao, Duoli, Ximo, Sihan, Penghong and many others. Indeed, it would be much more difficult for one to face challenges in life without support from good friends. I want to say thank you to my best friend Yiwang for his support since high school (can't believe it has been ten years now!).

I would like to thank my undergrad advisor, Dr. Teng Zhang. He has been an inspiring figure for me and leads me into the world of academia. In addition, I wish to appreciate helps from professors and friends at my undergrad school, especially during my PhD program application, without which I would most likely not be here writing my dissertation.

Mostly importantly, I would like to thank my parents and my lovely girlfriend for their consistent love and caring. They are willing to do whatever they can to help me get through difficult moments in my life. I wouldn't have made it so far without their support and I can't thank them enough.

Last but not least, thanks to all who take time to read this dissertation.

TABLE OF CONTENTS

Page

ABSTRACT ..... **i**

DEDICATION ..... **ii**

ACKNOWLEDGMENTS ..... **iii**

LIST OF FIGURES ..... **ix**

CHAPTER

Chapter 1 Introductions **1**

1.1 The Rise of 2D Materials **1**

1.1.1 Graphene 2
1.1.2 TMDCs 3

1.2 Defects in 2D Layers **4**

1.2.1 Point Defects 5
1.2.2 Line Dislocations and Grain Boundaries 7

1.3 Heterostructures of 2D Monolayers **8**

1.4 Pseudo–1D Materials **9**

1.4.1 Black Phosphorus and Tellurium 10
1.4.2 Transition Metal Trichalcogenides MX_3 12
1.4.3 Anisotropic TMDC ReX_2 13

1.5 Discussions and Scope of this Dissertation **23**

1.5.1 Challenges for Anisotropic Materials 24

CHAPTER **Page**

Chapter 2 Review of Experimental Techniques..... 27

2.1 Materials Fabrication.....27

2.1.1 Mechanical Exfoliation 27
2.1.2 Vapor Phase Synthesis 28

2.2 Optical Characterizations.....29

2.2.1 Raman Spectroscopy 29
2.2.2 Photoluminescence Spectroscopy 32

2.3 Electron Microscopy Characterizations.....34

2.3.1 Scanning/Transmission Electron Microscopy 34
2.3.2 Practical Resolution of Electron Microscope 36
2.3.3 Electron Beam Radiation Damage 36
2.3.4 Sample Preparation 40
2.3.5 Structural Analysis 42
2.3.6 Chemical Analysis.....45

2.4 Atomic Force Microscopy.....48

Chapter 3 Architecture and Anisotropy in CVD ReS_2..... 50

3.1 Introduction 50

3.2 Experimental Details.....51

3.2.1 Electron Microscopy Characterizations 52
3.2.2 Raman Spectroscopy 53
3.2.3 AFM characterizations 53

3.3 Results.....53

3.3.1 Growth Characteristics 53
3.3.2 Effect of Growth Conditions 55
3.3.3 Architecture and Orientation of Subdomains 58

CHAPTER **Page**

3.3.4 STEM Characterizations of Grain Boundaries....62
3.3.5 Effects of Defects on Anisotropy....65

3.4 Discussions....66

Chapter 4 Rhenium Disulfide/Tungsten Disulfide Heterostructures....67

4.1 Introduction....67

4.2 Experimental Details....69

4.2.1 Materials Growth....69
4.2.2 Roman Spectroscopy....70
4.2.3 STEM and EELS Measurements....71

4.3 Results....72

4.3.1 Growth Characteristics....72
4.3.2 Microscale Look and EELS Measurements....76
4.3.3 Atomic Scale Structural Studies....77
4.3.4 Highly Anisotropic Response of Pseudo-1D ReS_2 in Lateral Junction....79
4.3.5 Size Dependent Anisotropy in Vertical Heterostructures....81

4.4 Discussions....83

Chapter 5 Tellurium/2D Layer Heterostructures....85

5.1 Introduction....85

5.2 Experimental Details....86

5.2.1 Synthesis of Tellurium....86
5.2.2 Raman Spectroscopy....87
5.2.3 Microscopy Characterization....87

5.3 Results....88

5.3.1 Synthesis and Growth Characteristics....88

CHAPTER **Page**

5.3.2 Cross-sectional TEM and Tellurium Orientation 91

5.4 Discussions 94

Chapter 6 Summary and Future Directions 97

6.1 Summary 97

6.2 Future Directions 98

6.2.1 Interface Structure and its Reliability 98
6.2.2 Interface Diffusion 98
6.2.3 Substrate Effects 99

REFERENCES 100

LIST OF FIGURES

FIGURE **Page**

Figure 1-1 **a.** Atomic structure of graphene and **b.** its electronic band structure showing a linear dispersion at K point. 2

Figure 1-2 **a.** The structure of MX_2 and **b.** band structure of MoS_2 showing indirect to direct transition at monolayer limit..... 3

Figure 1-3 Stone Wales defect SW(55-77), formed by rotating a carbon carbon bond by 90°. **a.** Experimental TEM image of the defect and **b.** its atomic structure as obtained from DFT calculations..... 5

Figure 1-4 **a.** Single vacancy 5|9 rings seen in an experimental TEM image. **b.** its atomic structure obtained from DFT calculations. 5

Figure 1-5 Experimental ADF STEM image of vacancies and antisite defects in MoS_2. 6

Figure 1-6 HR TEM images of grain boundaries in graphene..... 7

Figure 1-7 **a.** Tilt boundary in MoS_2 with an 18.5° angle. **b.** 5|7 and **c.** 6|8 dislocations taken from a. **d.** Pristine and **e.** molybdenum substituted 4|6 dislocations observed in tilt boundaries, respectively. 8

Figure 1-8 Schematic representation of heterojunctions between monolayers of two different transition metal dichalcogenides, for example, between MoS_2 and WS_2. Mo, W and S atoms are represented by green, pink and yellow spheres, respectively. **a.** WS_2 can grow on top of MoS_2. or **b.** laterally from MoS_2. 9

FIGURE **Page**

Figure 1-9 **a.** The structure of black phosphorus and **b.** anisotropic DC conductivity. 10

Figure 1-10 Schematic showing the crystal structure and electronic structures of tellurium. **a.** Spiral chains of the crystals arrange in a crystal structure. **b.** View along the c-axis indicating spiral chains of Te atomic structures with an angle of 120°. **c.** electronic band structures and total density of states (DOS) of tellurium. **d.** The XRD pattern spectrum of Te nanostructures. 11

Figure 1-11 **a.** Tilted side view of a ball and stick model of a single layer of MX_3. M and X atoms are denoted by green and yellow spheres, respectively. The dotted black line represents the primitive monoclinic cell. And the blue trigonal prisms represent the chain. **b.** stacked layers of bulk MX_3 as seen from the *b* axis. 12

Figure 1-12 **a.** The structure of ReX_2 and **b.** Anisotropic (Re-chain) direction probed by angle-resolved Raman spectroscopy and STEM. 13

Figure 1-13 Periodic table for two-dimensional layered van der Waals transition metal dichalcogenides. 14

Figure 1-14 Three typical phases: 2H, 1T and 1T' (distorted 1T) of TMDCs. 14

Figure 1-15 Distorted 1T phase in WTe_2, where grey and yellow atoms are tungsten and tellurium atoms, respectively. **a.** Top view showing the basal plane with W-Te bonding. and **b.** showing only zigzag bonding between neighboring tungsten atoms. 15

FIGURE **Page**

Figure 1-16 Basal plane of ReS_2 monolayer showing **a.** Re-S bonding and **b.** only Re-Re bonding. Diamond-shape repeating units is formed by four Re atoms as linear chains. 16

Figure 1-17 Calculated energy for common TMDC monolayers in 2H, 1T and 1T' structures. 16

Figure 1-18 Calculated band structure of $ReSe_2$. **a.** octahedral structure (2H) and **b.** trigonal prismatic structure (1T). 17

Figure 1-19 Orbital states. Partial density of states of **a.** 2H- and **b.** 1T'- monolayer MoS_2. Isosurface (0.003 e/$Å^3$) of the charge distributions of **c.** 2H- and **e.** 1T'- MoS_2 doped with 1.00 e/f.u. Within crystal field theory, the Mo 4d orbitals **d.** D_{3h}- and **f.** O_h-MoS_6 unit will split into three and two groups, respectively. 18

Figure 1-20 **a.** Calculated electronic band structures and density of states for 1T' MoS_2. **b.** band structure of WTe_2 19

Figure 1-21 **a.** band structure of bulk (red solid line) and monolayer (magenta dash line). **b.** Energy of the system as a function of interlayer distance. 20

Figure 1-22 Raman spectra of thin layer and bulk ReS_2, with 18 Raman active peaks labeled. 21

Figure 1-23 Annular dark-field scanning transmission electron microscopy (ADF-STEM) of bulk to monolayer ReS_2. **a.** Low magnification STEM image of ReS_2 sample on a TEM grid. Inset: optical micrograph of sample on PDMS before transfer. **b.** Medium magnification ADF-STEM image of

FIGURE **Page**

suspended ReS_2 where the sample tore during the transfer process. **c.** High-magnification ADF-STEM image of a few-layer region. **d.** Polarization- and orientation-resolved Raman spectra of bulk region. White double arrows depict direction of rhenium chains in a-c. 22

Figure 1-24 **a.** Differential reflectance spectra of monolayer ReS_2 with varied incident laser polarization angles. **b.** Excitonic transition energies are exacted out and plotted as function laser polarizations. **c.** photoluminescence spectra of ReS_2 with varied thickness. 23

Figure 2-1 Tape exfoliation process for monolayers from bulk crystals. 27

Figure 2-2 CVD system setup and optical images of grown MoS_2 monolayer on SiO_2/Si substrates..... 28

Figure 2-3 Energy level of diatom molecule model. 29

Figure 2-4 Raman spectrum showing Rayleigh, anti-Stokes and Stokes scattering lines. 30

Figure 2-5 **a.** Renishaw InVia spectrometer setup and **b.** Rotary stage for anisotropic measurements. 31

Figure 2-6 Schematic of luminescence in a solid. 32

Figure 2-7 Band diagrams of direct gap semiconductor and indirect gap semiconductor. 33

Figure 2-8 **a.** Improvement of resolving power by developing electron microscopes over the years. **b.** Aberration-corrected FEI Titan TEM and **c.** NION UltraSTEM 100. 35

FIGURE **Page**

Figure 2-9 The maximum transferable energy for a range of atoms as a function of the displacement-threshold energy. 37

Figure 2-10 Scattering cross sections appropriate to radiolysis (smooth curves) and knock-on displacement (discrete data points) for E_0 between 10 and 300 keV..... 38

Figure 2-11 **a.** Displacement threshold energies E_d obtained from DFT molecular dynamics calculations (crosses) and formation energies of chalcogen vacancies with nonrelaxed (dashed lines) and relaxed (solid lines) geometries in transition metal dichalcogenides MeX_2, X=S, Se, Te. **b.** Cross section for sputtering a sulfur atom from MoS_2, WS_2, and TiS_2 sheets as calculated through the McKinley-Feshbach formalism and the dynamical values of the displacement thresholds. Dotted lines are the data for the static lattice, and solids lines are the results of calculations where lattice vibrations are taken into account, assuming a Maxwell-Boltzmann velocity distribution. The cross denotes the experimentally determined cross section for MoS_2. The inset shows the same data for a larger range of electron energies..... 39

Figure 2-12 Schematic of one step PMMA-assisted transfer technique..... 41

Figure 2-13 Stages in making TEM samples using a FIB instrument. **a.** The area of interest has been marked. **b.** A Pt bar is deposited to protect this area from the Ga beam. **c.** and **d.** The two trenches are cut. **e.** The bottom and sides

FIGURE **Page**

of the slice are (final) cut. **f.** The TEM specimen is polished in place before extracting it. 41

Figure 2-14 Bragg reflection for electron beam incidenting crystal plane. 42

Figure 2-15 TEM image and diffraction pattern probe two aspects of the same phenomenon. 43

Figure 2-16 **a.** Diffracted beams generated by thin specimen scattering incident beam and **b.** example of diffraction pattern formed by recording diffracted beams on the plane perpendicular to incident beam. 43

Figure 2-17 Inferences between different electron beams give rise to lattice fringes. **a.** parallel line image generated by incident beam O and diffracted beam G in the **b.** ideal tilted two beam condition **c.** The fringes with three-fold symmetry produced by interference between direct beam O and three sets of diffracted ± G beams. 44

Figure 2-18 **a.** Various imaging modes in STEM by using different detectors that collect electrons scattered by different angles. **b.** 3D Schematic showing images available in the STEM as a probe is scanned across GaAs crystal by high angle annual dark field imaging mode. 45

Figure 2-19 Various signal generated by irradiating specimen with high energy electron beam. 46

Figure 2-20 Schematic of ionization process by electron irradiation. An inner (K) shell electron is ejected from the atom by a high-energy electron. When

FIGURE **Page**

the hole in the K shell is filled by an electron from the L shell, characteristic (Ka) X-ray emission occurs. The beam electron loses energy but continues on through the specimen..... 46

Figure 2-21 **a.** Schematic of operation principle of atomic force microscope in contact mode. **b.** Atomic force as a function of tip-sample distance. 48

Figure 3-1 Crystal structure of ReS_2 where purple and yellow dots are Re and S atoms respectively. 50

Figure 3-2 Schematic of CVD ReS_2 growth on sapphire. 52

Figure 3-3 Optical images of **a.** hexagonal and **b.** truncated triangular ReS_2 monolayers. **c.** AFM images of hexagonal and **d.** truncated triangular ReS_2 monolayer. 54

Figure 3-4 Optical images taken from ReS_2 monolayers deposited onto c-cut sapphire substrates at various conditions such as **a-c** low to high temperatures, **d-f** low to high precursor amount, and **g-i** low to high gas flow-rates. 57

Figure 3-5 **a.** Raman spectra of ReS_2 fabricated by different methods. **b.** Exfoliated ReS_2 thin layer and **c.** Its angle-resolved Raman plot of peak 214 cm^{-1}. 58

Figure 3-6 **a.** Optical image of the point I and II on hexagonal ReS_2 and **b.** corresponding polar Raman plots. 59

Figure 3-7 **a.** Raman mapping of 214 cm^{-1} peak on hexagonal ReS_2 with different laser polarization angles. **b.** Illustration of six subdomains in a hexagonal monolayer and their anisotropy directions. 60

FIGURE **Page**

Figure 3-8 **a.** HDAAF STEM images taken from pristine ReS_2 monolayers area showing the quasi-1D nature of synthesized monolayers and **b.** schematic depiction of ReS_2 monolayers and b- and a-axis lattice directions. 63

Figure 3-9 **a.** HRSTEM image taken at ReS_2 grain boundaries and specific zoom in images from **c., d.** grain boundary region and **b., e.** away from the grain boundaries. 64

Figure 4-1**a.** Structure model of WS_2 and **b.** ReS_2 where yellow, grey and purple dots are sulfur, tungsten and rhenium atoms, respectively. 67

Figure 4-2 Schematic of two-step CVD growth for ReS_2/WS_2 heterostructures..... 69

Figure 4-3 **a.** Optical image of continuous area of CVD WS_2 monolayer with manual scratch, inset is WS_2 PL mapping at scratched / unscratched region. **b.** Optical image of discrete WS_2 triangles domains. **c.** AFM measurement of triangular WS_2 and **d.** corresponding line scan profile showing monolayer thickness. 72

Figure 4-4 **a.** Optical image of the grown ReS_2/WS_2 heterostructure. **b.** AFM image of as-grown heterostructure edge. Inset is the line profile along white dash line. 73

Figure 4-5 **a.** Raman spectra and **b.** micro-absorption spectra of ReS_2, WS_2, and ReS_2 /WS_2 regions. **c.** Raman mappings of WS_2 358 cm^{-1} peak and **d.** ReS_2 163 cm^{-1} peak, respectively. Scale bar is 10 μm. 75

Figure 4-6 **a.** Low magnification STEM image of heterostructure edge, where ReS_2 and WS_2 overlap. **b.** Point EELS measurements performed at ReS_2, WS_2,

and ReS_2/WS_2 areas. **c.** STEM image at ReS_2/WS_2 interface and **d.** corresponding EELS line scan across it along the yellow arrow. A transition from WS_2 bandgap absorption at 2.03 eV to ReS_2 at 1.63 eV is shown. 76

Figure 4-7 **a.** HAADF STEM image taken at the ReS_2/WS_2 interface, and **d.** corresponding FFT image **b.** Zoom-in image of the area outlined by the solid white square in a and **c.** simulated STEM image by Dr. Probe software. **e.** FFT of ReS_2/WS_2 area squared by solid white line and **f.** FFT of pure WS_2 layer squared by dash blue line in a. 78

Figure 4-8 **a.** Optical image of ReS_2 layer grown along WS_2 edges extending towards sapphire substrates. **b.** Angle-resolved 214 cm^{-1} Raman peak of ReS_2 grown along the WS_2 edge I and II. **c.** Angle-resolved 214 cm^{-1} Raman of exfoliated ReS_2 and the ones grown on sapphire substrate and WS_2 sheets. **d.** Low-mag image of WS_2 monolayer triangle with lateral ReS_2 junction along edges. **e.** Zoom in HAADF STEM image of at the area squared by the black dash line in d. **f.** HAADF HRSTEM image of the white square area in e. **g.** HAADF HRSTEM image of larger scanning size at monolayer ReS_2 area. **h.** HAADF HRSTEM images of ReS_2 island on WS_2 surface and **i.** Maximum to a minimum intensity ratio of angle-resolved 214 cm^{-1} Raman peak of ReS_2/WS_2 vertical heterostructures with different ReS_2 sizes..... 80

FIGURE **Page**

Figure 5-1 **a.** Crystal structure of Tellurium viewing down from c-axis. **b.** SEM images of randomly oriented Te grown on sapphire. **c.** Low-magnification TEM image and corresponding diffraction pattern showing the c-axis is along the longitudinal crystal grown direction. 88

Figure 5-2 PVD results on different exfoliated 2D materials. **a.** GaS. **b.** GaSe. **c.** GaTe. **d.** mica. **e.** MoS_2. **f.** graphite. 89

Figure 5-3 **a.** Optical image of Te on GaSe for angle resolved Raman measurements. **b.** Schematic of angle resolved Raman measurement. **c.** Polar plot of 92 cm-1 peak collected from Te ribbons. 91

Figure 5-4 Cross-section TEM images collected from tellurium/GaSe 2D interfaces. **a.** Low magnification cross-sectional TEM image of Te/GaSe heterostack. **b.** SAED pattern of GaSe showing its zone axis is [100], which is fixed as a reference during the experiment. **c.** SAED pattern of Te crystal showing [100] zone axis. **d.** Structural models illustrating cross-sectional and top view of the heterostructure. 91

Figure 5-5 **a.** SAED pattern of GaSe showing its zone axis is [100], which is fixed as a reference during the experiment. **b.** SAED pattern of Te crystal showing [111] zone axis. **c.** Structural models illustrating cross-sectional and **d.** top view of the heterostructure showing the alignment of [001] Te chain and armchair direction in GaSe. 93

Figure 5-6 Schematic showing **a.** Te along armchair direction and **b.** zigzag direction of GaSe and MoS_2 substrates. 94

Chapter 1 Introductions

I'm certain our children or grandchildren will not be using silicon. The world is large; there must be a better material.

— Chenming Hu, inventor of the FinFET

1.1 The Rise of 2D Materials

Developing smaller, faster, and cheaper electronic devices have been the core of modern electronic industry in the past decades. Moore's law has been well-followed by scaling integrated circuits down, but the current will be increasing difficult to control as the device size shrinks. One way to address this problem is by designing better transistor gate structures, such as a multiple-gate field-effect transistor. For example, FinFETs which have gate dielectric on three sides of the channel are made in 16nm scale commercial products are available since 2016. However, as the node size further reaches the extreme limit of below 10 nm, undesired phenomena such as quantum tunneling and short channel effects come into play in silicon based electronics.

A more revolutionizing way is through the design of novel materials. Several two-dimensional (2D) materials have been proposed as channel materials for next generation devices because of their thinness and extraordinary attributes. For example, graphene shows great potential by its tremendously high carrier mobility and subsequent 1 nm gate length MoS_2 transistor with high on/off switch ratio demonstrates the capability of these atomically thin layers in the electronic industry.

As the inventor of the FinFET says, "there must be a better material", large groups of 2D materials have been discovered since graphene and have indeed intrigued many

researchers worldwide. It is reasonable to believe that the versatile collections of the 2D family will continue to grow and become the essential part of future electronic and optoelectronic applications.

1.1.1 Graphene

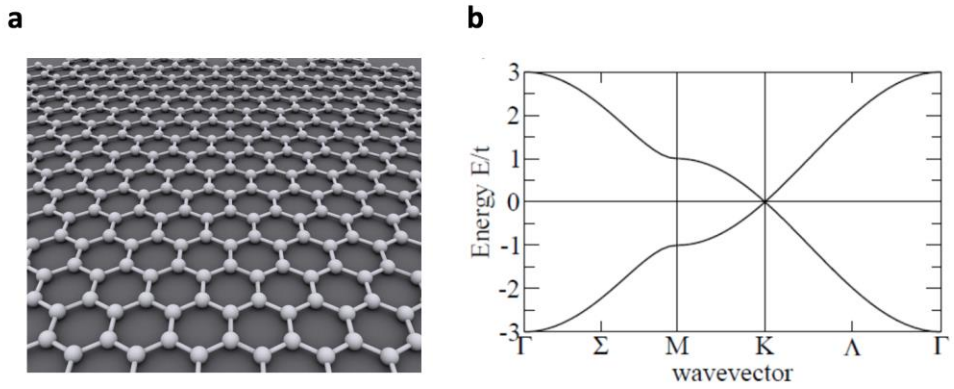


Figure 1-1 **a.** Atomic structure of graphene and **b.** its electronic band structure showing a linear dispersion at K point.

Two-dimensional crystals were predicted to be thermodynamically unstable until the successful isolation of a single atomic layer from bulk graphite in 2004, which marks the beginning of new era of researches in 2D materials[1]. The name graphene is given to such 2D sheet of carbon atoms with sp^2 hybridization arranged in a honeycomb network (Figure 1-1a). The subsequent discoveries of its extraordinary properties have drawn tremendous attentions of researchers worldwide. The most noticeable feature of graphene lies in its unique linear dispersion of electron energy in K-space (Figure 1-1b), which essentially makes charge carriers behave as massless Dirac fermions[2,3]. The observation of room temperature quantum Hall of graphene is expanding the boundary of condensed matter physics. Later discoveries of incredibly high carrier mobility (200 000 $cm^2v^{-1}s^{-1}$)[4],

high thermal conductivity (5000 $Wm^{-1}K^{-1}$)[5] and large young's modulus (1.0 TPa) [6] enable graphene to be a promising candidate for next-generation electronics.

1.1.2 TMDCs

Graphene stands out in the 2D family as a gapless metallic material. However, to practically revolutionize the electronic industry, semiconductors are needed for transistor fabrications as they are building blocks of modern integrated circuits. Although band gap can be opened in graphene by artificial nanostructuring, chemical functionalization etc., those processes add extra complexities towards practical applications[7]. Transition metal dichalcogenides (TMDCs) as layered materials have been in use and research for decades, but only until the recent advent of graphene and advanced sample preparation techniques and nanoscale characterization methods, researchers are triggered to push the dimensional limit of TMDCs.

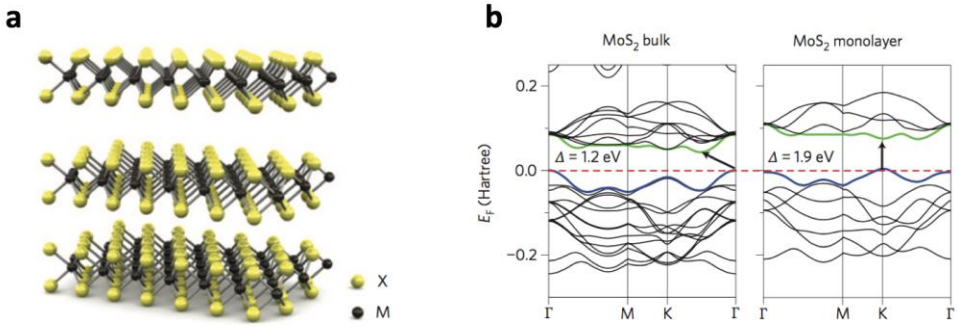


Figure 1-2 **a.** The structure of MX_2 and **b.** band structure of MoS_2 showing indirect to direct transition at monolayer limit.

As the name suggests, TMDCs with formula MX_2 comprise of one transition metal M (Ti, Hf, Zr, V, Nb, Ta, Mo, W, Tc, Re) and two Chalcogen atoms X (S, Se, Te) as shown in Figure 1-2a. TMDCs benefit from the rich pool of elements in that they can largely adjust their electrical properties from metal to (NbS_2) semiconductor (MoS_2) by forming

different compounds[8]. One distinct feature of TMDCs semiconductors is the indirect to direct band structure transition from bulk materials to their monolayer limit (Figure 1-2b). They show a wide range of bandgap modulation capability because of rich choices of chemical components, which enables the electronic application of various kinds. In terms of optical applications, excitons are two-dimensional confined in TMDCs semiconductors which result in their large excitonic binding energies (hundreds of meV) compared to conventional materials (tenths of meV)[9,10]. These excitons are thus stable at room temperature for optoelectronics such as LED, photovoltaics, and photodetectors.

1.2 Defects in 2D Layers

Defects are important for the fundamental understanding of material properties. It is the engineering of defects (doping) in silicon that makes the modern Si-based electronics possible. To fully exploit the potential of 2D materials in the electronic and optoelectronic application, careful characterization of defects and their impacts on the properties of these thin layers is necessary.

Here intrinsic defects of graphene and TMCs family are briefly discussed. They are generally categorized into point defects, dislocation and grain boundaries. Because of the reduced dimensionality, grain boundaries are now 1D imperfections and 3D defects do not even exist in 2D materials.

1.2.1 Point Defects

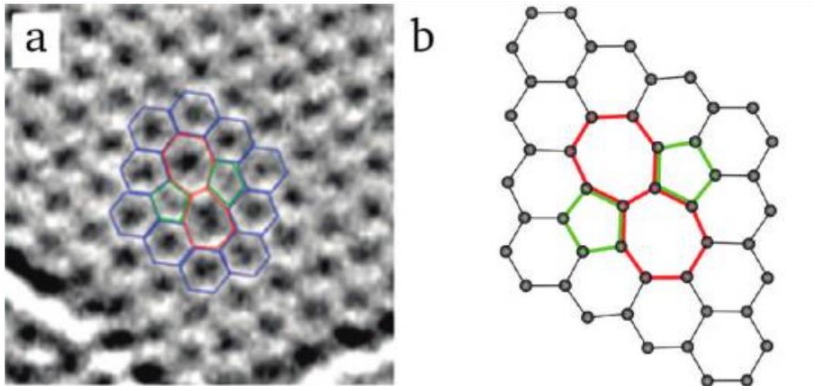


Figure 1-3 Stone Wales defect SW(55-77), formed by rotating a carbon carbon bond by 90°. **a.** Experimental TEM image of the defect and **b.** its atomic structure as obtained from DFT calculations.

Graphene has strong ability to reconstruct its atomic arrangement by forming non-hexagonal rings at defect sites. The simplest example is the Stone Wales (SW) defect, which does not involve any removed or added atoms. Four hexagons are transformed into two pentagons and two heptagons 55|77 as shown in Figure 1-3[11]. Single vacancies tend to form a five-membered and a nine-membered ring 5|9 illustrated in Figure 1-4[11].

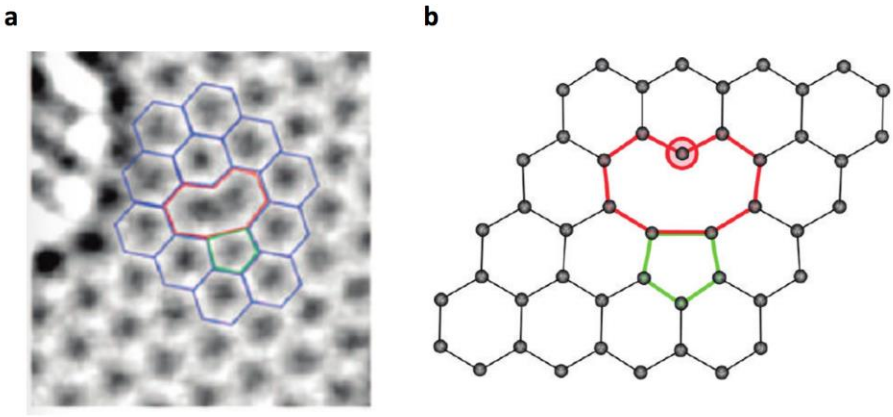


Figure 1-4 **a.** Single vacancy 5|9 rings seen in an experimental TEM image. **b.** its atomic structure obtained from DFT calculations.

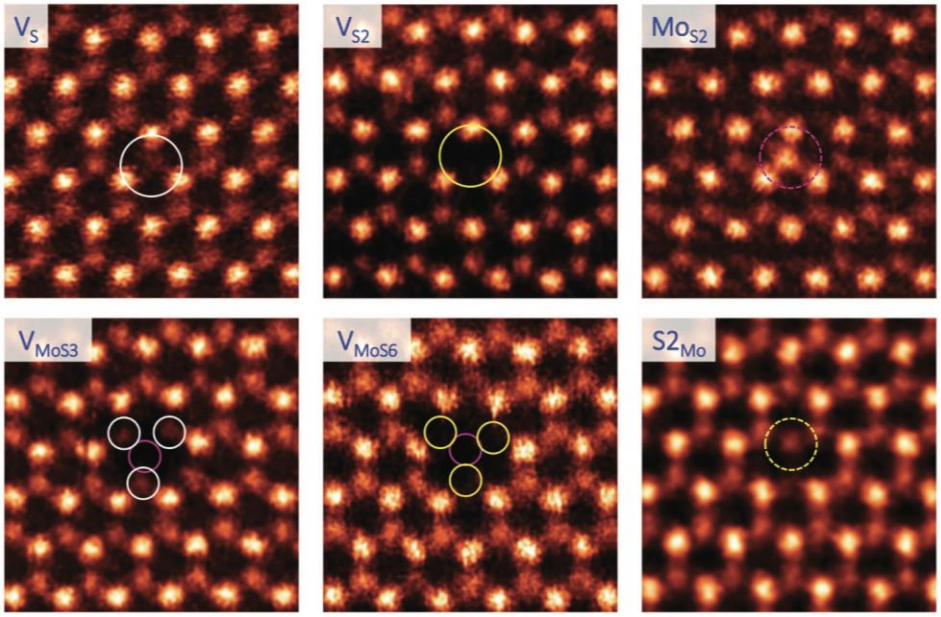


Figure 1-5 Experimental ADF STEM image of vacancies and antisite defects in MoS_2.

2H MoS_2 as a representative of TMDCs class materials have been extensively studied. Because of its more complicated three atomic layer unit cell, defects in MoS_2 have more variations than those in graphene as shown in Figure 1-5[12]. One unique feature of TMDs, when compared to graphene, is the existence of antisite defect structures where metal atoms can occupy the sites of chalcogen atom pairs or a pair of chalcogen atoms can occupy metal atom sites. Anti-site defects in MoS_2 reveal that when molybdenum atoms replace a sulfur pair within the lattice, a break in the symmetry of the hexagonal network is observed, whereas a sulfur pair will replace molybdenum atoms while maintaining the crystal lattice symmetry.

1.2.2 Line Dislocations and Grain Boundaries

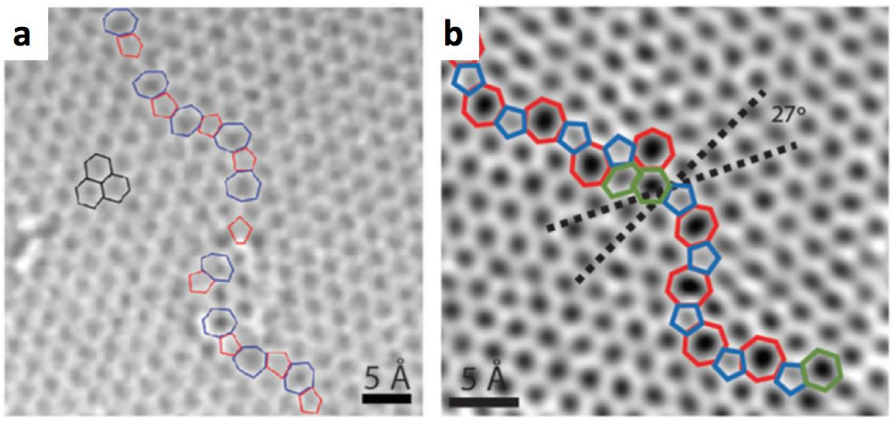


Figure 1-6 HR TEM images of grain boundaries in graphene.

Grain boundaries and dislocations in graphene usually exist in the form of 5|7 rings (Figure 1-6)[12]. They appear to have significant line curvature and the curvature persists even after extensive imaging, which can cause atom movements at the boundaries. This departure from theoretically studied boundaries is likely caused by the roughness of growing edges prior to crystal stitching during the synthesis[12].

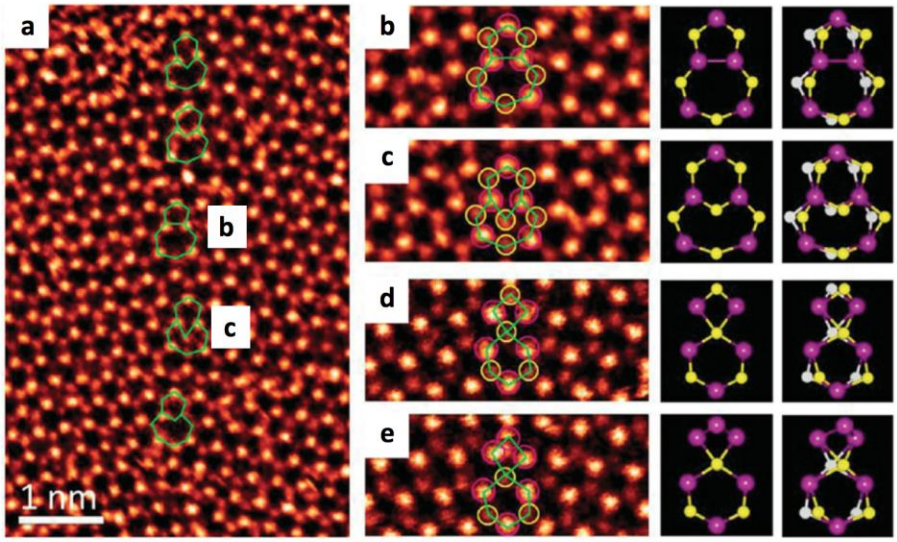


Figure 1-7 **a.** Tilt boundary in MoS_2 with an 18.5° angle. **b.** 5|7 and **c.** 6|8 dislocations taken from a. **d.** Pristine and **e.** molybdenum substituted 4|6 dislocations observed in tilt boundaries, respectively.

The complex bonding capability of the atomic constituents of TMDCs allows for interesting boundary structures. In tilt boundaries, new 4|6 and 6|8 dislocations have been observed along with conventional 5|7 dislocations and are believed to be the result of variations in the local concentrations of reactant species during growth. A collection of dislocation structures observed in MoS_2 tilt boundaries is shown in Figure 1-7a to e[12]. In mirror boundaries, 4|4 and 4|8 line defects exist between neighboring crystalline domains.

1.3 Heterostructures of 2D Monolayers

The very nature of van der Waal interaction between layers and no dangling bonds on surface allow dissimilar 2D layers to be stacked with great freedom without worrying about lattice match, which is a serious concern in conventional semiconductors.

Therefore, the true potential of these unique classes of materials can be realized especially when a variety of different types of 2D materials are stacked in lateral or vertical structures to form complex heterostructures and superlattices[13,14]. Heterostructures built by 2D materials have been manifested in flexible photovoltaic devices[15,16] and field-effect tunneling transistors[17]. MoS_2/graphene heterostructures also have shown great potential in many novel applications, such as electronic logic and memory devices[18], ultrasensitive detection of DNA hybridization[19], hydrogen evolution reaction[20,21], and energy storage[22,23].

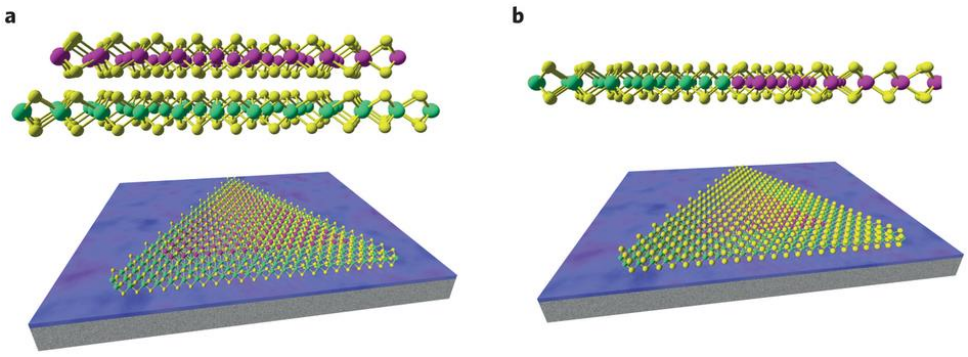


Figure 1-8 Schematic representation of heterojunctions between monolayers of two different transition metal dichalcogenides, for example, between MoS_2 and WS_2. Mo, W and S atoms are represented by green, pink and yellow spheres, respectively. **a.** WS_2 can grow on top of MoS_2. or **b.** laterally from MoS_2.

Figure 1-8 shows the two possible geometries of forming heterostructures using atomically thin 2D layers. One is to build a vertical heterojunction, where one monolater stacks on the other for example, WS_2 on MoS_2 (Figure 1-8a). The other is to build in-plane lateral heterostructure as shown in Figure 1-8b. Although stamping transfer methods can be conveniently used to build vertical heterostructures[24-27], lateral heterojunctions are typically fabricated by chemical vapor disposition (CVD) technique[28-31].

1.4 Pseudo–1D Materials

High symmetry of hexagonal crystal lattice in conventional 2D materials discussed above makes them isotropic in terms of their properties. For example, their optical, electrical and phonon characteristics are similar along different directions across their 2D basal plane, which is beneficial for conventional electronic applications. To have uniform device performance, it is advantageous that transistors built on a large scale wafer have similar properties along various crystal directions[32].

On the other hand, recent research efforts have also been made towards the development of the anisotropic 2D materials, such as black phosphorus, ReS_2, etc. These materials with reduced crystal symmetry exhibit asymmetrical in-plane behaviors, where electrical, thermal, optical and mechanical properties are distinct along different crystal directions. Certain crystal axis serves as high carrier transport channel as a result of reduced backscattering from hot electrons[33] and enable fabrication of high mobility (10000 $cm^2V^{-1}s^{-1}$ predicted in TiS_3 and 700 $cm^2V^{-1}s^{-1}$ demonstrated in Tellurium) transistors for next generation electronics[34,35]. In addition, this new degree of freedom stimulates previously less explored tunability in materials properties and provide advances in polarized light detection and valleytronics[36,37].

1.4.1 Black Phosphorus and Tellurium

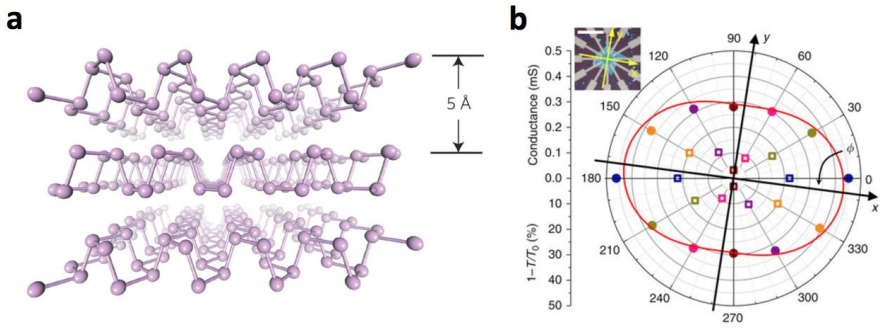


Figure 1-9 **a.** The structure of black phosphorus and **b.** anisotropic DC conductivity.

Black phosphorus is a well-known example of anisotropic 2D materials. Its strong in-plane anisotropy stems from its special crystalline structure: inside a single layer, each P atom is covalently bonded to three adjacent P atoms to form a buckled honeycomb structure as shown in Figure 1-9a[38]. Black phosphorus has a tunable band gap between 0.3 eV to 2 eV depending on its thickness which covers a significantly wide range of spectrum[39].

The structural anisotropic leads to electrical and thermal conductivity at selective crystal directions[39,40]. BPs films with a thickness of 15 nm show high mobility above 650 $cm^2 V^{-1} s^{-1}$at room temperature and above 1,000 $cm^2 V^{-1} s^{-1}$ at 120 K along the buckled P direction. This indicates that carriers travel significantly faster in the light effective mass (*x*) direction (Figure 1-9b), implying its promising future for high frequency, thin-film electronics[39]. However, its strict synthesis conditions (10 kbar, 1000 ^oC) and unstable nature largely limit its potential applications.

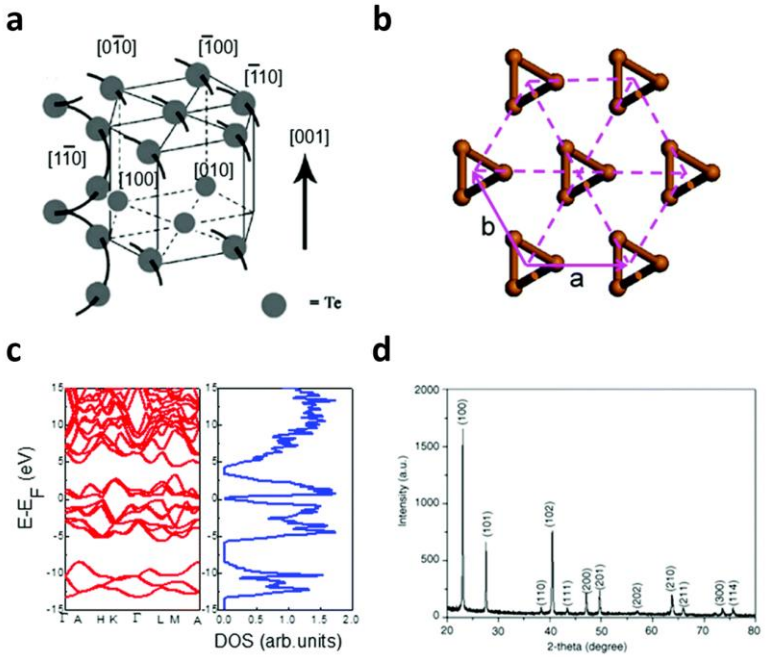


Figure 1-10 Schematic showing the crystal structure and electronic structures of tellurium. **a.** Spiral chains of the crystals arrange in a crystal structure. **b.** View along the c-axis indicating spiral chains of Te atomic structures with an angle of 120°. **c.** electronic band structures and total density of states (DOS) of tellurium. **d.** The XRD pattern spectrum of Te nanostructures.

Tellurium, another elemental 2D materials, is considered as successor to BPs because it offers comparable high carrier mobility[35] and anisotropic properties[41] and yet with

much improved environmental stability[42,43]. It has trigonal crystal structure and possess spiral Te chains structure (Figure 1-10) that leads to anisotropic properties.

1.4.2 Transition Metal Trichalcogenides MX_3

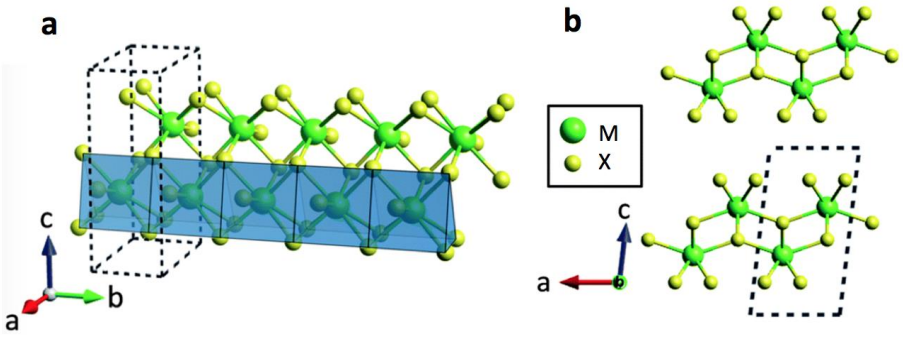


Figure 1-11 **a.** Tilted side view of a ball and stick model of a single layer of MX_3. M and X atoms are denoted by green and yellow spheres, respectively. The dotted black line represents the primitive monoclinic cell. And the blue trigonal prisms represent the chain. **b.** stacked layers of bulk MX_3 as seen from the *b* axis.

Transition metal trichalcogenides (TMTCs) are reported to have structural anisotropy and thus anisotropic properties. MX_3 consists of IVB or VB group metal element M and X represents S, Se or Te. They typically have monoclinic structures with an explicit chain like features in the b-axis directions[44].

As a new member of the family of 2D layered materials, TMTCs offer similar diversity as that of TMDCs and yet display many outstanding properties as or better than other prominent 2D materials. For example, like phosphorene, TiS_3 monolayer exhibits both a desired direct band gap and relatively high carrier mobility for high performance electronic devices, and yet TiS_3 is much more chemically stable and free from the easy decomposition problem in phosphorene[45].

1.4.3 Anisotropic TMDC ReX_2

Interestingly, some TMDCs, for example, ReS_2 and $ReSe_2$, crystallize in distorted 1T' structure forming linear in-plane metal chains, which also leads to varied properties responses in selective directions. The direct optical band gap for $ReSe_2$ has been measured to be 1.26 eV in the bulk and 1.32 eV in monolayer[46]. For ReS_2, it has been reported that optical bandgap is 1.5-1.6 eV in the bulk and slightly higher for the monolayer[47,48].

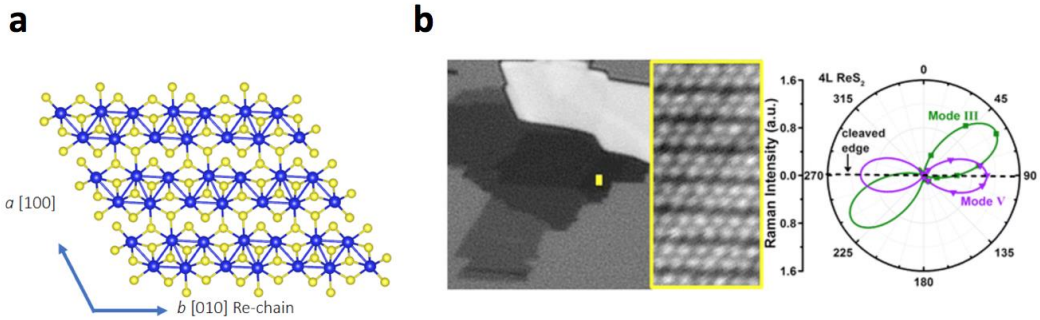


Figure 1-12 **a.** The structure of ReX_2 and **b.** Anisotropic (Re-chain) direction probed by angle-resolved Raman spectroscopy and STEM.

Compared group VI metals forming to isotropic TMDCs such as Mo and W, each Re atom has one extra electron. These electrons in rhenium bond neighboring metal atoms to form diamond-shaped repeating unit extending along b-axis. Thus, metal chains can clearly be seen when looking down from [001] crystal directions (Figure 1-12a). Recent reports point out that angle-resolved Raman spectroscopy, where the polarization of incident laser is varied, provides a convenient way for determining the Re-chain directions (Figure 1-12b)[49-51]. Because of the differences in polarizability and optical absorption coefficient in a- and b-axis, the Raman intensity reaches a maximum when laser polarization coincides the Re-chain direction.

Since ReS_2 is the main materials system studied in this dissertation, it will be discussed in more details below.

1.4.3.1 Structure of TMDC Monolayer

TMDCs possess rich variations of structural and chemical compositions, because of abundant electronic configurations in the transition metal and chalcogen atoms (Figure 1-13)[52].

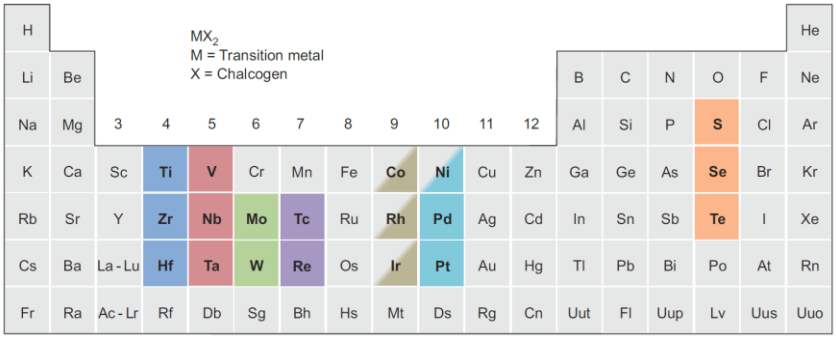


Figure 1-13 Periodic table for two-dimensional layered van der Waals transition metal dichalcogenides.

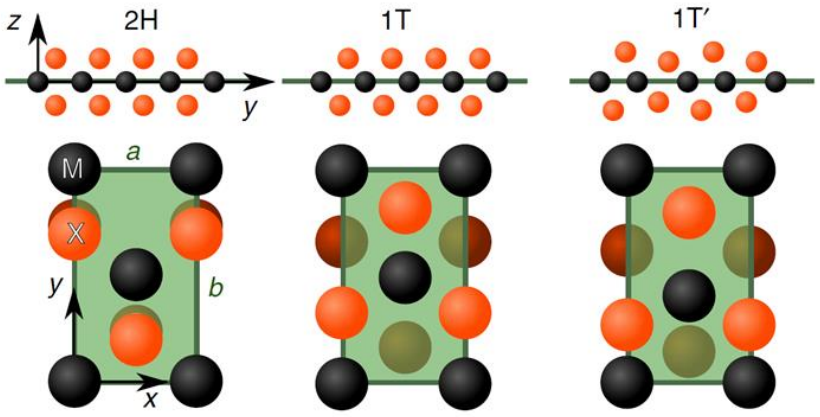


Figure 1-14 Three typical phases: 2H, 1T and 1T' (distorted 1T) of TMDCs.

Monolayer MX_2 exist in multiple phases as shown in Figure 1-14 where 2H and 1T are the most common, while only a few are stabilized in 1T' (distorted 1T) structure[53].

2H is also called trigonal prismatic structure where the chalcogen atoms of the top layer and bottom are exactly aligned. It belongs to D_{3h} space group and typically shows semiconducting behaviors.

If transition metal is coordinated by chalcogen atoms in a way that they form octahedrons, then the structure becomes 1T, or octahedral phase belonging to D_{3d} symmetry group. Most of 1T phases have metallic characteristics as electrons in d-orbitals lower their energies by narrowing band gap as compared to semiconducting 2H phase. This point will be discussed in detail in the following section.

A few MX_2 are stabilized in distorted 1T structures, titled 1T' phase, such WTe_2 and ReS_2. Transition meatal atoms in 1T' structure form metal-metal bonds and therefore distort the lattice, which reduces symmetry from trigonal to triclinic. Such distortion can be considered as deviation of metal atoms from perfect 1T lattice sites (dimerization of metal atoms along armchair direction) and the driving force is argued in terms of Peierls or Jahn–Teller distortions similar to charge density waves.

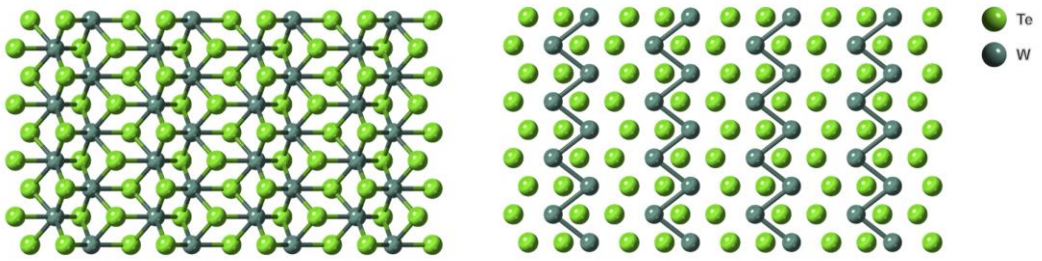


Figure 1-15 Distorted 1T phase in WTe_2, where grey and yellow atoms are tungsten and tellurium atoms, respectively. **a.** Top view showing the basal plane with W-Te bonding. and **b.** showing only zigzag bonding between neighboring tungsten atoms.

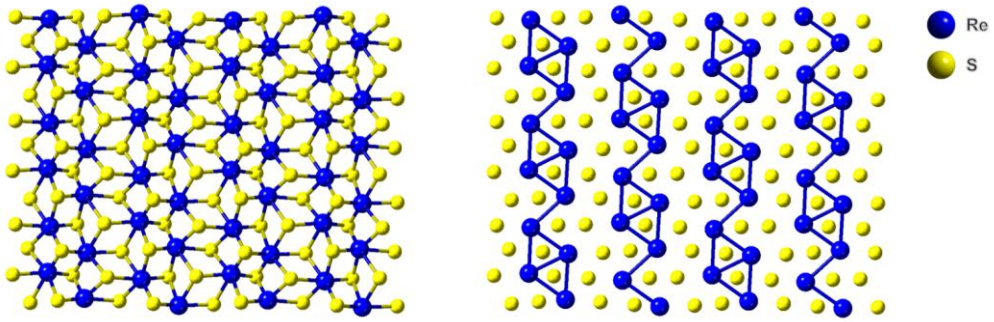


Figure 1-16 Basal plane of ReS_2 monolayer showing **a.** Re-S bonding and **b.** only Re-Re bonding. Diamond-shape repeating units is formed by four Re atoms as linear chains.

The distorted structures can be further categorized into different kinds, depending on the types of metal-metal bonding. For example, in the WTe_2, neighboring tungsten atoms form zigzag shape chain structure (Figure 1-15). ReS_2 on the other hand, repeating units of diamond shape are formed by four rhenium atoms, extending along its [010] crystal axis (Figure 1-16).

It is the distortion of atoms that leads to anisotropic behaviors in these TMDCs 2D materials.

1.4.3.2 Phase Transition

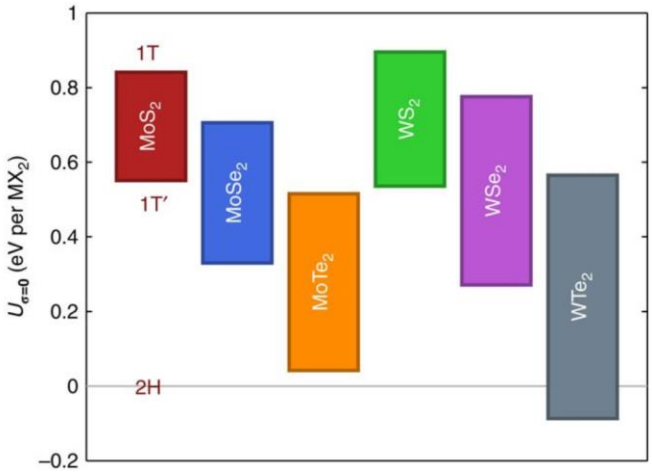


Figure 1-17 Calculated energy for common TMDC monolayers in 2H, 1T and 1T' structures.

Although each TMDCs has preferential stable phase, they are able to switch structures, as a result of the small energy difference between phases (Figure 1-17)[53]. MoS_2 for example, normally exist in 2H phase, can be found in 1T phase when exfoliated by Li intercalation methods[54-56]. Charge transferred from lithium to MoS_2 is considered as the stimuli for 2H-1T structure transition in early studies for bulk TMDCs[57]. In fact, the electron counts in d orbitals of transition metal are critical for determining the stable phase of TMDCs[52]. The energy gap in 2H phase increases the total energy of the system when extra electrons are added, whereas the metallic 1T phase provides lower energy states habiting transferred electrons (Figure 1-18)[58]. The energy gain is large enough to offset the work required for lattice distortion. Therefore, by forming 1T phase, the system reaches a lower energy state compared to 2H phase, and hence more stable.

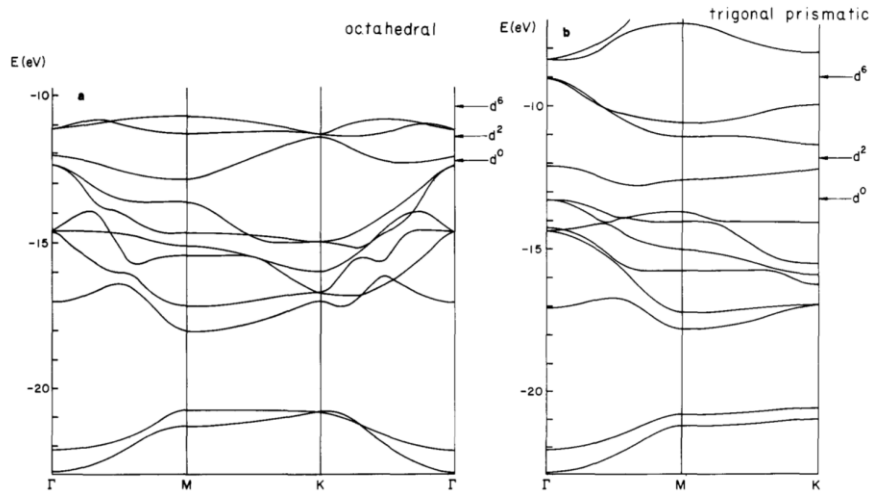


Figure 1-18 Calculated band structure of $ReSe_2$. **a.** octahedral structure (2H) and **b.** trigonal prismatic structure (1T).

The general mechanism of 2H-1T phase transition in TMDC monolayer can be understood by the d-orbital splitting as shown in Figure 1-19[59]. Crystal field theory states that the five initially degenerate 4d Mo orbitals are split into multiple degenerate energy

levels, because of effect of octahedrally arranged negative ions positioned on the six vertices. For 2H MoS_2, there are three levels: 1) one filled dz^2 orbital, 2) two empty dx^2-y^2, dxy orbitals, and 3) two empty dxz, dyz orbitals, as shown in Figure 1-19d. In contrast, the Mo 4d orbitals in the 1T-MoS_2 are separated into two levels: 1) three degenerated dxz, dyz, and dxy orbitals occupied by two electrons, and 2) empty dz^2 and dx^2-y^2 orbitals as shown in Figure1-19f. Unfilled degenerate orbitals lead to metallic ground states of the 1T MoS_2 and less structure stability as compared to 2H MoS_2 with saturated dz^2 orbitals[59]. However, when 1T MoS_2 is doped with extra electrons that occupy all three of the dxz, dyz and dxy orbitals, the stability of 1T MoS_2 is largely increased. Opposite is true for electron doped 2H MoS_2, where the extra electrons half-fill dx^2-y^2 or dxy states and thus reduce the stability of 2H structure.

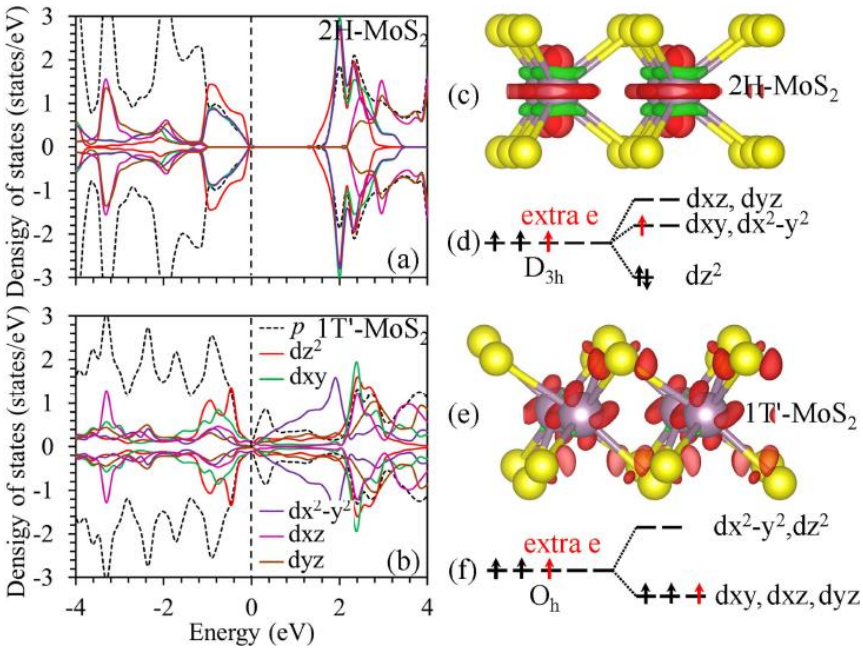


Figure 1-19 Orbital states. Partial density of states of **a.** 2H- and **b.** 1T'- monolayer MoS_2. Isosurface (0.003 e/Å^3) of the charge distributions of **c.** 2H- and **e.** 1T'- MoS_2 doped with 1.00 e/f.u. Within crystal field theory, the Mo 4d orbitals **d.** D_{3h}- and **f.** O_h-MoS_6 unit will split into three and two groups, respectively.

Figure 2-19a and b are the calculated partial density of states of 2H and 1T' monolayer MoS_2, respectively. 2H monolayer MoS_2 shows semiconducting characters where the Mo 4dxz and 4dyz orbitals do not contribute to energy states near VBM and CBM. The 1T' monolayer MoS_2 is more stable when doped with extra electron since no charge from M-S bond is lost[59].

In short, the electron doping destabilizes the 2H MoS_2 structure while forcing a structural transformation into the 1T' phase by renormalization of the Mo 4d orbitals. Later studies on monolayer TMDCs show that the exact stable phase depends on the specific electron doping density[60]. This also explains the reason that ReS_2 is intrinsically stable in 1T' phase, as each rhenium atom has one extra electron than molybdenum and thus serves as high concentration electron donor in the "2H MoS_2-like" system.

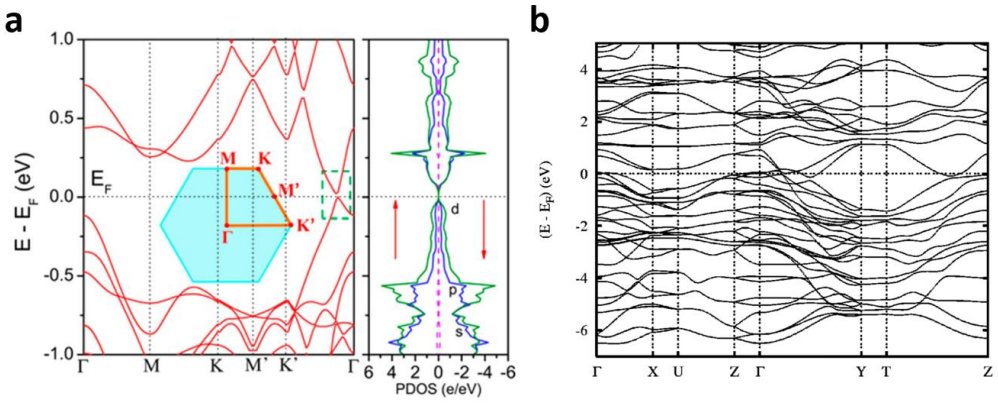


Figure 1-20 **a.** Calculated electronic band structures and density of states for 1T' MoS_2. **b.** band structure of WTe_2.

It needs to point out that the octahedrally coordinated 1T TMDCs in ideal condition should be metallic. However, the lattice distortion makes 1T' phase either semiconducting or metallic, depending on specific systems. For example, 1T' WTe_2 is

semimetal[61,62], but 1T' MoS_2 and ReS_2 are semiconductors[47,60] as shown in Figure 1-20a and Figure 1-21a.

1.4.3.3 Electronic Band Structure

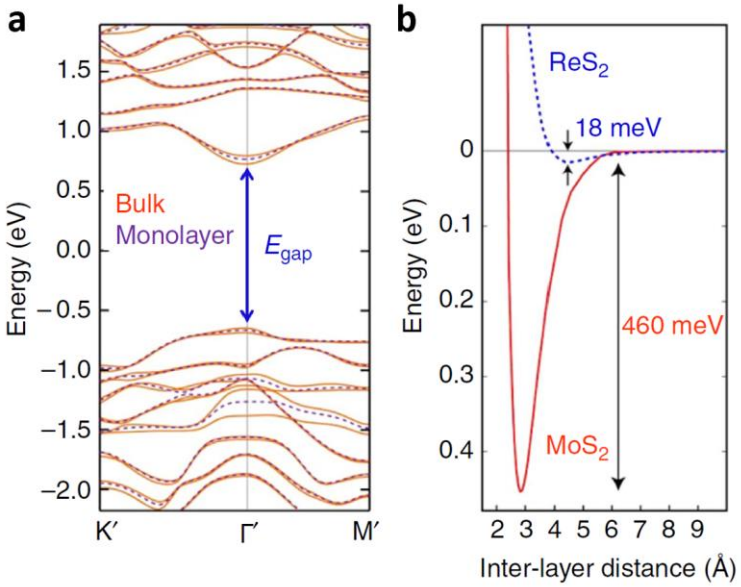


Figure 1-21 **a.** band structure of bulk (red solid line) and monolayer (magenta dash line). **b.** Energy of the system as a function of interlayer distance.

Unlike typical MX_2 that undergo indirect-direct bandgap transition from bulk to monolayer, ReS_2 is intrinsically direct in terms of band structure even in bulk form (Figure 1-21a)[47]. The direct transition happens at Gamma to Gamma as opposed to K-K in traditional TMDCs. The almost identical band structure in bulk and monolayer ReS_2 is due to the extremely weak interlayer coupling, which is a result of the lack of strict stacking order in ReS_2. Figure 1-21b compares the system energy between MoS_2 and ReS_2 as a function of interlay distance. While MoS_2 varies its energy as much as 460 meV between 2-6 angstrom, ReS_2 shows little dependence of system energy on the interlay spacing.

1.4.3.4 Raman Scattering

Four rhenium and eight sulfur atoms in ReS_2 unit cell form a total of 36 phonon modes with irreducible representation Γ=18 (Ag+Au), of which 18 modes are Raman active (Figure 1-22)[63]. It is easily noticeable that those peaks are located at the same vibrational frequency regardless of crystal thickness, which confirms the decupling nature of the ReS_2 interlayers.

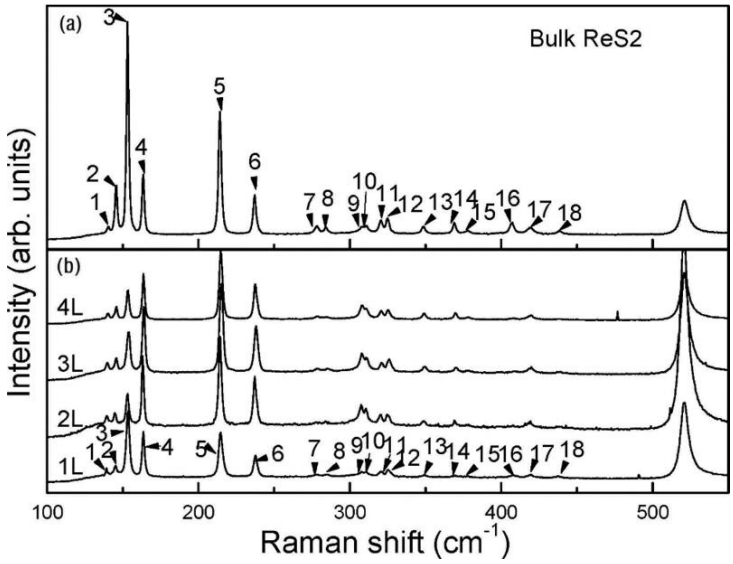


Figure 1-22 Raman spectra of thin layer and bulk ReS_2, with 18 Raman active peaks labeled.

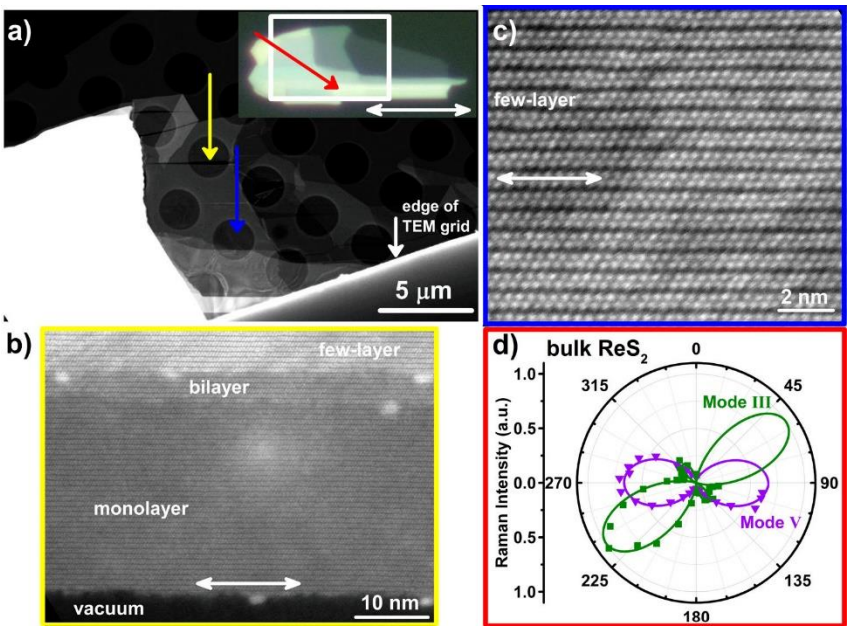


Figure 1-23 Annular dark-field scanning transmission electron microscopy (ADF-STEM) of bulk to monolayer ReS_2. **a.** Low magnification STEM image of ReS_2 sample on a TEM grid. Inset: optical micrograph of sample on PDMS before transfer. **b.** Medium magnification ADF-STEM image of suspended ReS_2 where the sample tore during the transfer process. **c.** High-magnification ADF-STEM image of a few-layer region. **d.** Polarization- and orientation-resolved Raman spectra of bulk region. White double arrows depict direction of rhenium chains in a-c.

Some Raman modes related to in-plane Re-Re vibrations are found to be sensitive the polarization of incident laser. Of particular interests is the ~ 213 cm^{-1} that involves the Re-Re bond vibration, which has been demonstrated to be effective in determining the crystal orientation by angle-resolved Raman spectroscopy in backscattering configuration. When the polarization direction of incoming laser is aligned with the b-axis of ReS_2, the 213 cm^{-1} reaches its highest intensity and thus the orientation can be deduced from the polar Raman plot (Figure 1-23d)[49]. Using angle resolved Raman spectroscopy, Re-chain (b-crystal axis) in ReS_2 can be conveniently determined.

1.4.3.5 Excitons and Photoluminescence

ReS_2 exhibit polarized absorption feature with two prominent exciton transitions at 1.4-1.7 eV.

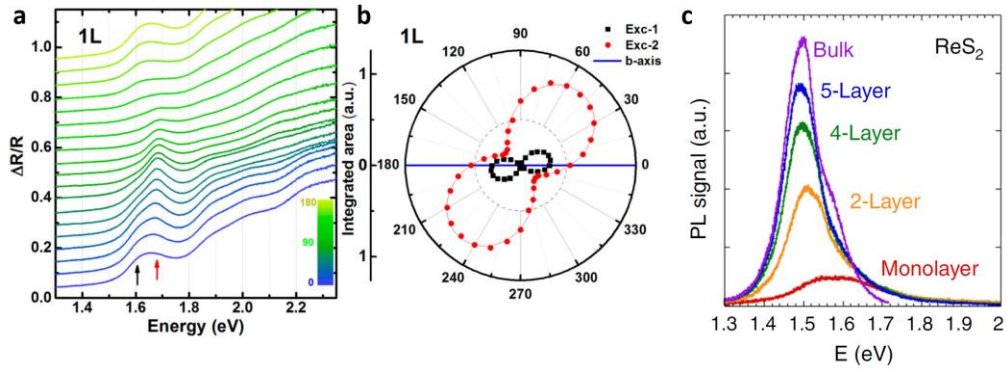


Figure 1-24 **a.** Differential reflectance spectra of monolayer ReS_2 with varied incident laser polarization angles. **b.** Excitonic transition energies are exacted out and plotted as function laser polarizations. **c.** photoluminescence spectra of ReS_2 with varied thickness.

The excitons are polarized in ReS_2 monolayer. Exciton 1 located at 1.6 eV has its highest absorption efficiency when light is polarized parallel to its Re-chain direction. Exciton 2, on the other hand, does not follow the same rule but maximize its absorption intensity when laser polarization is at 45^o with b-axis as shown in Figure 1-24b[48]. Photoluminescence of ReS_2 shows a decreasing intensity from bulk to monolayer, opposite to the trends in conventional TMDCs semiconductors (Figure 1-24c)[47].

1.5 Discussions and Scope of this Dissertation

The first demonstration of FET based on graphene in 2004 unveils the possibility of building smaller and faster devices using an atomically thin layer of carbon. However, the lack of intrinsic band gap limits its potential in the semiconducting industry. Later discovery of semiconducting single layer MoS_2[64] further brings us a clearer vision of operating 2D materials-based electronic devices with high performance, e.g. on/off

switch ratio. Over the years an increasing number of 2D materials systems with unique structures and properties have been reported, including pseudo 1-D materials with strong in-plane anisotropy. These materials, which are structurally different from traditional isotropic 2D materials, have preferential carrier transport and high optical absorption channels along certain crystal axis. Therefore, two-dimensional anisotropic thin films show special potential in developing high speed electronics and optoelectronics, such as ultrathin polarizers and polarization detectors.

1.5.1 Challenges for Anisotropic Materials

While isotropic 2D materials such as graphene and MoS_2 are well-documented, novel 2D layers with anisotropic properties are still at the seminal stage. This dissertation aims to address two of the many challenges in terms of full utilization of 2D anisotropic materials.

1.5.1.1 High quality monolayer synthesis

The first challenge is batch synthesis of highly crystalline ReS_2 monolayers. Previously, it has been reported to grow on SiO_2 substrate in a dendritic form which leads to poor crystal quality, and the control over its anisotropy (its key feature) is lost[65]. Our group pioneered in ReS_2 CVD monolayer growth with noteworthy anisotropy and found out that it can be achieved on the c-cut sapphire substrate, likely due to the crystallinity of sapphire as compared to amorphous SiO_2[66]. It is noted that ReS_2 monolayers are more likely to form close to the step edges of the sapphire compared to the center area of the substrate, which is in line with previous theoretical and experimental studies showing a substantial reduction in the energy barrier of nucleation close to the step edges[67,68]. Therefore, similar catalytic growth processes can be expected in nucleation and diffusion

of ReS_2 monolayer growth on sapphire wafers, which lead to preferentially oriented monolayer hexagons. However, anisotropic responses from grown ReS_2 samples vary significantly at different portions with in each monolayer (some regions even behave as isotropic material). Further studies show that these ReS_2 flakes are in fact comprised of subdomains, which can result in the undesirable loss of anisotropy at grain boundaries and leads to the second challenge discussed in the next section.

In **Chapter 4**, we discuss in detail synthesis and domain architectures of those CVD grown ReS_2 monolayers and the origin of inconsistent anisotropy from a microscopic point of view.

1.5.1.2 Controllability over anisotropic directions

Successful synthesis of high quality 2D anisotropic materials is only the first step. The following challenging task towards their practical applications is the controllability over their anisotropic directions. To fully realize the potential of anisotropic materials, one needs to take advantages of these preferential in-plane crystal channels for high mobility, thermal conductivity and optical absorption, etc. Therefore, practical applications require macroscopic scale consistence of anisotropic structural alignment. The overall anisotropic response can be compromised if orientations of anisotropic materials are only locally aligned. Randomization of anisotropic directions result in rather undesirable loss of anisotropy at macroscale as discussed in Chapter 4.

One possible route to achieve controlled oriented growth is epitaxy, which is widely applied in semiconductor industry[69]. Van der Waals epitaxy, first coined by Koma[70,71], has been observed in multiple 2D monolayer vertical heterostructures: a second monolayer grown on top of the other monolayer or substrate show orientation registration

through weak van der Waals interaction between layers[28,29,72]. Therefore, proper design of underlying layer might lead to desirable orientation control of top anisotropic monolayers.

In lateral heterostructures, on the other hand, epitaxial interfaces are covalently bonded and largely depend on the crystal terminating planes, where a strict registration between constituent materials at junction interface is required. In-plane heterostructure of conventional 2D isotropic materials have been demonstrated to have atomically sharp interface[28,73], even with high lattice strain[74]. Therefore, it is reasonable to expect anisotropic materials with defined anisotropic directions to grow epitaxially, if the seeding monolayer crystal and the lattice parameters at the heterostructure interface are properly designed.

Chapter 5 and **Chapter 6** explore the possibility of controlling anisotropy of anisotropic ReS_2 and tellurium layers by the design of heteroepitaxial growth.

Chapter 2 Review of Experimental Techniques

2.1 Materials Fabrication

Methods of synthesizing 2D layered materials can be divided into two segments, where one is top-down and the other is bottom up. In general, top-down methods focus on thinning thick or bulk crystal down to monolayer/few layer limit by exfoliation of various ways. The original method of producing graphene is a top-down method which relies on mechanical exfoliation (repeatedly peeling) from a bulk graphite crystal[1]. Thus, top-down methods begin with a bulk crystal. Bottom-up methods typically involve the direct growth of 2D materials on a substrate.

2.1.1 Mechanical Exfoliation

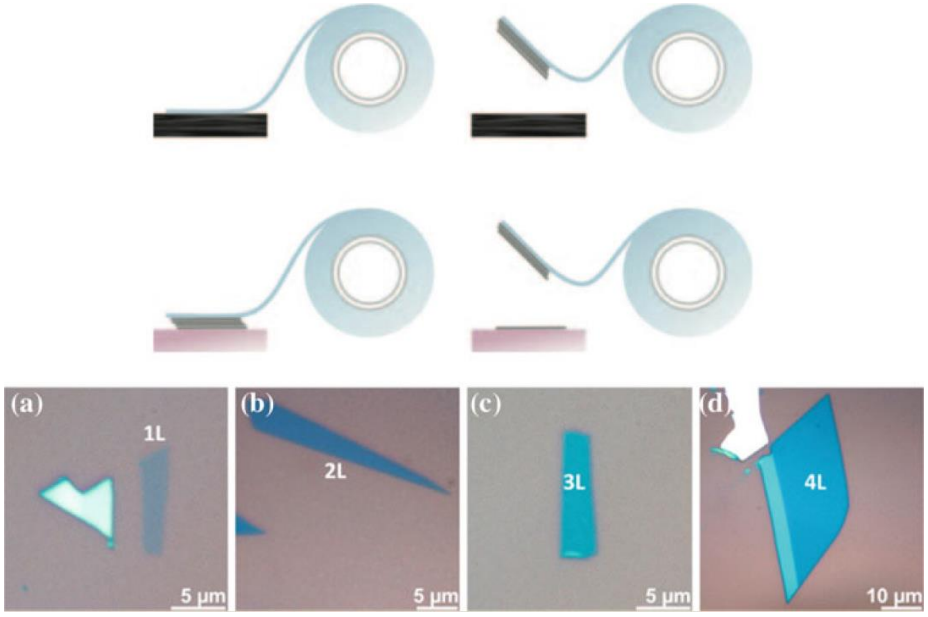


Figure 2-1 Tape exfoliation process for monolayers from bulk crystals.

Obtained crystals are used for subsequent top-down exfoliation process to produce thin layers. Mechanical exfoliation provides the simplest way to yield monolayer and slightly thicker layers (Figure 2-1)[75]. However, the size of the exfoliated is typically

small at 3-5 micron. It is reported that by using gold substrate large area MoS_2 can be exfoliated as result of the strong Au-S bonding[76]. On the other hand, liquid exfoliation provides a better yield and larger size monolayers than mechanical cleavage[7]. It can be a pure mechanical force-assisted process, such as ultrasonication or ion intercalation-assisted chemical process[77]. While the former simply involves submerging thick crystals in a suitable solvent for ultrasonication[78]; the latter is typically done by intercalating ion spices such as Li^+ in between layers followed by sonication[54].

2.1.2 Vapor Phase Synthesis

Limited by the size of and yield of mechanical exfoliation and the cleanness of samples obtained from chemical/liquid exfoliation, bottom-up methods serve the need of manufacturing clean monolayers in a scalable manner.

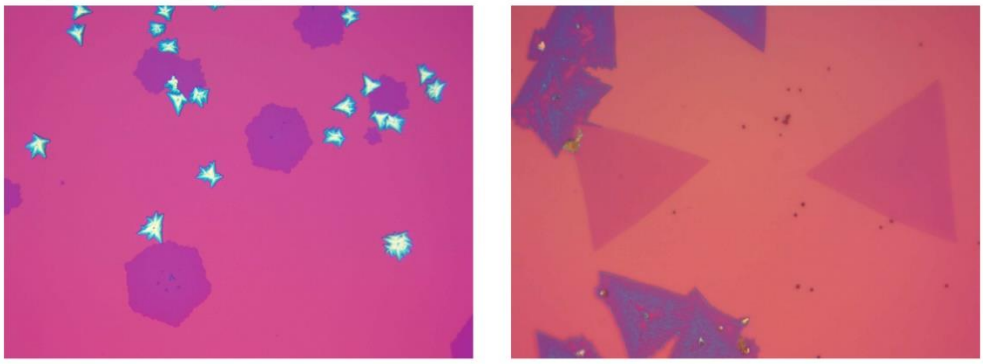


Figure 2-2 CVD system setup and optical images of grown MoS_2 monolayer on SiO_2/Si substrates.

Chemical vapor deposition (CVD) is the most popular bottom-up method for monolayer production. In a typical CVD process, precursors are heated up to a certain temperature for building up vapor pressure and those gaseous reactants are carried by inert gas flow to diffuse onto the substrate where the chemical reactions take place. The size of the product can vary from small monolayer domains to full covered substrate of

the 2-inch wafer. Compared to CVT method, CVD synthesis takes place on shorter time scales, at lower temperatures, and with more volatile precursors[79]. Owing to the relative violence of the technique, a large variety of defects can be generated and engineered in CVD grown monolayers[80].

A Recent advance in CVD growth technique has enabled the direct growth of heterojunctions of various kinds. It is worthwhile to mention that lateral heterojunctions which are hard to build by the traditional exfoliation-transfer method, is relative easier to achieve by CVD via either one-step or two-step growth[77].

2.2 Optical Characterizations

2.2.1 Raman Spectroscopy

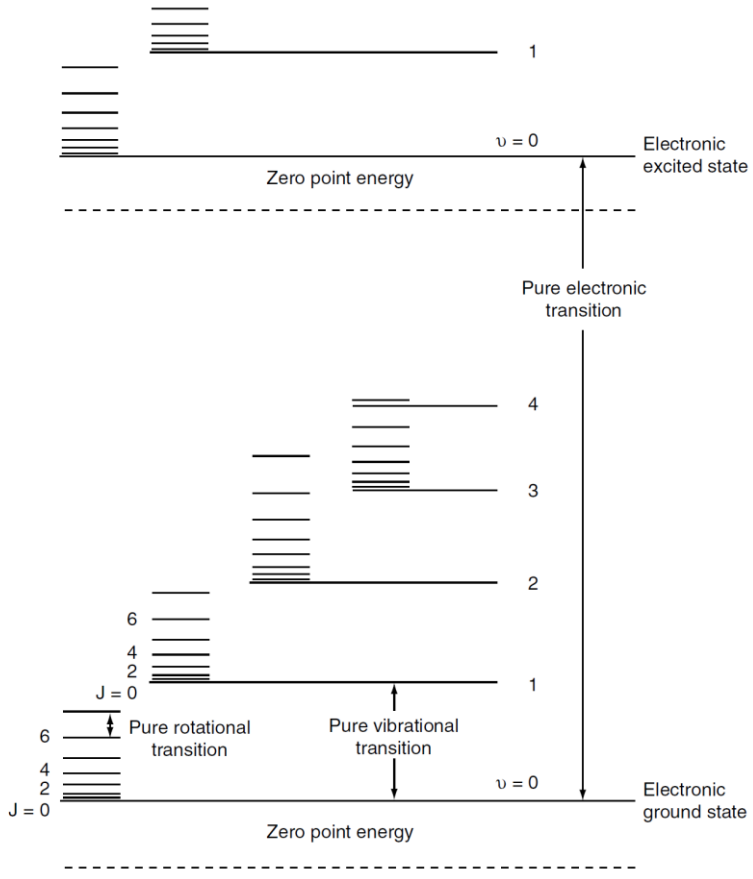


Figure 2-3 Energy level of diatom molecule model.

Raman effect is an inelastic scattering process of visible wavelength photons. The main application since its discovery in 1928 is to investigate vibrations in molecules and crystals. There are various excited states in defined materials systems and a diatom molecule model is shown in Figure 2-3 as an example[81]. Below the very high electronic states located are vibrational and rotational transitions that are typically in the range between tens to hundreds of meV.

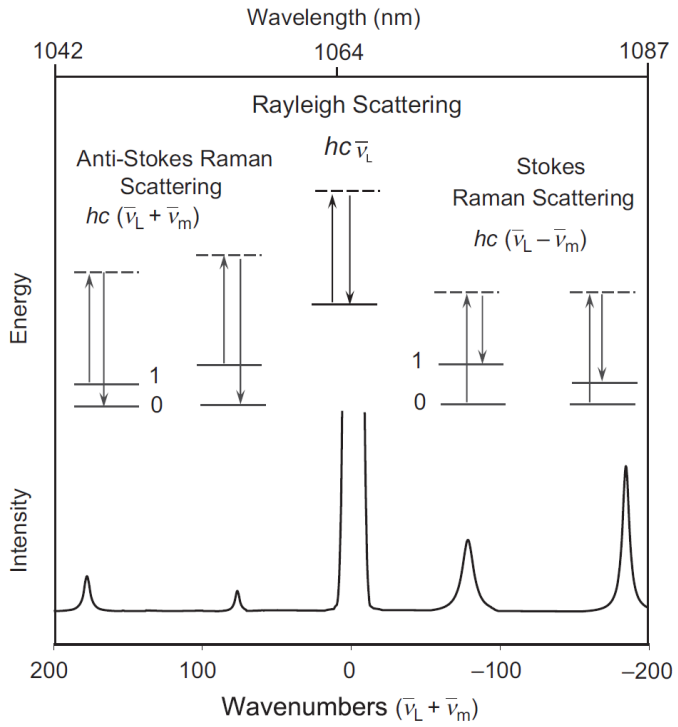


Figure 2-4 Raman spectrum showing Rayleigh, anti-Stokes and Stokes scattering lines.

Raman spectroscopy is measured by irradiating samples by an intense laser beam of visible wavelength, and the scattered light signals are collected typically in a backscattering or right-angled configuration. Scattered lights can be categorized into types: 1) Rayleigh scattering which is a strong elastic process where scattered photons have the same frequency (ν_0) as the incident laser light, and 2) Raman scattering which is a very weak (~10^{-5} of incident beam) inelastic scattering process where scattered photons

have frequencies of $\nu_0 - \nu_m$ and $\nu_0 + \nu_m$ (ν_m is a vibrational frequency of molecule or phonon mode in crystal). These two frequencies in Raman spectra are called Stokes and anti-Stokes lines, respectively (Figure 2-4)[82]. Therefore, vibrational frequency (ν_m) is measured as a shift from incident light frequency (ν_0).

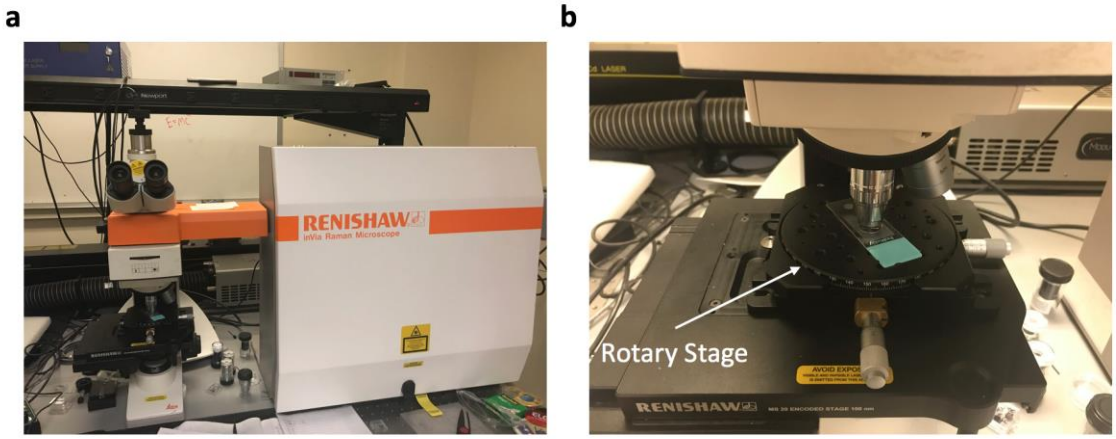


Figure 2-5 **a.** Renishaw InVia spectrometer setup and **b.** Rotary stage for anisotropic measurements.

Raman and PL measurements for the as samples were performed in a Renishaw InVia spectroscopy system (Figure 2-5a) with a 100× objective lens using a laser source with 488 nm wavelength. The laser was focused onto the sample with a spot size of ~1μm^2 and the power of 0.5 mW. Angle-dependent data was collected by mounting samples on a rotatory stage and Raman was taken every 15 degrees of sample rotation (Figure 2-5b).

2.2.2 Photoluminescence Spectroscopy

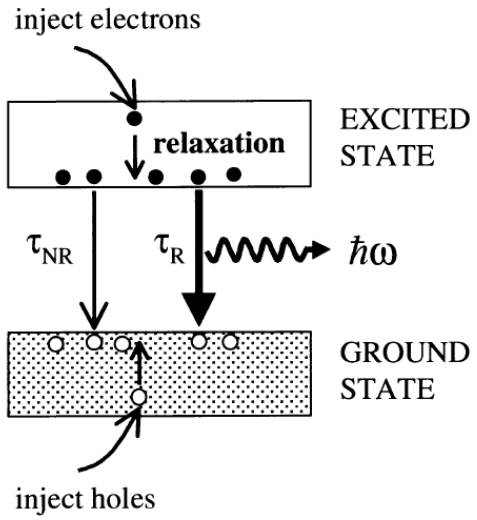


Figure 2-6 Schematic of luminescence in a solid.

As mentioned in previous section, there are various excited electronic states in crystals and they can be stimulated by ground state electrons absorbing energy from light. When electrons in excited states drop down to a lower level by radiative transitions, light is emitted and this process in solids is called luminescence as illustrated in Figure 2-6[83]. It is photoluminescence if the excited states are created by absorption of light, i.e. emission of light after absorbing photons of higher energy.

In semiconductors, interband photoluminescence occurs when a photoexcited electron in the conduction band drops back to the valence band by emission of a photon. This process reduces both electron and hole population in conduction and valence band, respectively, and corresponds to annihilation of electron-hole pairs, which is called electron-hole recombination.

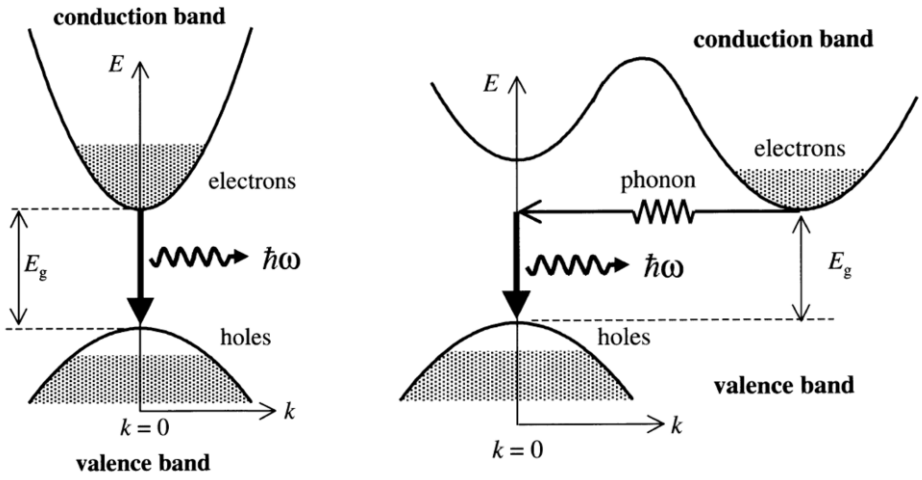


Figure 2-7 Band diagrams of direct gap semiconductor and indirect gap semiconductor.

Interband photoluminescence is mostly discussed in direct and indirect band gap semiconductors. Figure 2-7 is the schematic for a direct and indirect gap photoluminescence transition[83]. Excited electrons and holes relaxes to their lowest energy levels (CBM for electrons and VBM for holes) before luminescence happens. Since the negligible momentum of photon, electrons and holes must recombine at the same k vector. This condition is automatically fulfilled for direct band semiconductors since their VBM and CBM are located near k=0 with energy gap of Eg. The radiative lifetime is relatively short with values between 10^{-8}-10^{-9} s. Thus, the luminescence efficiency is supposed to be high. Indirect gap semiconductors, on the other hand, have much less luminesce efficiency because of the different locations of CBM and VBM in the Brillouin zone. To satisfy momentum conservation, a phonon needs to be involved (emitted or absorbed) to assist the photon emission, which makes the process second-order with longer radiative lifetime.

Photoluminescence data in this dissertation was collected in the same condition as the Raman measurements.

2.3 Electron Microscopy Characterizations

2.3.1 Scanning/Transmission Electron Microscopy

Electron microscopes are developed by the pursuit of higher resolving power for finer features in microscopic structures. The resolution of optical microscopes is limited by wavelength of visible light. The classic Rayleigh criterion for resolution of visible light microscope, which reveals that the finest distance that can be resolved, δ is given approximately by

$$\delta = \frac{0.61\lambda}{\mu sin\beta}$$

Where λ is the wavelength of the electromagnetic wave, μ the refractive index of the viewing medium and β the collecting semi-angle the magnifying lens. The term μsinβ is usually called numerical aperture and can be approximately to unity (similar formula for electron microscope is ~1.22λ/β). A simple estimation of 500 nm green light, which is at the middle of visible light spectrum, leads to a resolution of optical microscope at ~300 nm. Since the magnitude of atom size is tenths of a nanometer, better instruments need to be devised for resolving atomic structures in materials.

The discovery of matter wave by the famous de Broglie's equation links wavelength of particle to its energy. Transmission electron microscopy is based on the idea that high energy electron beam can be used as "light source" for high resolution imaging, because of the very short wavelength that can be achieved by accelerating electrons to high speed.

Electrons in TEM gain kinetic energy from acceleration by a potential drop (V), which leads to a momentum p by

$$p = m_0 v = (2m_0 eV)^{1/2}$$

Where m_0 is the electron mass. Plug above equation into de Broglie's equation

$$\lambda = \frac{h}{p}$$

where h is the plank constant, gives

$$\lambda = \frac{h}{(2m_0eV)^{1/2}}$$

which links the wavelength of electron (λ) to the accelerating voltage of the electron microscope (V). Since electrons can reach speeds close to light, a more sophisticated treatment including relativistic effects gives the equation

$$\lambda = \frac{h}{2m_0eV\left(1 + \frac{eV}{2m_0c^2}\right)]^{1/2}}$$

Simple calculations lead to relativistic wavelengths of 0.00370 nm and 0.00197nm for 100 and 300 keV accelerated electrons, respectively. They are 5 orders of magnitude smaller compared to visible light (550 nm)). Therefore, resolution is greatly improved, and atomic structures can be recorded by manipulating electron beams via magnetic lens to form images (Figure 2-8a)[84].

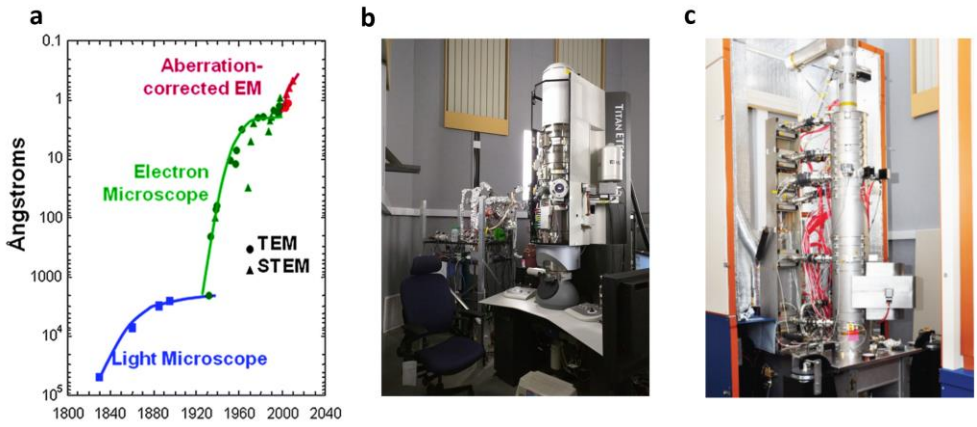


Figure 2-8 **a.** Improvement of resolving power by developing electron microscopes over the years. **b.** Aberration-corrected FEI Titan TEM and **c.** NION UltraSTEM 100.

TEM operates by illuminating a broad and parallel electron beam on specimens and a camera is used to record transmitted electrons to form images. STEM, on the other hand, is a scanning technique where the electron is focused to a small probe that scans through the area of interest. Annual detectors are used in recoding signals from annular dark field mode. The TEM used in this dissertation is aberration-corrected FEI Titan 80-300 (Figure 2-8b), in which an aberration corrector is installed to correct spherical aberration from objective lens. Aberration-corrected NION UltraSTEM 100 (Figure 2-8c) was used for collecting Z-contrast images and electron loss spectra.

2.3.2 Practical Resolution of Electron Microscope

The resolution discussed in previous section sets a theoretical limit for electron microscope. However, practical image resolution for TEM is mostly dominated by spherical aberration due to imperfections in magnetic lens system, given by[85]

$$r_{min} \approx 0.90(C_s\lambda^3)^{1/4}$$

Where r_{min} is the smallest resolvable distance between two points, C_s spherical aberration and λ the wavelength of electron beam.

Practical resolution for STEM follows a similar argument which is also dictated by the aberration in the system[86].

2.3.3 Electron Beam Radiation Damage

2.3.3.1 Knock-on Displacement

Incident electron – atomic nuclei elastic scattering to displace atoms from the crystal lattice and create point defects or sputtering of surface atoms. But there is a threshold incident electron energy below which the knock-on damage does not happen since there

is not enough energy transferred to nuclei during the elastic scattering process.

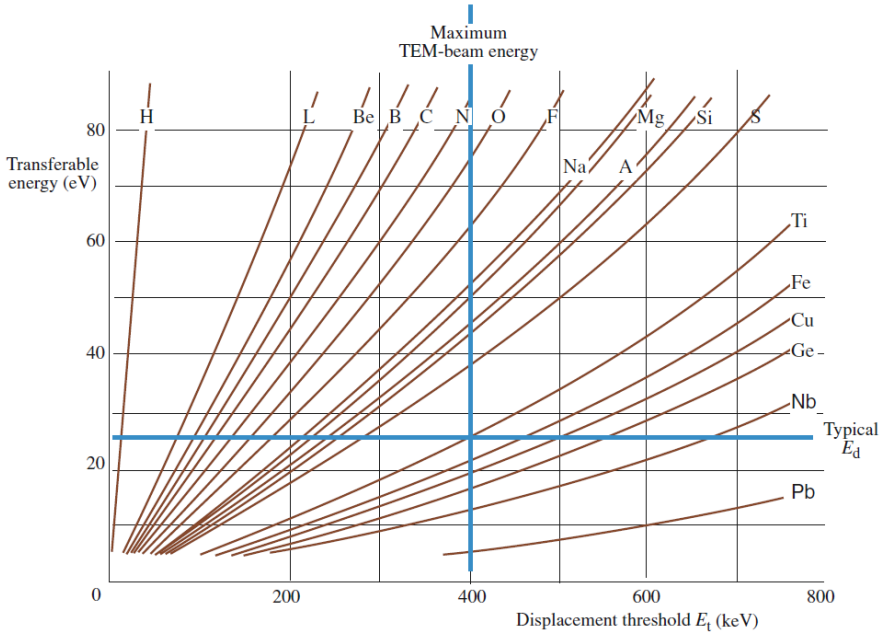


Figure 2-9 The maximum transferable energy for a range of atoms as a function of the displacement-threshold energy.

The bonding strength of each element is given by displacement energy E_d, which is sample specific property depending bonding type and crystal lattice. The total transferable energy to nuclei in sample from elastic collision with incident electron can be calculated for each element as shown in Figure 2-9[85]. If the transferred energy exceeds the displacement energy, then the atom will be knocked out from bulk or cause surface sputtering.

2.3.3.2 Radiolysis (Ionization) Damage

Incident electron (beam) - atomic electron (sample) inelastic scattering to excite single electron interband transitions or multi-electron plasmons oscillations. This is the prominent damage process in less conductive samples: once excited, it takes a longer time (than atomic vibration period) to fill the electron vacancy because of the small

electron density in the conduction band. During this time, the electron wave-functions may change (stimulated by atomic vibration, for example) and some of the excitation energy accumulated in sample may result in broken bonds[87].

2.3.3.3 Strategies for Damage Control

a) Low voltage

It is generally advised that one should always use the highest voltage that samples can withstand to get best resolution. Figure 2-10 shows that both elastic and inelastic scattering cross sections decreases as the voltage increases[88].

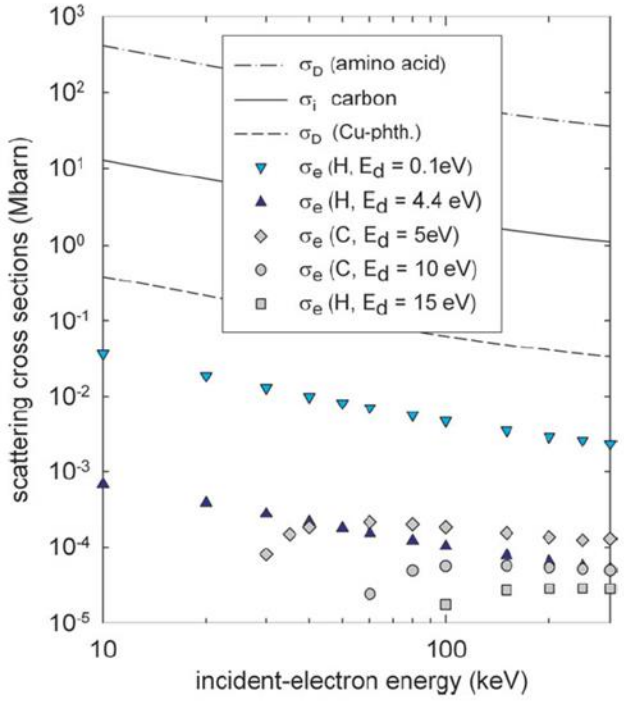


Figure 2-10 Scattering cross sections appropriate to radiolysis (smooth curves) and knock-on displacement (discrete data points) for E_0 between 10 and 300 keV.

High voltage. Smaller inelastic scattering cross sections lead to reduced radiolysis damages in polymers. But the knock-on damage increases (although elastic scattering

cross section also decreases) because more energy can be transferred to nuclei for displacement to happen (Figure 2-9).

Low voltage (< 100 keV). If the voltage is below the displacement threshold for the elements in the sample then no knock-on damage is expected to happen. However, as the inelastic scattering cross section increases at lowered voltage, ionization damage probability increases (Figure 2-10)[88]. Also, the resolution and image quality is affected as well.

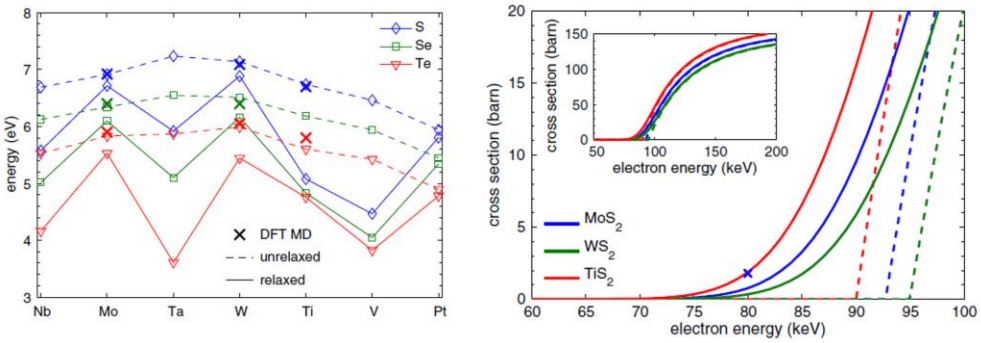


Figure 2-11 **a.** Displacement threshold energies E_d obtained from DFT molecular dynamics calculations (crosses) and formation energies of chalcogen vacancies with nonrelaxed (dashed lines) and relaxed (solid lines) geometries in transition metal dichalcogenides MeX_2, X=S, Se, Te. **b.** Cross section for sputtering a sulfur atom from MoS_2, WS_2, and TiS_2 sheets as calculated through the McKinley-Feshbach formalism and the dynamical values of the displacement thresholds. Dotted lines are the data for the static lattice, and solids lines are the results of calculations where lattice vibrations are taken into account, assuming a Maxwell-Boltzmann velocity distribution. The cross denotes the experimentally determined cross section for MoS_2. The inset shows the same data for a larger range of electron energies.

Displacement energy has been calculated for a variety of 2D monolayers and the corresponding knock-on damage electron energy for sulfur in TMDCs has been shown

experimentally to be ~80 kV (Figure 2-11)[89]. Therefore, the electron beam energy was kept at 40 or 60 kV throughout the experiments to minimize the radiation damage.

b) Low dose

Dose usually means electron exposure (often in C/cm^2), the product of incident-current density and exposure time. Reducing the exposure time and beam current can greatly minimize the total electron interacting with specimen and therefore limits the radiation damage. A smaller electron beam current can also help reduce sample degradation caused by heating.

2.3.4 Sample Preparation

2.3.4.1 Monolayer Transfer

Specimens are transferred to 200 mesh copper grids with holey carbon support film (Electron Microscopy Science) by PMMA assisted technique (Figure 2-12). The copper grid is firstly put on top of CVD-grown samples before they are coated with PMMA. Subsequently, PMMA/monolayer film is separated from the sapphire substrate by KOH etching (2 mol $^{-1}$) at 80 °C. The film is then transferred to deionized water beakers to dilute KOH residue. Finally, the PMMA was washed away by acetone solution and the sample was cleaned by IPA.

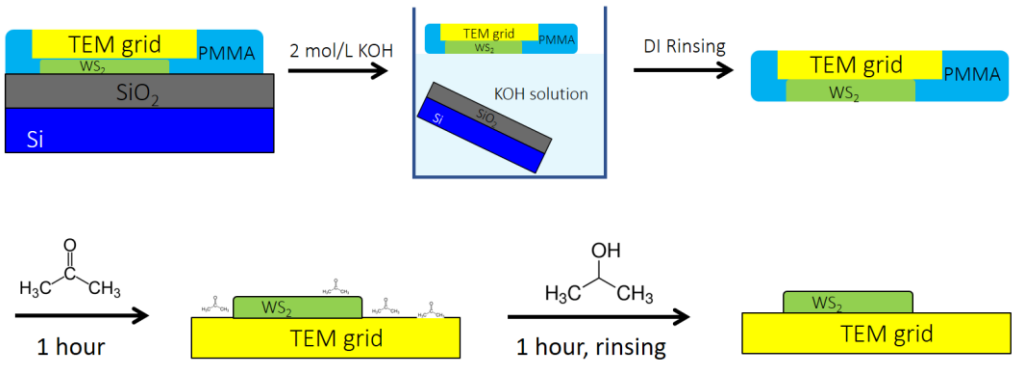


Figure 2-12 Schematic of one step PMMA-assisted transfer technique.

2.3.4.2 Focused Ion Beam Fabrication

Focused ion beam instrument can be conveniently used to prepare cross-section samples of stacks of thin films. A focused gallium ion beam is used a cutting tool to remove materials around area of interest and leave an electron transparently thin cross-section sample, which is then picked up for imaging. Figure 2-13 shows a typical workflow of FIB sample fabrication process[85]. Pt is deposited as a protective layer and markers are placed accordingly (Figure 2-13a, b). Trenches are made by ion beam bombardment on both sides of the area of interest (Figure 2-13c, d). Finally, a film thin is formed and lifted out after cutting its connection with the bulk specimen (Figure 2-13e, f).

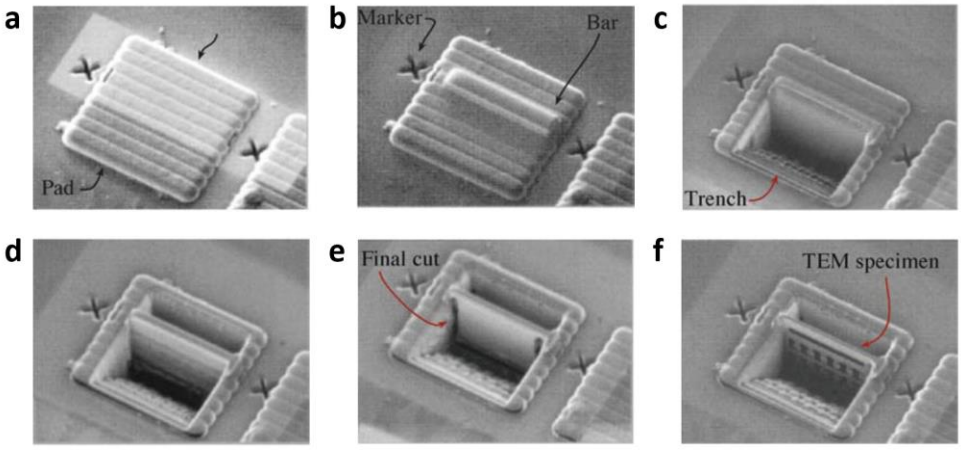


Figure 2-13 Stages in making TEM samples using a FIB instrument. **a.** The area of interest has been marked. **b.** A Pt bar is deposited to protect this area from the Ga beam. **c.** and **d.** The two trenches are cut. **e.** The bottom and sides of the slice are (final) cut. **f.** The TEM specimen is polished in place before extracting it.

2.3.5 Structural Analysis

The interaction between electron and specimen is strong and various signals are generated when samples are irradiated by high energy electron beams. The main process responsible for structural information collection is electron scattering, specifically, the elastic ones.

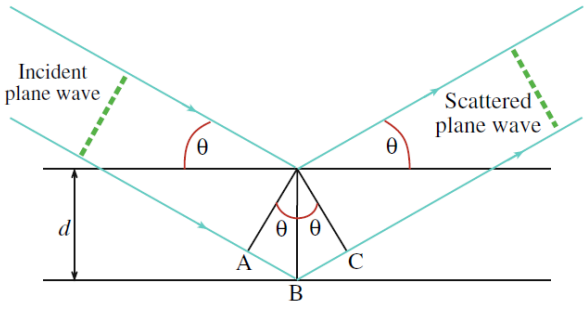


Figure 2-14 Bragg reflection for electron beam incidenting crystal plane.

The collective inelastic scattering of electrons by atoms in the specimen is called diffraction and it corresponds to the wave nature of electron. Typical diffracted angle is small (3^o), and intensity of these low angle scattering is closely related to the atomic structures in the specimen under test. The diffraction process can be treated simply as electrons reflection off crystal planes, described by Brag equation

$$n\lambda = 2dsin\theta_B$$

Where λ wavelength of electron, d the spacing of a certain crystal plane and θ_B the incident angle with respect to the crystal plane (Figure 2-14)[85].

The TEM images is the spatial distribution of scattered electrons while the diffraction patterns indicate the angular distribution of the scattered electrons. They both contain structural information of the sample (Figure 2-15) and the underlying principle is the diffraction physics[85].

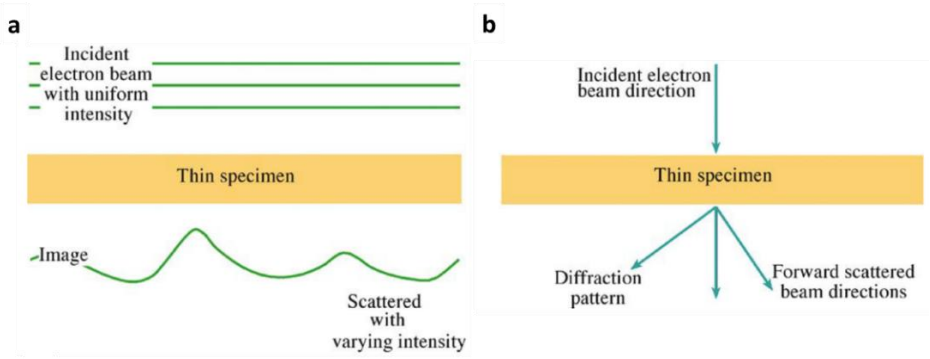


Figure 2-15 TEM image and diffraction pattern probe two aspects of the same phenomenon.

2.3.5.1 Electron Diffraction Pattern

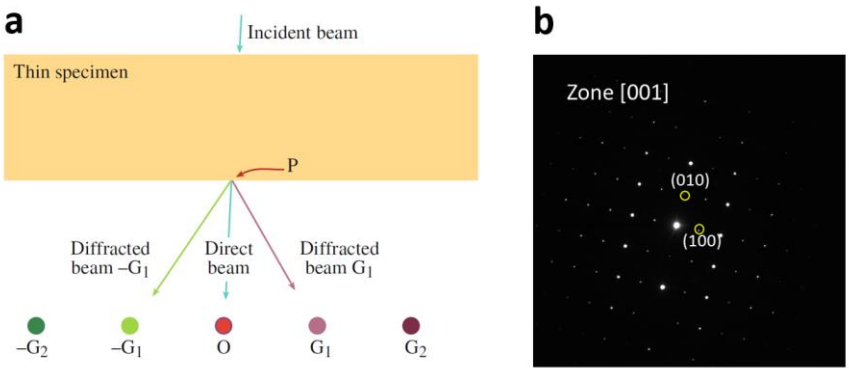


Figure 2-16 **a.** Diffracted beams generated by thin specimen scattering incident beam and **b.** example of diffraction pattern formed by recording diffracted beams on the plane perpendicular to incident beam.

As, if not more, powerful as X-ray diffraction, electron diffraction technique can be essential for direct determination of interplanar distance, crystal structure and relative orientation of crystals, although a much more complicated diffraction pattern indexing process is required.

2.3.5.2 High Resolution Imaging

For TEM, the high-resolution images are formed by phase contrast, which is the interaction between the direct (undiffracted electrons) and the diffracted electron beam.

Their phases interfere constructively or destructively when exiting the specimen, depending mainly on the nature of materials, the thickness of sample and the plane spacings.

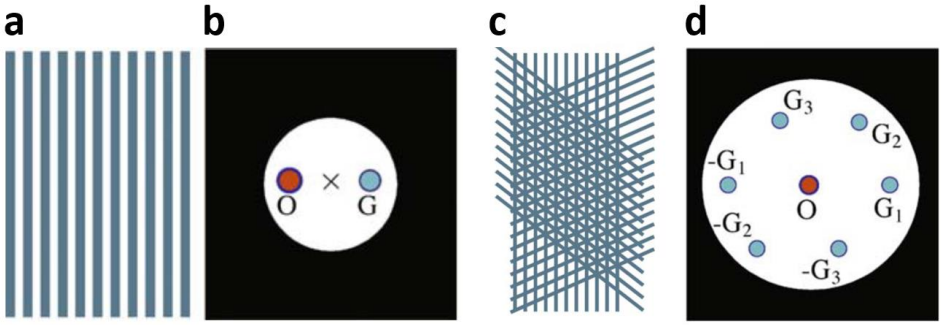


Figure 2-17 Inferences between different electron beams give rise to lattice fringes. **a.** parallel line image generated by incident beam O and diffracted beam G in the **b.** ideal tilted two beam condition **c.** The fringes with three-fold symmetry produced by interference between direct beam O and three sets of diffracted ± G beams.

Figure 2-17a, b illustrates the simplified formation mechanism of lattice fringes seen in high resolution TEM images where two beams form parallel fringes[85]. More generally, if the beam axis is on low-index zone axis, then more diffracted beams are interacting with incident beam and thus more complicated fringes are present (Figure 2-17c, d). Therefore, lattice fringes do not directly correspond to real atomic positions in the specimen, but rather lattice plane spacings, symmetry and orientation information. Interpretation of the high resolution TEM images for determining atomic arrangement in a unit cell typically involves careful matching simulation and experimental results.

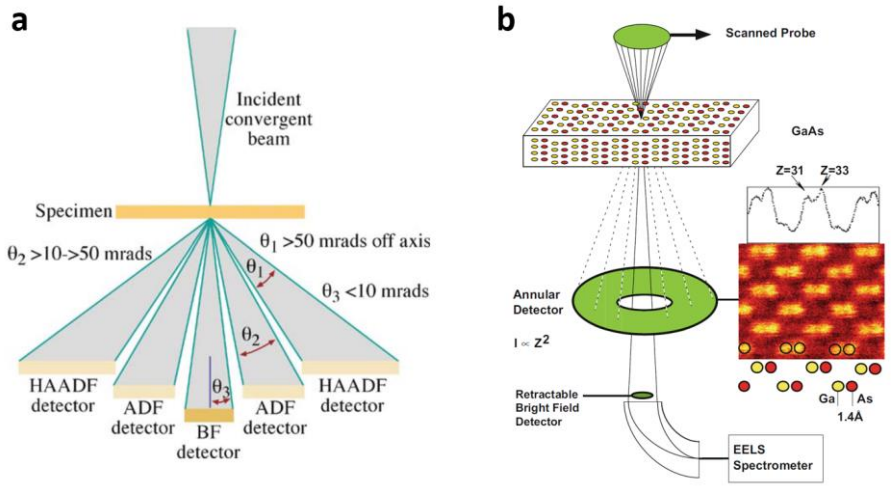


Figure 2-18 **a.** Various imaging modes in STEM by using different detectors that collect electrons scattered by different angles. **b.** 3D Schematic showing images available in the STEM as a probe is scanned across GaAs crystal by high angle annual dark field imaging mode.

STEM, on the other hand, provides directly interpretable high-resolution images using high angle annual dark field (HAADF) imaging technique. The imaging mechanism is completely different from the interference effect, which is the basis of phase contrast in TEM. By selecting electrons that are only incoherently scattered by a large angle (> 50 mrads) and excluding the direct beam for constructing images, it can form mass-thickness contrast images dominated by Rutherford scattering process (Figure 2-18)[85,90]. Therefore, HADDF mode is also called Z-contrast STEM since the scattering cross section depends quadratically on Z (atomic number).

2.3.6 Chemical Analysis

Electron microscopes are not just structural analysis tool, but also a powerful instrument for chemical analysis, because of the rich signal generated by the strong electron-matter interactions (Figure 2-19)[85]. For elemental analysis, elastic scattering is

less important, and inelastic scattering starts to play a critical role. The two analytical electron microscopy techniques used in this dissertation are briefly introduced below.

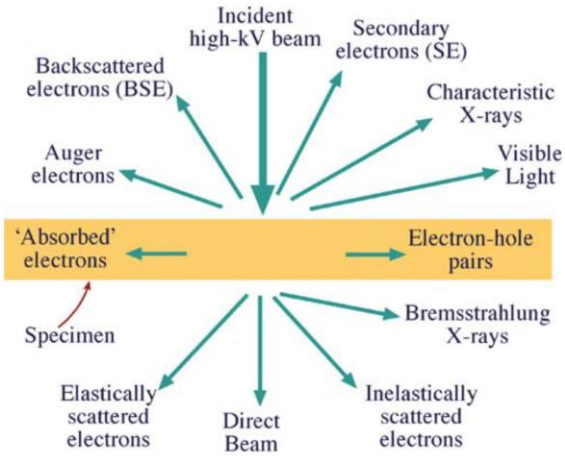


Figure 2-19 Various signal generated by irradiating specimen with high energy electron beam.

2.3.6.1 Electron Energy Loss Spectroscopy

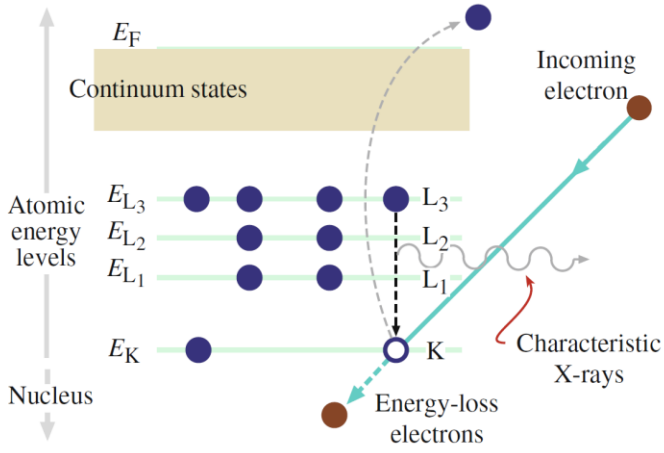


Figure 2-20 Schematic of ionization process by electron irradiation. An inner (K) shell electron is ejected from the atom by a high-energy electron. When the hole in the K shell is filled by an electron from the L shell, characteristic (Ka) X-ray emission occurs. The beam electron loses energy but continues on through the specimen.

The direct outcome of inelastic scattering event is the loss of incident electron energy, and all other signal, such as X-ray, Auger electron, are secondary or even higher order

process. Therefore, the electron energy loss spectroscopy has the highest detection efficiency with fine energy resolution (meV). High energy electron loss spectra correspond to the atomic bonding information in the specimen, which depends on atomic species as well as their chemical environment. By using a monochromator, the low electron energy loss spectroscopy can be applied to probe valence electron excitation, which collects band to band transitions to reveal bandgap information of semiconductors. In this dissertation, the state-of-art monochromated STEM is used for valence electron excitation measurement to determine band gap of 2D layers at nanoscale.

2.3.6.2 Energy-dispersive X-ray Spectroscopy

Energy dispersive X-ray spectroscopy is often referred as a complimentary technique to EELS. While EELS has better energy resolution and detects very light elements, EDX is more sensitive to heavier atoms. Two kinds of X-ray are generated during the measurement: 1) Bremsstrahlung X-ray, which is due to the loss of kinetic energy of electron when decelerating. Because kinetic energy can be released in a continuous fashion, the radiation emission is then shown in EDX spectrum as a continuous background noise. 2) Characteristic X-ray, which is the one used for elemental analysis. When the electron beam excites the sample to a high energy states, the core shell electron is promoted to conduction or vacuum state and leaves an empty state in the core level. Outer electron then will try to decay into this empty core state to reduce the total energy of the system, and the energy difference between the outer shell level and the core level is released as X-ray photon. Since the electronic levels for each atom are different, transitions between levels reflect characteristics of specific element under test. As

mentioned before, since the X-ray is secondary process (electron energy loss happens first), it has smaller cross section then EELS and thus lower collection efficiency.

2.4 Atomic Force Microscopy

Invented in 1980s, atomic force microscopy (AFM) is the successor to scanning tunneling microscopy for imaging dielectric samples with high resolution. It is a scanning probe technique where the signal is generated by interaction between a sharp tip and sample surface. Figure 2-21a illustrate the simplified operation principle of AFM in contact mode. During scanning, a laser is focused on the back of cantilever which bends when interacting with sample. Thus, the position of laser shifts accordingly and is registered by photodiode, which is then translated into height profile of sample surface after data processing.

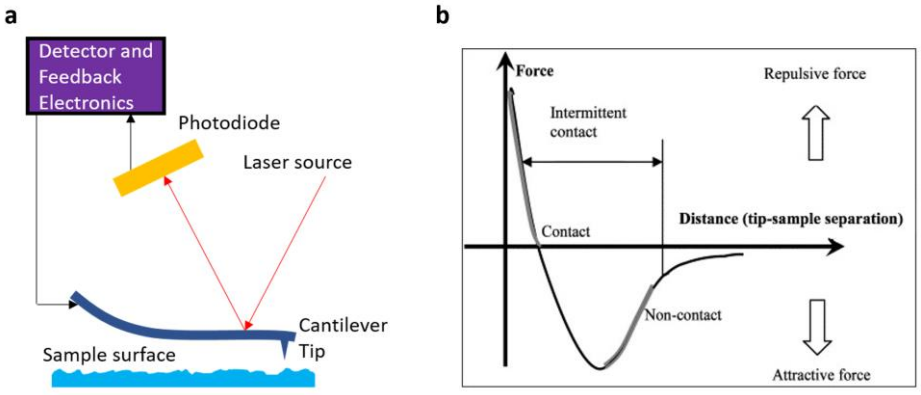


Figure 2-21 **a.** Schematic of operation principle of atomic force microscope in contact mode. **b.** Atomic force as a function of tip-sample distance.

Intermittent or tapping mode is another popular mode owning to its reduced interaction force compared to contact mode (Figure 2-21b)[91]. Especially when imaging soft samples, this mode is of particular use because of less sample damage. In tapping mode, cantilever is vibrating at a specific frequency and amplitude while being held at a

constant distance away from sample surface. As the probe scans, damping of cantilever oscillation amplitude (when tip encounters feature on sample surface) is monitored in real-time and a feedback mechanism is turned on to keep tip-sample distance constant. In this way, change in vibration amplitude can be translated into morphology information of sample surface.

AFM has been ubiquitously applied to determine surface morphology and thickness of 2D materials[92]. In this dissertation, Bruker Multimode 8 or Dimension 3100 is used to measure sample morphology in tapping mode. The scanning speed was set to 1 Hz and scanning size is 256 x 256. Data were analyzed by Gwyddion software.

Chapter 3 Architecture and Anisotropy in CVD ReS_2

This chapter is mostly adapted from our paper: Wu, K., Chen, B., Yang, S., Wang, G., Kong, W., Cai, H., Tongay, S. (2016). Domain Architectures and Grain Boundaries in Chemical Vapor Deposited Highly Anisotropic ReS_2 Monolayer Films. Nano Lett, 16(9), 5888-5894.

3.1 Introduction

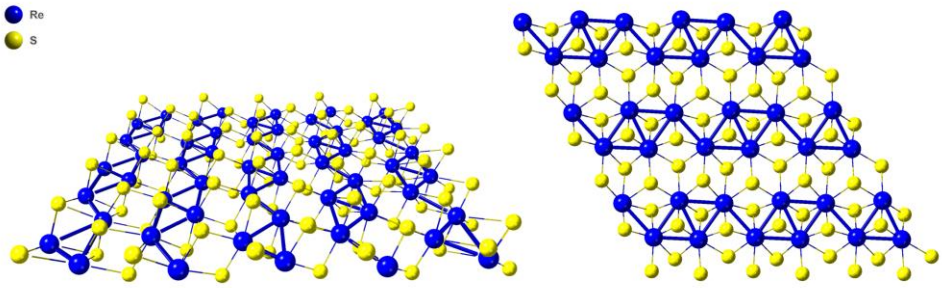


Figure 3-1 Crystal structure of ReS_2 where purple and yellow dots are Re and S atoms respectively.

Unlike typical TMDCs in 2H phase, ReS_2 is stabilized in distorted 1T' phase which leads to its unique anisotropic properties (Figure 3-1). An extra electron in Re compared to group VI transition metal such as Mo and W bonds neighboring rhenium atoms. Dimerized Re atoms form 1D chains extending along b-axis in monolayer plane. ReS_2 also exhibit layer independent properties due to extremely weak interaction between layers[47]. Each layer in bulk ReS_2, in fact, behaves as decoupled individual monolayer, which is in stark contrast MoS_2/WS_2. For example, the electronic band structure remains direct regardless of the thickness of ReS_2 layers[47].

CVD growth of ReS_2 thin layers have been reported, but ReS_2 layers tend to grow dendritic form due to anisotropic interface energy and the control over anisotropy is lost.

Here, our group report on the monolayer ReS_2 growth by CVD with noteworthy structural anisotropy and demonstrate the possibility of structurally anisotropic ReS_2CVD domain growth. Typical CVD monolayers show truncated triangular or hexagonal shapes which are not the same as those isotropic TMDC such as MoS_2 and WS_2. The current state of knowledge on domain structure of CVD MoS_2 is relatively well-established but is completely unknown for CVD anisotropic materials like ReS_2. For example, how does domain arrangement/architecture differ in ReS_2 compared to structurally isotropic TMDCs such as MoS_2 and WS_2? And how is the *b*-axis (Re-chain direction) oriented within each ReS_2 domain? Our results present the first data on this by demonstrating how subdomains arrange themselves to build larger scale flakes and demonstrate in which direction Re-chains are oriented within each subdomain. HAADF STEM images elucidate the complex structure of ReS_2 grain boundaries (GBs). Typical isotropic 2D materials (like graphene and MoS_2) have GBs extending out linearly in one direction, and vacancy defects are energetically most stable when arranged in 4|6, 4|8, 5|7, and 6|8 rings.

3.2 Experimental Details

ReS_2 is grown in a similar setup but at a lower temperature as shown in Figure 3-2. Sapphire substrates are placed on the top of an alumina boat containing ammonium perrhenate (Sigma-Aldrich 316954, NH_4ReO_4, 99%) precursor. This ceramic boat was placed at the center of the heating zone of the furnace, and sulfur precursor was placed approximately 18.5 cm upstream from the NH_4ReO_4 precursor. The monolayer growth was performed at atmospheric pressure (ATM), and precursors were transported to the substrate high purity argon flow. Samples were first heated to 300 °C (100 sccm Ar flow), and flow was gradually decreased to 50 sccm at the growth temperature

(490−520 °C). Sulfur precursors were sublimated at 350−420 °C temperature range and carried to the surface by Ar flow. Growth was carried out at 490−520 °C for 25 min followed by controlled cooling (5 °C min^{-1}) to 420 °C and fast cooling (>10 °C min^{-1}) to room temperature.

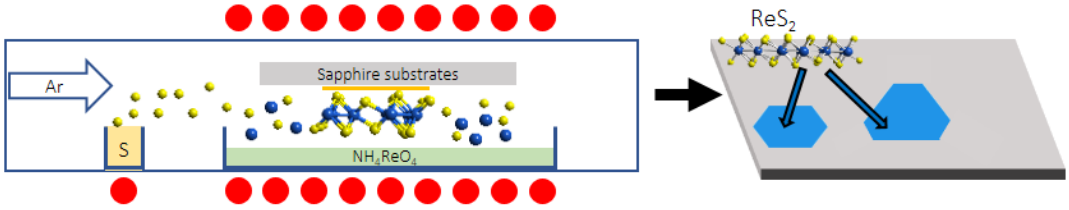


Figure 3-2 Schematic of CVD ReS_2 growth on sapphire.

3.2.1 Electron Microscopy Characterizations

CVD grown samples are subsequently transferred to 200 mesh copper grids with holey carbon support film (Electron Microscopy Science) by PMMA assisted technique. The copper grid is firstly put on top of CVD-grown samples before they are coated with PMMA. Subsequently, PMMA/monolayer film is separated from the sapphire substrate by KOH etching (2 mol $^{-1}$) at 80 °C. The film is then transferred to deionized water beakers to dilute KOH residue. Finally, the PMMA was washed away by acetone solution and the sample was cleaned by IPA.

High resolution imaging and valence electron energy loss spectroscopy were performed using Nion 100 UltraSTEM. It is a high-resolution monochromated EELS STEM system equipped with a Nion high energy resolution monochromator and a modified Gatan Enfinium EEL spectrometer. The energy resolution measured from the half width of the zero-loss peak was set to be 60 meV. To improve S/N, zero loss peak (ZLP) was cut off from 0.5 eV. The accelerating voltage was 60kV, the probe size was

about 0.31 nm, and the probe current was approximately 12 pA. HAADF images were taken with 30 mrad convergence angle and 80-200 mrad collection angle.

3.2.2 Raman Spectroscopy

Raman measurements for the as grown samples were performed in a Renishaw InVia spectroscopy system with a 100× objective lens using a laser source with 488 nm wavelength. The laser was focused onto the sample with a spot size of ~3μm^2 and the power of 0.5 mW. Angle-dependent data was collected by mounting samples on a rotatory stage and Raman was taken every 15 degrees of rotation.

3.2.3 AFM characterizations

Samples are scanned by Dimension Multimode 8 with tapping mode. The scanning speed was set to 1 Hz and scanning size is 256 x 256. Data were analyzed by Gwyddion software.

3.3 Results

3.3.1 Growth Characteristics

At growth temperature, ammonium perrhenate decomposes into Re_2O_7:

$$NH_4ReO_4 \rightarrow Re_2O_7 + NH_3 + H_2O$$

And subsequent oxides complexes continue to be reduced by vaporized sulfur gas carried by Ar to form ReO_2 which is further sulfurized to ReS_2:

$$ReO_2 + S \rightarrow ReS_2 + SO_2$$

After initial sulfurization and formation of the ReS_2 nucleation centers at random locations, conventional growth mode such as layer by layer and dendritic growth apply. Optical images (Figure 3-3a and b) show that the grown ReS_2 monolayers crystalize mainly in the shape of hexagons and truncated triangles. The hexagonal ReS_2 domains

favorably orient themselves in two distinct geometries on the substrate (red and black hexagons in Figure 3-3a), which is in large contrast to ReS_2 growth on amorphous SiO_2 know to yield randomly oriented ReS_2 domains. It is also noteworthy to highlight that ReS_2 monolayers are more likely to form close to the step edges of the sapphire subtract compared to center area of the substrate. This is in line with previous theoretical and experimental studies showing a substantial reduction in the energy barrier of nucleation close to the step edges[67,68]. Therefore, we conclude that similar catalytic processes are also involved in nucleation and diffusion of ReS_2 monolayer growth on sapphire wafers, which lead to preferentially oriented monolayer hexagons.

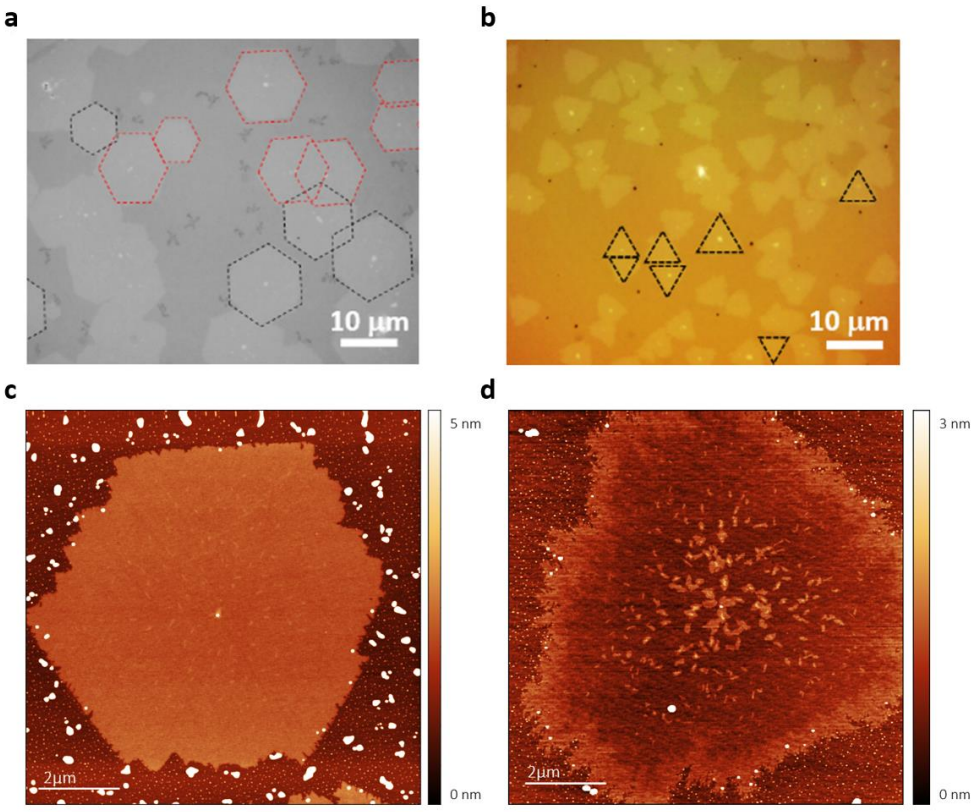


Figure 3-3 Optical images of **a.** hexagonal and **b.** truncated triangular ReS_2 monolayers. **c.** AFM images of hexagonal and **d.** truncated triangular ReS_2 monolayer.

Figure 3-3c and d are two representative AFM images of ReS_2 truncated triangle and hexagon. Unlike WS_2 and other isotropic TMDCs with 2H structure, where the highly symmetric (100) growth plane forms perfect triangle or hexagon with clearly defined edges, ReS_2 monolayers grow without sharp edges in both truncated triangle and hexagon configurations. Instead, features of dendritic growth can be observed which has been attributed to the anisotropic interface energy of ReS_2[67,68]. DFT simulations have been carried out to reveal the origin of the anisotropic interface energy that stabilizes ReS_2 in the form of dendritic growth. Calculations point out that the exposure of dimerized Re-Re atoms at edges are energetically unfavorable and sulfur atoms tend to migrate to cover those exposed Re atoms[65]. Migrated sulfur atoms may stay in a plane to continue 2D growth or move out of a plane to initiate to second layer growth on top. It is worth noting that more dendritic features are present in truncated triangles (Figure 3-3d) than hexagonal ones, indicating less ordered growth in triangular ReS_2 monolayer, which is closely related to anisotropic properties and will be discussed in later sections.

3.3.2 Effect of Growth Conditions

The temperature dependent studies in the 490-520 ^oC range reveal that increasing the temperature decreases the nucleation density but yields larger sized flakes at atmospheric pressure (Figure 3-4a, c). This finding is consistent with previous studies in graphene and MoS_2 monolayers. However, ReS_2 monolayers grown at higher (>520 ^oC) temperatures take more complex shapes with multi-layer growth, thus the ideal temperature for the high-quality formation of these triangular flakes appears to be in the range of 490-520 ^oC. In our studies, we find that the growth temperature, initial loading amount of NH_4ReO_4 and overall flow-rate make large changes in overall coverage and domain structure of

ReS_2 layers (Figure 3-4d, f). For example, increasing the NH_4ReO_4 precursor amount from 10 mg to 50 mg at 500 ^oC and 50 sccm flowrate, results in much smaller domain sizes and higher nucleation densities due to much increased Re intermediate oxide concentration. This implies that NH_4ReO_4, i.e., rhenium sub-oxides, controls the nucleation density and large-area growth in agreement with similar findings for MoO_3 in MoS_2 growth. High flow rate of carrier gas may promote the mass transfer that contributes to the increase in the crystal growth rate. In this case atoms do not have enough time to move into the right lattice locations, where crystal domains could have the lowest surface free energy, and the probability of defect formation increases therefore under high flow rate conditions, the ReS_2 crystals are more likely to grow under kinetic conditions which is resulting in the formation of dendritic morphologies rather than the thermodynamic ones. Similarly, decreasing the flow-rate from 50 sccm to 10 sccm significantly increases the domain sizes and stabilizes hexagonal features possibly due to much wider diffusion boundary layer and limited precursor supplies in line with trends for NH_4ReO_4 precursor amount. Overall, it appears that hexagonal ReS_2 monolayers are synthesized at low temperature, NH_4ReO_4 precursor amount, and flow-rate conditions,

whereas triangular features are observed at slightly higher temperatures.

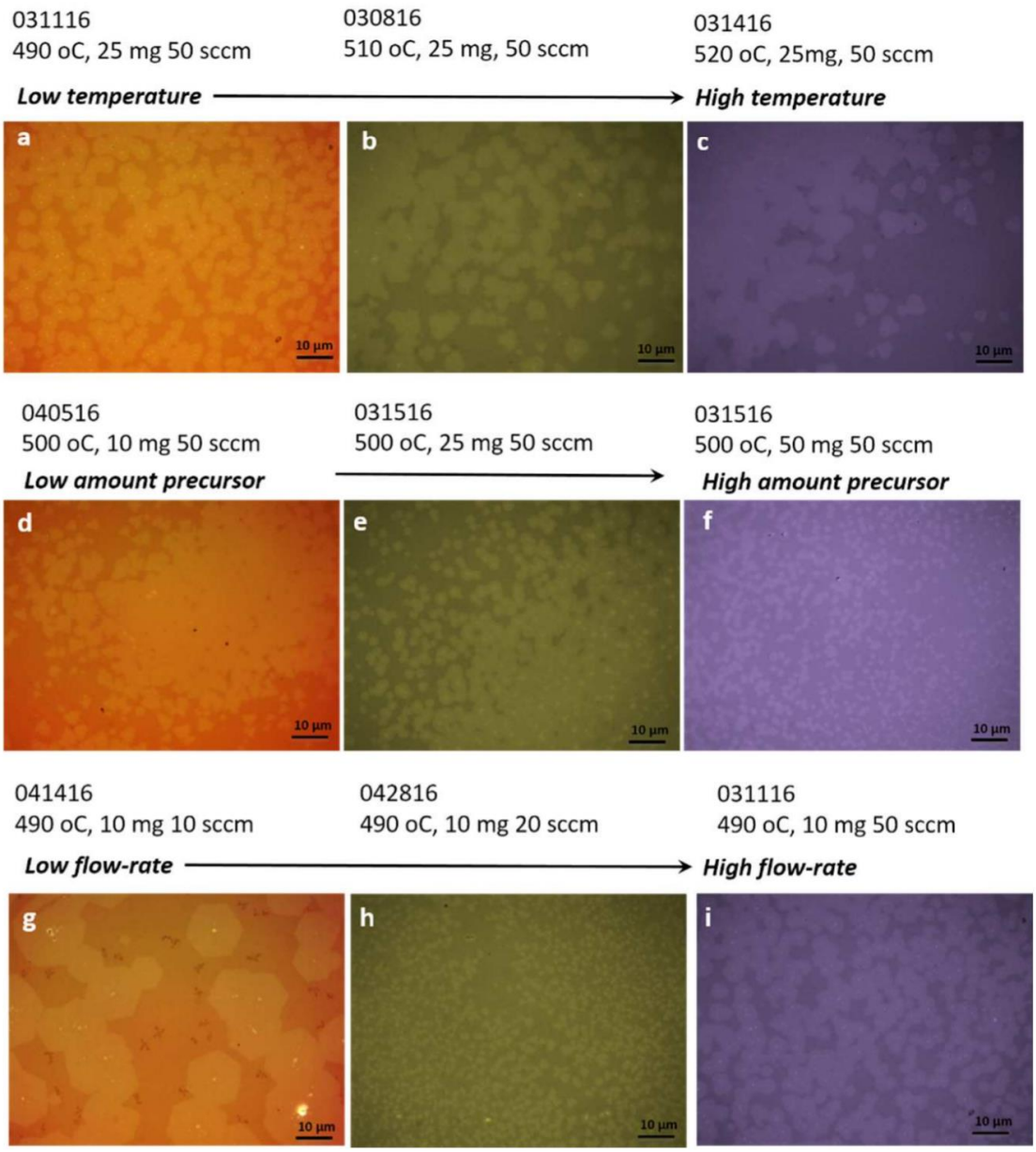


Figure 3-4 Optical images taken from ReS_2 monolayers deposited onto c-cut sapphire substrates at various conditions such as **a-c** low to high temperatures, **d-f** low to high precursor amount, and **g-i** low to high gas flow-rates.

3.3.3 Architecture and Orientation of Subdomains

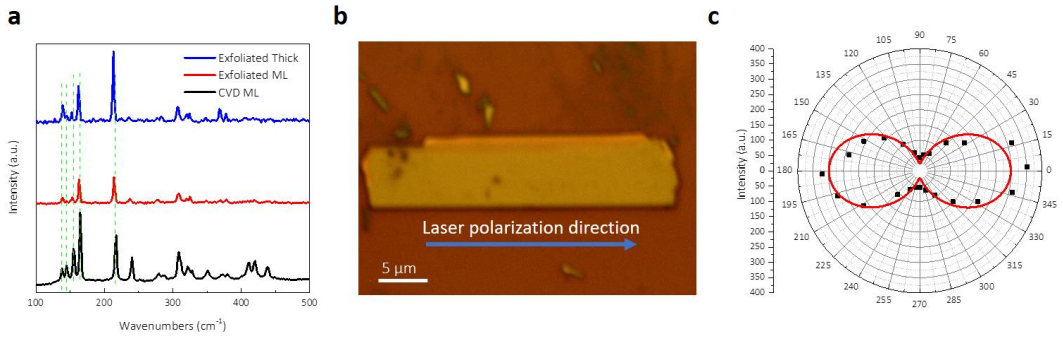


Figure 3-5 **a.** Raman spectra of ReS_2 fabricated by different methods. **b.** Exfoliated ReS_2 thin layer and **c.** Its angle-resolved Raman plot of peak 214 cm^{-1}.

ReS_2 has relatively rich Raman modes compared to other MX_2 materials due to its lower symmetry by 1T' distorted structure and a higher number of atoms in a unit cell (4 Re and 8 S atoms). There are in total 18 Raman active modes[93] and a comparison of Raman spectra taken on bulk, exfoliated monolayer and CVD grown monolayer is given in Figure 3-5a. The negligible difference in Raman shifting between bulk and monolayer ReS_2 is attributed to the extremely weak-bounded nature of bulk ReS_2 that behaves as decoupled layers. Sharp Raman peak (4-5 cm^{-1} FWHM) of CVD grown samples reveal its high crystallinity which is comparable to exfoliated one.

The fundamental Raman peaks in the range between 100 to 400 cm^{-1} provide useful information about ReS_2. Among those peaks, 152, 163, 214 and 237 peaks are all assigned to in-plane vibrations of Re atoms[93], which is important in that the structural anisotropy is due to the dimerization of Re atoms. Indeed, those peaks are found to have maximum intensity when Re-chain axis are aligned with the polarization of excitation laser[49,94,95]. Angle-resolved Raman plots of those peaks show a twofold symmetry that can be fitted into $\cos^2(\theta)$ where θ is the angle between the laser polarization and the b-

axis of ReS_2. Thus, anisotropic directions of ReS_2 can be identified by tracking the maximum intensity of the corresponding peak in a polar Raman plot. Here, the 214 cm^{-1} peak is used as a representative peak for probing the Re-chain directions in our sample as it presents the largest maximum to minimum intensity ratio. Figure 3-5b shows an optical image of exfoliated ReS_2 flake annotated with the initial laser polarization direction. The horizontal polarization is set to be the 0 degree and successive Raman measurement is performed on the same spot with 15 degrees of polarization rotation each step. The complete Raman polar plot by 214 cm^{-1} (Figure 3-5c) shows strong Raman anisotropy. However, it is known from previously reports that CVD ReS_2 has reduced anisotropy because of poor crystallinity resulting from dendritic growth[65,96]. AFM images reveal the dendritic growth nature of the our monolayers where the edges and growth directions are not well-defined, which leads to the question of whether these monolayers retain their structural anisotropy. As mentioned previously, triangular ReS_2 monolayers (Figure 3-3d) show high degree of dendritic growth at the edge and its polar Raman shows isotropic behavior, suggesting minimum amount of anisotropy.

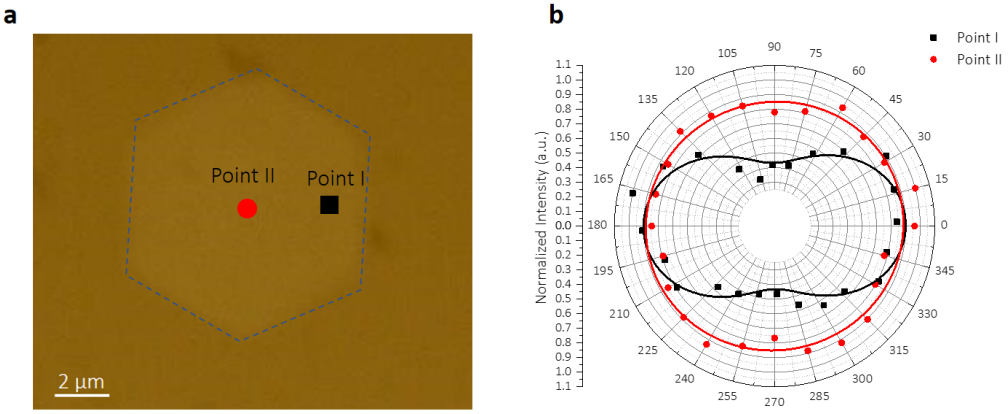


Figure 3-6 **a.** Optical image of the point I and II on hexagonal ReS_2 and **b.** corresponding polar Raman plots.

On the other hand, a polar Raman measurement performed at the point I on hexagonal CVD ReS_2 (Figure 3-6a) is plotted as black squares in Figure 3-6b. The good fit of $\cos^2(\theta)$ elucidate anisotropic properties of CVD samples. However, similar polar Raman measured on center of the hexagon (point II in Figure 3-6a) shows a rather isotropic response (red dots in Figure 3-6b).

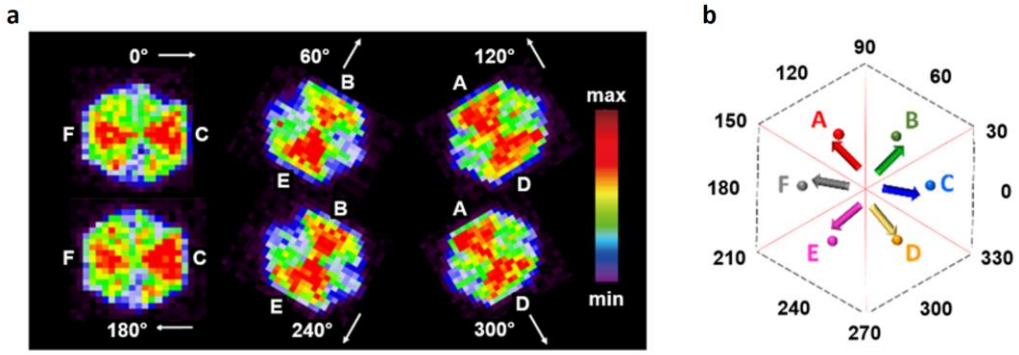


Figure 3-7 **a.** Raman mapping of 214 cm^{-1} peak on hexagonal ReS_2 with different laser polarization angles. **b.** Illustration of six subdomains in a hexagonal monolayer and their anisotropy directions.

To better understand the domain structure of ReS_2 monolayers and determine Re-chain direction, Raman intensity mapping at the 214 peak is performed on the ReS_2 hexagonal monolayer. First, one edge of the hexagon is aligned with incident laser polarization and then polarization angle is changed by 60^o with respect to sample in the next mapping. The result of six Raman mapping is shown in Figure 3-7a. Mapping data demonstrates that there are always two regions of the hexagon with at least an order of magnitude more signal then others. Most importantly, these individual segments (subdomains that are ~10 μm in size) appear to be triangular and the most "bright" two triangles point opposite to each other. Thus, six different domains in a hexagonal monolayer flake can easily be identified. This finding convincingly elucidates that

hexagonal flakes are not constructed by randomly oriented Re-chains as one is tempted to assume by the dendritic grown feature observed by AFM, but instead are made of six well-defined subdomains. These domains appear to have grain boundaries roughly running from 30° to 210°, 90° to 270°, and 150° to 330° as highlighted by red lines in Figure 3-7b. This suggests that Re-chain direction is closely aligned for subdomains located across from each other. We note that polarization dependent response within triangular subdomains (constituting the hexagon itself) is in stark contrast to group-VI TMDCs domains with no polarization dependence in Raman intensity mapping due to their highly isotropic crystal structure.

With the general anisotropic information of hexagonal ReS_2 in mind, we probe the Re-chain direction (anisotropy) in each individual domain. Measurement is performed by tightly focusing the laser to an area of 3-micron meter inside each triangular domain and therefor the anisotropic response is from the specific domain being probed only. Angle-resolved measurements on each triangular subdomain, however, yield two-lobed polar plot and the orientation of *b*-axis with respect to laboratory axes can be identified by fitting to $y=A+B^* \cos^2(\theta + \alpha_0)$. Results show that 214 cm^{-1} Raman intensity in domain A, B, C, D, E, and F reaches its maximum at 136^o, 50^o, 348^o, 303^o, 214 ^{o}, and 160^o. the following can be concluded from the angle-resolved Raman spectroscopy data: (i) Opposite triangular domains (A–D, B–E, and C–F) have the nearly similar *b*-axis orientation (180° rotation), which explains why domains across from each appear bright at a given polarization angle (Figure 3-7a). (ii) *b*-axis of domain A, B, D, and E appear nearly at the grain boundary whereas *b*-lattice direction runs perpendicular to the edge in domain C and F. Based on these, the proposed domain structure is depicted in Figure 3-

7b (each arrow indicated anticipated Re-chain direction). While individual domains yield strongly anisotropic response, middle of the hexagon or probing the whole hexagonal ReS_2 (using lower magnification larger area probing spot) yields isotropic response in Figure 3-6b. This suggests that each hexagonal flake behaves as if isotropic MoS_2 at macroscale, but each subdomain has the well-defined structural anisotropy.

3.3.4 STEM Characterizations of Grain Boundaries

Results so far indicate that the anisotropy of ReS_2 flakes is largely modulated by grain boundaries. To achieve a controlled anisotropic growth, one needs to know how and why grains are formed and arranged. For some isotropic 2D materials, such as graphene, h-BN and MoS_2, the formation of their grain boundaries has been well understood. Grain boundaries in graphene can be defined as arrays of dislocations formed by mainly 5|7 carbon rings and a variety of different kinds of carbon arrangements mediated by carbon vacancy (V_C)[11]. It has been also reported that grain boundaries of h-BN and MoS_2, contain similar vacancies or sulfur substituted 4|6, 4|8, 5|7, and 6|8 B–N and Mo–S rings[12,80]. However, grain boundary structure of ReS_2 is anticipated to be vastly different from other 2D systems due to the anisotropy in interfacial energy and a vast number of different atomic arrangements around defect sites. In fact, there is limited understanding about the detailed grain boundary structures in anisotropic 2D systems such as ReS_2 and $ReSe_2$.

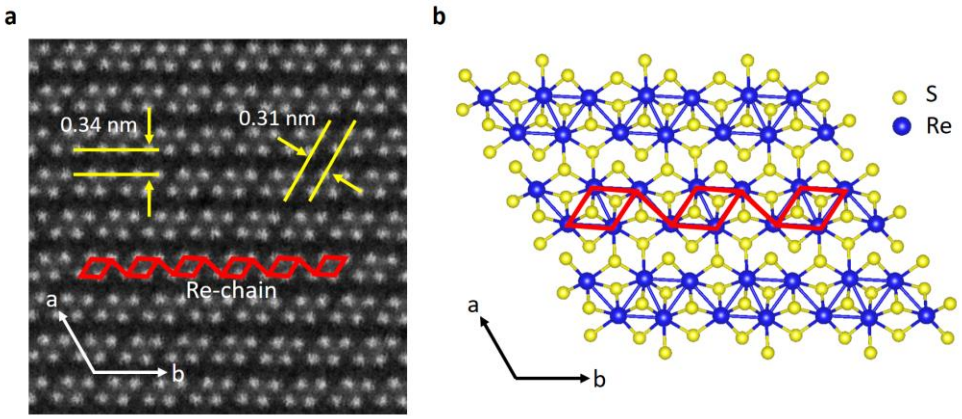


Figure 3-8 **a.** HDAAF STEM images taken from pristine ReS_2 monolayers area showing the quasi-1D nature of synthesized monolayers and **b.** schematic depiction of ReS_2 monolayers and b- and a-axis lattice directions.

Based on the understanding of lost anisotropy due to dendritic growth, we hypothesize that similar dendritic features appear at grain boundaries, which are related to reduced anisotropic response at these locations. STEM is used for atomic scale characterizations to help understand local lattice order in monolayers. High resolution imaging is typically regarded as a local characterization technique and may not be representative for general flake properties, especially when it can introduce extrinsic defects by sample prep and irradiation. As a result, STEM images tend to overestimate the amount of intrinsic defects. To minimize the perturbation introduced by electron beam radiation, we applied low voltage imaging (60 kV) technique, which is effective in preserving intrinsic structural features of ReS_2, as demonstrated by the defect-free images shown in Figure 3-8a. Rhenium atoms provide most of the image contrast because of its large atomic number in HADDF Z-contrast STEM images. The Re-chains and their directions are clearly resolved and match well with the crystal model shown in Figure 3-8b.

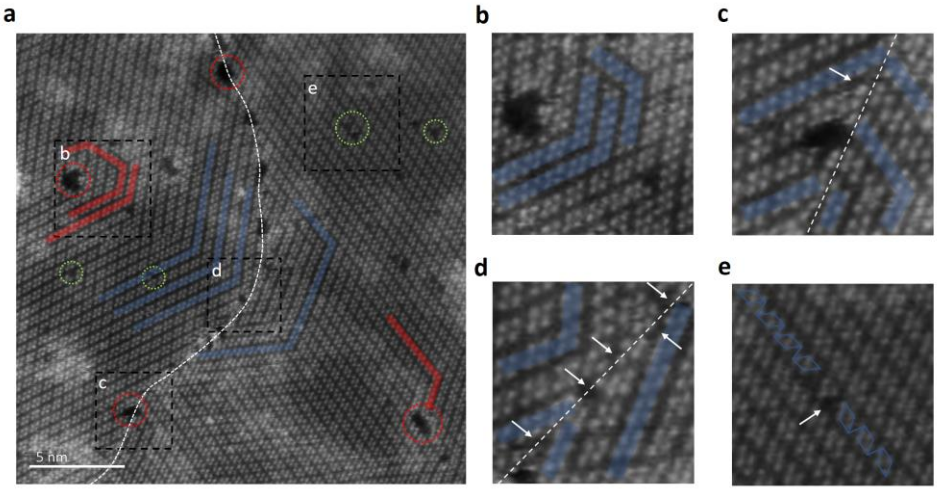


Figure 3-9 **a.** HRSTEM image taken at ReS_2 grain boundaries and specific zoom in images from **c., d.** grain boundary region and **b., e.** away from the grain boundaries.

Before discussion of defects in STEM images, it is worth noting in our experiments that the isotropic responses by polar Raman spectroscopy have been constantly observed across multiple CVD monolayers, which is carried to the prepared samples for STEM characterizations. Since we fixed imaging parameters to record high resolution images and the pristine area does not degrade over time, it is reasonable to believe that images recorded at grainboundaries locations are affected by beam irradiation to a minimum level, and therefore reflect the features of as grown sample. Figure 3-9 shows rather complicated features at grain boundaries of ReS_2. Apart from the typical anion vacancies, other structural imperfections also exist away from the boundary region. For example, green dashed circles in Figure 3-9a highlight commonly observed S–Re–S pair vacancies (triangular black missing patches, Figure 3-9e). These defects change atomic level local interactions sufficiently enough that it can lead to 180° in-plane chain rotation by Re slip motion as shown in Figure 3-9e. Interestingly, the atomic structure around cluster defects (red dashed circles in Figure 3-9b) is heavily influenced by the strain imposed through

these imperfections. A closer look at the highlighted false-color strips (Re-chains) demonstrates that these chains do not extend along infinitely but instead change their directions in multiples of 60° around these cluster defects. Because many defects are present at the boundary, similar *b*-axis rotation action is apparent near grain boundary (blue strips near boundary Figure 3-9c, d). We note that these observed defect behaviors are largely different from other isotropic 2D systems, such as graphene and MoS_2, and provides valuable insight into the structure of ReS_2 grain boundary.

3.3.5 Effects of Defects on Anisotropy

Raman mapping and angle-resolved measurements show that the CVD ReS_2 monolayers are synthesized with well-defined anisotropy in each crystal domains. However, the degree of microscale structural anisotropy of ReS_2 subdomains is likely to be modulated by alterations in Re-chain direction imposed by a variety of imperfections such as cluster defects and vacancies. Therefore, uncontrolled anisotropy (caused by imperfections) at nanoscale prevents polarization selection and reduces the polarization dependent material properties. For example, near defect rich grain boundaries in which Re-chain direction is strongly altered by the presence of a variety of vacancy defects and thus minimum anisotropy is observed by Raman spectroscopy at these regions. The structural anisotropy within ReS_2 subdomains is quickly recovered away from grains boundaries in relatively defect-free regions, and these regions display rather large anisotropy. Based on our findings above, we predict that structural anisotropy and polarization-dependent properties will be negligible for layers with a high density of defects due to randomly oriented Re-chains caused by imperfections. It is also anticipated that achieving macroscale (chip-scale) ReX_2 (X = S and Se) with large anisotropy will be

a large challenge, and either more sophisticated molecular beam epitaxy (MBE) technique needs to be utilized to achieve large area single crystalline ReS_2 layers or selective epitaxy routes need to be developed for fabrication at a targeted area with well-defined crystalline anisotropy.

3.4 Discussions

ReS_2 can be grown by CVD retaining its in-plane anisotropy. Angle-resolved Raman spectroscopy reveals that obtained highly crystalline ReS_2 flakes have well-defined anisotropic sub-domains, which also allowed us to determine the Re chains (*b*-axis) directions within each sub-domain in both hexagonal and truncated triangular flakes. This is surprising since anisotropic interfacial energy stabilizes the completely random dendritic growth. HR-STEM images show that multiple defects exist at grain boundaries. The cluster and vacancy defects at the grain boundaries can cause Re chains to change the directions to different angles; those defects located away from the grain can either cause Re chains to change direction in multiples of 60°, or even rotate chains in 180 degrees around their own *b*-axis. Therefore, the overall randomization of ReS_2 chains at grain boundaries results in the loss of anisotropy.

From manufacturability and application perspective, further work may be focused on achieving large anisotropic ReS_2 monolayer flakes for chip scale applications. To achieve this goal, either more sophisticated selective epitaxy routes need to be developed for fabrication at a targeted area with well-defined crystalline anisotropy. Besides, further insights will also be given to alloying this material ($ReS_xSe_{(1-x)}$) and introducing defect since these two routes are known to affect the anisotropic response.

Chapter 4 Rhenium Disulfide/Tungsten Disulfide Heterostructures

This chapter is mostly adapted from our paper: Chen, B., Wu, K., Suslu, A., Yang, S., Cai, H., Yano, A., Tongay, S. (2017). Controlling Structural Anisotropy of Anisotropic 2D Layers in Pseudo-1D/2D Material Heterojunctions. Adv Mater, 29(34).

4.1 Introduction

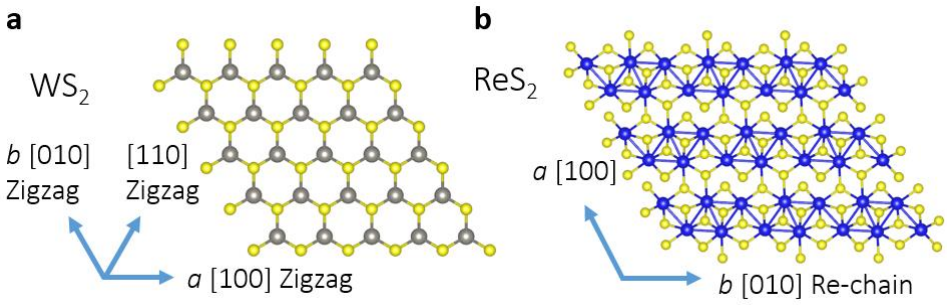


Figure 4-1**a.** Structure model of WS_2 and **b.** ReS_2 where yellow, grey and purple dots are sulfur, tungsten and rhenium atoms, respectively.

Semiconducting two-dimensional transition metal dichalcogenides (sTMDC) are a class of materials that are potential candidates for a variety of optoelectronic and photonic applications owing to their unique optical, electronic and magnetic properties stemming from quantum confinement effects[7]. While group VI-TMDCs (MoS_2, WSe_2, etc.) are found in their most stable 2H crystalline form (Figure 4-1a) and display direction independent (isotropic) properties, there exists other 2D semiconducting TMDCs such as ReS_2 and $ReSe_2$ that crystallize in 1T' phase (Figure 4-1b) with largely direction dependent (anisotropic) properties[93]. The fact that an extra valance electron in Re atoms (in comparison to group-VI Mo and W atoms) is shared between two neighboring Re atoms results in the formation of pseudo-1D Re-chains extending along [010] and subsequent attractive direction dependent (pseudo-1D) properties[47].

The true potential of these unique classes of materials can be realized especially when a variety of different types of 2D materials are stacked in lateral or vertical structures to form complex heterostructures and superlattices[13,14,97]. As such, to date, a few number of studies have demonstrated feasible synthesis routes for creating lateral and vertical heterojunctions between isotropic 2D materials, such as MoS_2/WS_2, WS_2/WSe_2, and others mainly involving group-VI TMDCs[28-31,98,99]. While 2D junctions between isotropic and anisotropic (pseudo-1D) systems offer novel opportunities and research directions, including polarization and direction dependent properties that are not possible to attain in 2D isotropic heterojunctions, their synthesis still remains at seminal stage due to complicated growth dynamics induced by highly anisotropic and complex interfacial energy. For example, previously report on ReS_2/WS_2 junction growth has been limited only to vertical heterostructure, leaving lateral junction unexplored probably due to complicated growth dynamics induced by highly anisotropic and complex interfacial energy[100]. More importantly, the anisotropic properties, which is the most attractive trait of ReS_2, in these vertical junctions are not discussed.

Here, we report on synthesis and growth dynamics of high anisotropic ReS_2/WS_2 pseudo-1D/2D material lateral heterojunctions via two-step chemical vapor deposition (CVD) for the first time. Proposed materials are carefully selected based on relatively low synthesis temperature of ReS_2 (T_g^{ReS2}~490 ^oC), which is much lower than the thermal decomposition temperature of WS_2 (~600 ^oC). Through HRSTEM, angle-resolved Raman spectroscopy, electron energy loss spectroscopy (EELS), optical absorption spectroscopy and atomic force microscopy (AFM) measurements, we were able to identify and answer three fundamental questions on the first pseudo-1D 2D material

junctions; (1) What is the overall growth dynamics of vastly different material systems? Through careful HRSTEM measurements, we managed to provide the very first atomic look at pseudo-1D / 2D material interfaces to understand the growth mechanism; (2) How do these vastly different materials stitch laterally and stack vertically? Our HRSTEM measurements show that quasi-1D Re chains orient themselves on WS_2 in [100]/[110] zigzag direction, and in the lateral junction Re-chains appear well-aligned in a direction always perpendicular to the WS_2 edges. (3) How are the anisotropic properties of 1T' phase anisotropic ReS_2 sheets influenced after they form junctions with isotropic WS_2 in 2H phase? Angle-resolved Raman measurements show that while vertical ReS_2/WS_2 sheets are highly anisotropic at nanoscales, at microscopic/macroscopic scales the anisotropy is lost due to randomization of Re-chains at the ReS_2/WS_2 interfaces.

4.2 Experimental Details

4.2.1 Materials Growth

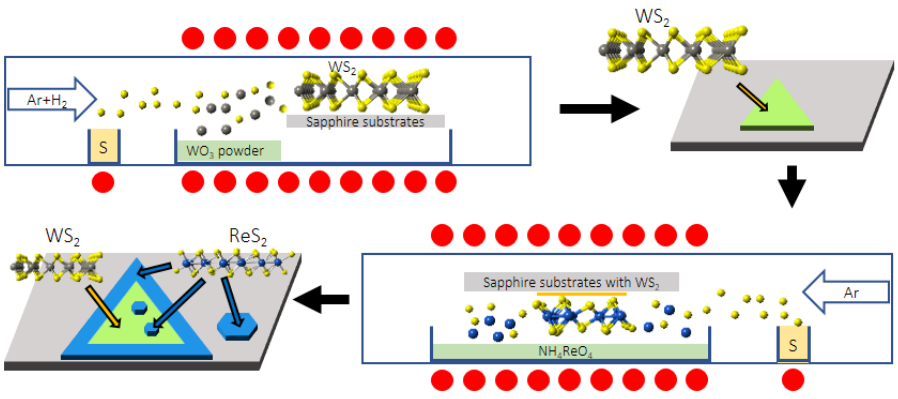


Figure 4-2 Schematic of two-step CVD growth for ReS_2/WS_2 heterostructures.

Prior to growth, sapphire substrates were treated with oxygen plasma for 3 min to remove any organic contaminants on the surface. WS_2 was first grown in a 2-inch quartz tube with WO_3 (Sigma-Aldrich 95410, powder, puriss., 99.9%) and Sulfur at 925°C. WO_3

powder was placed on a ceramic boat on the upstream side near the substrate. Sulfur (Sigma-Aldrich 414980, powder, 99.98% trace metals basis) was heated separately at around 20 cm from furnace center. Ar was used as carrier gas while H_2 as reducing agent for WO_3. The flow rate of Ar:H_2 was 80:40 sccm and the total pressure is at 1.5 Torr. In a typical process, full area coverage over 2x1 cm scale sapphire chips can be achieved within 15 minutes of growth at a slow cooling rate 5 °C min^{-1}. For heterostructure growth process, the growth time was kept at 10 minutes.

After WS_2 growth, substrates with WS_2 monolayer on top were transferred to a second furnace and placed on the top of an alumina boat containing ammonium perrhenate (Sigma-Aldrich 316954, NH_4ReO_4, 99%) precursor. This ceramic boat was placed at the center of the heating zone of the furnace, and sulfur precursor was placed approximately 18.5 cm upstream from the NH_4ReO_4 precursor. The monolayer growth was performed at atmospheric pressure (ATM), and precursors were transported to the substrate high purity argon flow. Samples were first heated to 300 ^oC (100 sccm Ar flow), and flow was gradually decreased to 50 sccm at the growth temperature (490−520 ^oC). Sulfur precursors were sublimated at 350−420 ^oC temperature range and carried to the surface by Ar flow. Growth was carried out at 490−520 ^oC for 25 min followed by controlled cooling (5 ^oC min^{-1}) to 420 ^oC and fast cooling (>10 ^oC min^{-1}) to room temperature.

4.2.2 Roman spectroscopy

Raman measurements for the as grown samples were performed in a Renishaw InVia spectroscopy system with a 100× objective lens using a laser source with 488 nm wavelength. The laser was focused onto the sample with a spot size of ~3μm^2 and the

power of 0.5 mW. Angle-dependent data was collected by mounting samples on a rotatory stage and Raman was taken every 15 degrees of rotation

4.2.3 STEM and EELS Measurements

ReS_2/WS_2 samples are transferred from sapphire substrates to the gold grid with holey carbon film support by the PMMA-assisted process. The CVD-grown samples were coated with PMMA and subsequently, PMMA/heterojunction film was separated from the sapphire substrate by KOH etching (2 mol $^{-1}$) at 80 °C. The film was transferred to deionized water beakers to dilute KOH residue under MoS2. Finally, the PMMA was washed away by acetone solution and the sample was cleaned by IPA.

High resolution imaging and Valence electron energy loss spectroscopy were performed using Nion UltraSTEM MC High-Resolution Monochromated EELS STEM (HERMES) system equipped with a Nion high energy resolution monochromator and a modified Gatan Enfinium EEL spectrometer. The energy resolution measured from the half width of the zero-loss peak was set to be 60 meV. To improve S/N, zero loss peak (ZLP) was cut off from 0.5 eV. The accelerating voltage was 40 or 60kV, the probe size was about 0.31 nm, and the probe current was approximately 12 pA. HAADF images were taken with 30 mrad convergence angle and 80-200 mrad collection angle. Images and FFT are processed by DigitalMicrograph 3 software. Image simulation was done in Dr. Probe software. Convergence angle was set to 30 mrad and collection angle between 80 and 200 mrad.

4.3 Results

4.3.1 Growth Characteristics

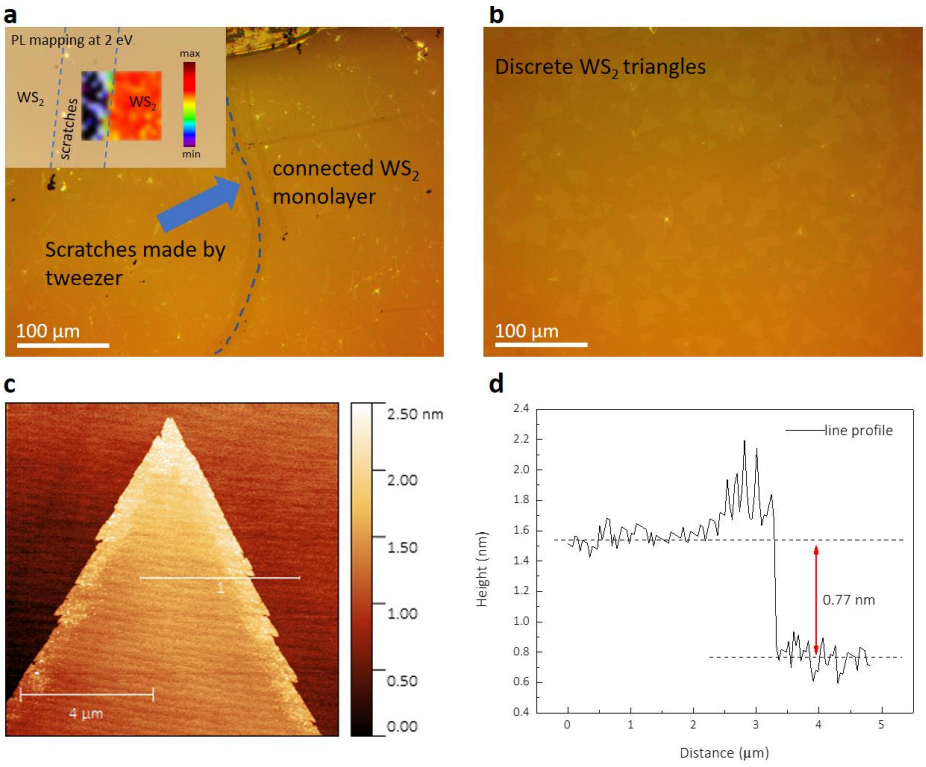


Figure 4-3 **a.** Optical image of continuous area of CVD WS_2 monolayer with manual scratch, inset is WS_2 PL mapping at scratched / unscratched region. **b.** Optical image of discrete WS_2 triangles domains. **c.** AFM measurement of triangular WS_2 and **d.** corresponding line scan profile showing monolayer thickness.

The size of WS_2 monolayer by CVD is modulated by the growth time. Longer time yields larger area of crystals that eventually merge into continuous film as shown in Figure 4-3a. Shorter time leads to discrete WS_2 monolayer that is suitable for the second step of lateral heterostructure fabrication.

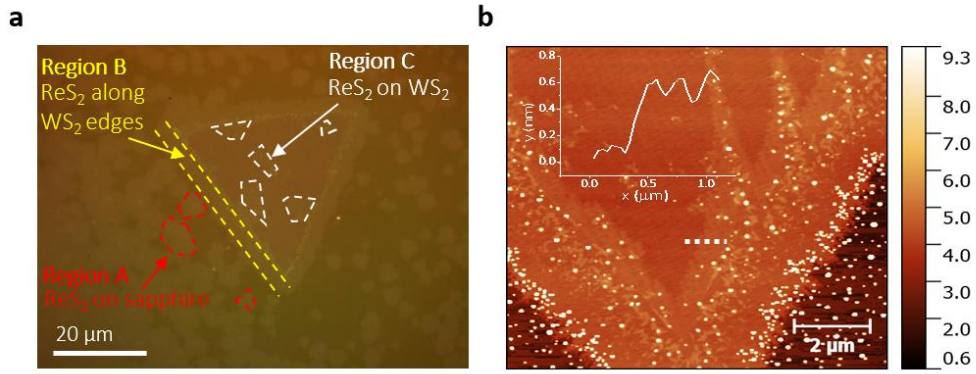


Figure 4-4 **a.** Optical image of the grown ReS_2/WS_2 heterostructure. **b.** AFM image of as-grown heterostructure edge. Inset is the line profile along white dash line.

Three different kinds of ReS_2 growth characteristics appear on sapphire; The first one (region A labelled in red dash lines in Figure 4-4a) involves direct deposition of ReS_2 monolayers directly onto sapphire substrates without making any vertical and lateral junctions with WS_2 monolayers. This can be attributed to low nucleation formation energy at highly crystalline oxide surfaces as the CVD process relies on physi-sorption of various Re-based sub-oxides complexes to carry out ReS_2 growth[66]. The second type (region B) of ReS_2 growth is mostly localized around WS_2 monolayer edges as highlighted in Figure 4-4a between yellow dash lines and constitute mostly lateral heterojunctions. Indeed, lateral junction of two dissimilar 2D layers is anticipated especially when the nucleation energy and forming energy is much reduced at the terraces and edges[101]. In this sense, WS_2 edges provide natural nucleation sites for ReS_2 and subsequent ReS_2 sheets grow laterally in layer-by-layer (LBL) mode. These clear boundaries can already be seen along those edges from optical images (Figure 4-4a). A closer look at AFM measurements at ReS_2/WS_2 interface shows that ReS_2 multiple nucleations at the WS_2 edges as evidenced by the slightly thicker formation that varies

from 2 to 5 nm in height. At this point, ReS_2 sheets grow laterally outwards (away) from monolayer (ML) WS_2 forming lateral junctions (yellow dash lined in Figure 4-4a). The third kind (region C) of ReS_2 growth takes places by nucleation on WS_2 surface followed by a lateral diffusion process (white dash lines in Figure 4-3a) and formation of vertical heterojunctions. Since chemically passive 2D surfaces have higher nucleation barrier compared to chemically active edge-sites, their nucleation density is low and grow only at localized regions while lateral junctions conform around the entire WS_2 edges. The height of as grown WS_2 is measured by AFM to be 0.8 nm, which is in line with previous reports[102-104]. The step height of ReS_2 measured from WS_2 at this area is found to be ~0.5nm, which is approximately the thickness of a single layer ReS_2[49,65,66,105] (inset of Figure 4-4b).

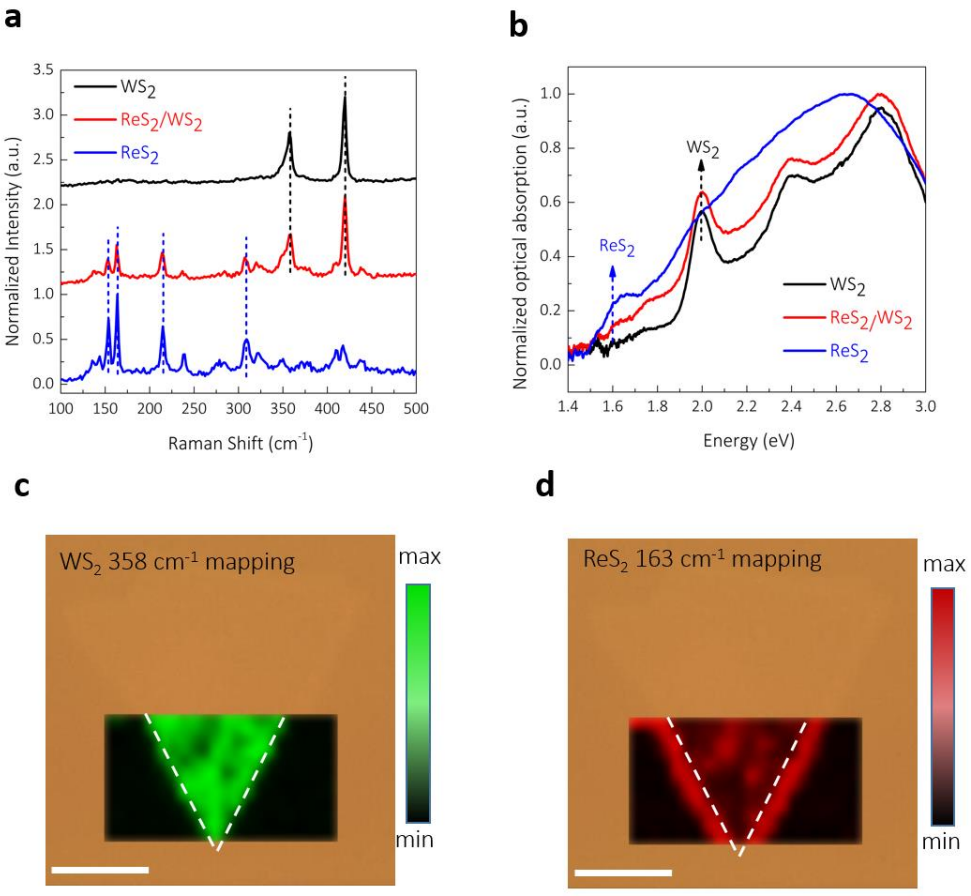


Figure 4-5 **a.** Raman spectra and **b.** micro-absorption spectra of ReS_2, WS_2, and ReS_2 /WS_2 regions. **c.** Raman mappings of WS_2 358 cm^{-1} peak and **d.** ReS_2 163 cm^{-1} peak, respectively. Scale bar is 10 μm.

Raman spectroscopy was utilized as a convenient method for identifying these two materials since ReS_2 has strong Raman peaks at 139, 151, 161, and 214 cm^{-1}[149] that are clearly different from two intense in-plane 359 cm^{-1} (A_{1g}) and out of plane 419 cm^{-1} (E_{2g}) modes of WS_2[49,102]. Figure 4-5a shows Raman spectra of ReS_2, ReS_2/WS_2, and WS_2 areas with 488 nm laser as excitation source. ReS_2/WS_2 spectrum (red solid line) was collected on spots where ReS_2 and WS_2 sheets clearly overlap each other and contain Raman peaks from both ReS_2 and WS_2 monolayers. These three distinct regions are also confirmed by micro-absorption spectroscopy in Figure 4-5b: Blue solid line for ReS_2 clearly marks an absorption edge at 1.60 eV which is consistent with prior results[48]. while WS_2 monolayers yield sharp peaks at 2.01 eV and 2.40 eV associated with A and B excitons[106]. Similar data and analysis on ReS_2/WS_2 vertical junctions show that ReS_2 absorption edge and excitonic peaks of WS_2 convincingly overlap, which is in accord with our HRSTEM studies in Figure 4-6.

Indeed, Raman mapping results clearly show the geometry of ReS_2/WS_2 heterogeneous region. Prominent and distinct WS_2 and ReS_2 Raman peaks at 358 cm^{-1} and 163 cm^{-1} are mapped in green (Figure 4-5c) and red (Figure 4-5d). Here, the inner WS_2 triangle (guided by white dash lines) is surrounded by ReS_2 grown from WS_2 edge front and some of the ReS_2 layers are found randomly distributed across the WS_2 surface (see red regions scattered across the WS_2 triangle in Figure 4-5d).

4.3.2 Microscale Look and EELS Measurements

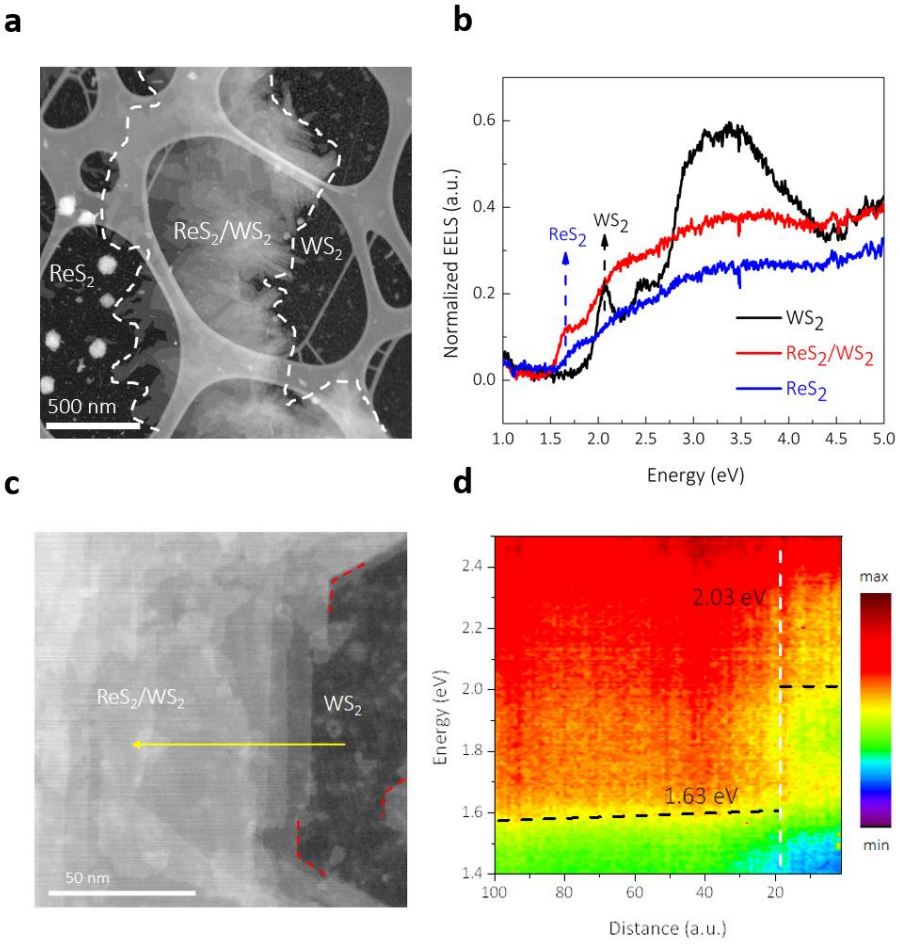


Figure 4-6 **a.** Low magnification STEM image of heterostructure edge, where ReS_2 and WS_2 overlap. **b.** Point EELS measurements performed at ReS_2, WS_2, and ReS_2/WS_2 areas. **c.** STEM image at ReS_2/WS_2 interface and **d.** corresponding EELS line scan across it along the yellow arrow. A transition from WS_2 bandgap absorption at 2.03 eV to ReS_2 at 1.63 eV is shown.

To better understand the interface across ReS_2 and WS_2 layers at a microscopic scale, we have performed careful STEM measurements. In Figure 4-6a, we present a low magnification STEM image taken at the ReS_2/WS_2 lateral interface. Dendritically grown ReS_2 clusters (nucleates) are found to be are narrowly localized where ReS_2 and WS_2 makes a lateral junction. This is likely due to high density nucleation centers at defect

rich 1D grain boundaries between WS_2 and ReS_2 sheets and the reduced nucleation energy battier at the step edge sites of WS_2, which prevents further atomic resolution imaging at the junction interface. It is noted that such interface is in contrast to conventional isotropic lateral junction, where clean interfaces are resolved as a result of similar growth temperature of sequential vapor depositions and continuous supply of different precursors from single step growth[28,73]. Nanoscale resolution electron energy loss spectroscopy (nano-EELS) measured at different parts across the junction region shows sharp excitonic peaks for WS_2 and clear band edges for ReS_2 (Figure 4-6b). Previously, EELS has been demonstrated as an effective method to identify fundamental band gap, absorption edges, excitonic, and defect (localized) energy bands in 2D TMDC material systems[107]. These EELS results are consistent with micro-absorption spectra in Figure 4-5b. Moreover, an EELS line scan across WS_2 layer to ReS_2 wall region suggests the excitonic transition from WS_2 layer to ReS_2/WS_2 heterostructure (Figure 4-6d).

4.3.3 Atomic Scale Structural Studies

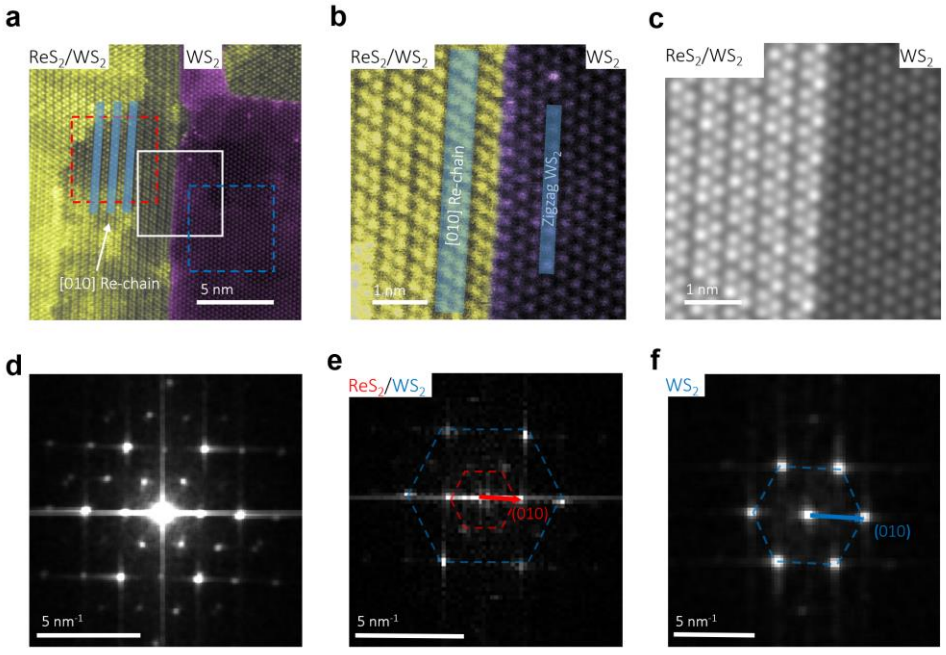


Figure 4-7 **a.** HAADF STEM image taken at the ReS_2/WS_2 interface, and **d.** corresponding FFT image **b.** Zoom-in image of the area outlined by the solid white square in a and **c.** simulated STEM image by Dr. Probe software. **e.** FFT of ReS_2/WS_2 area squared by solid white line and **f.** FFT of pure WS_2 layer squared by dash blue line in a.

To obtain detailed structural information of vertical ReS_2/WS_2 heterostructures, we performed high-resolution STEM studies. Surprisingly, ReS_2 monolayers stack on WS_2 sheets in 1T' anisotropic phase with clearly aligned Re-chains (outlined by blue strips) as clearly seen in high resolution images highlighted by red dashed square in Figure 4-7a. Here, it is noteworthy to mention that 1T' phase is energetically more favorable against 2H ReS_2 due to the presence of an extra electron in group-VII Re atoms compared to group-VI W atoms. This suggests that even though underlying WS_2 layer is stabilized in isotropic 2H phase and layers exchange a significant amount of charge[108], ReS_2 grown onto WS_2 sheets still crystallizes in 1T' anisotropic phase with clear Re-chain direction and charge transfer across the layers is not sufficient to stabilize 2H ReS_2 phase.

A closer look at the vertical heterojunction area in Figure 4-7b reveals that Re-chains in ReS_2 align along the zigzag direction of underlying WS_2 which means that Re-chain [010] direction of ReS_2 prefers to align along [100]/[110] direction of WS_2 sheets. The high-resolution image matches well with simulated image by Dr. Probe software[109] in Figure 4-7c. Here, we note that well-defined alignment between WS_2 and ReS_2 sheets have important implications for ReS_2/WS_2 vertical and lateral heterojunctions and is discussed in greater detail in the next section.

FFT of Figure 4-7a explicitly shows two perfectly aligned hexagonal-shaped patterns (Figure 4-7d). Although ReS_2 has a triclinic crystal structure, its lattice constant and angle (a=6.419 Å, b=6.523 Å, and γ=61.163°) is rather close to hexagonal one. Thus, its

pattern deviates only slightly from a standard hexagon and we refer to the FFT pattern of ReS_2 as a quasi-hexagon for convenience. FFT image was taken on ReS_2/WS_2 vertical stacking (Figure 4-7e) area suggests that the distance between the origin and the inner hexagonal spot (red hexagon) is 1.78 nm^{-1}, corresponding to 0.562 nm in real space, which is the d-spacing of (010) plane for ReS_2. The distance between the origin and the blue hexagon spot in FFT image of ReS_2/WS_2 vertical stacking (Figure 4-7e) area and that of the pure WS_2 region (Figure 4-7f) are equal at 3.69 nm^{-1}, whose inverse value is the d-spacing of (200) plane for ReS_2, or (010) plane for WS_2. These imply that the smaller hexagonal pattern in Figure 4-7e is a quasi-hexagon attributed to ReS_2. For the larger hexagon pattern, it, in fact, consists of information from both WS_2 and ReS_2 crystal altogether. Thus, the good alignment of two patterns in FFT clearly illustrates the strict growth stacking of ReS_2/WS_2 vertical junctions, as shown in HRSTEM Figure 4-7e. We note that of all HRSTEM images taken on vertical heterostructures, this is always the case, i.e. *b*-axis [010] of ReS_2 aligns with [100] / [110] zigzag direction of underlying WS_2.

4.3.4 Highly Anisotropic Response of Pseudo-1D ReS_2 in Lateral Junction

To investigate the how anisotropy (i.e., how well Re-chains remain aligned at a given lattice direction) of ReS_2 is influenced by the overall growth dynamics, we have measured angle-resolved Raman for two ReS_2 configurations mentioned above. In a typical measurement, laser spot was kept at ~3μm^2 and the polarization direction of the exciting light source was swept from 0 to 360 degree at 15 degrees per step. Based on previous investigations on exfoliated and CVD ReS_2, polar plots of 214 cm^{-1} peak appears highly ellipsoidal in such a way that its intensity is maximized when polarization

is parallel to the Re-chain direction, giving quick and non-destructive ways to identify anisotropy direction[49,66,110].

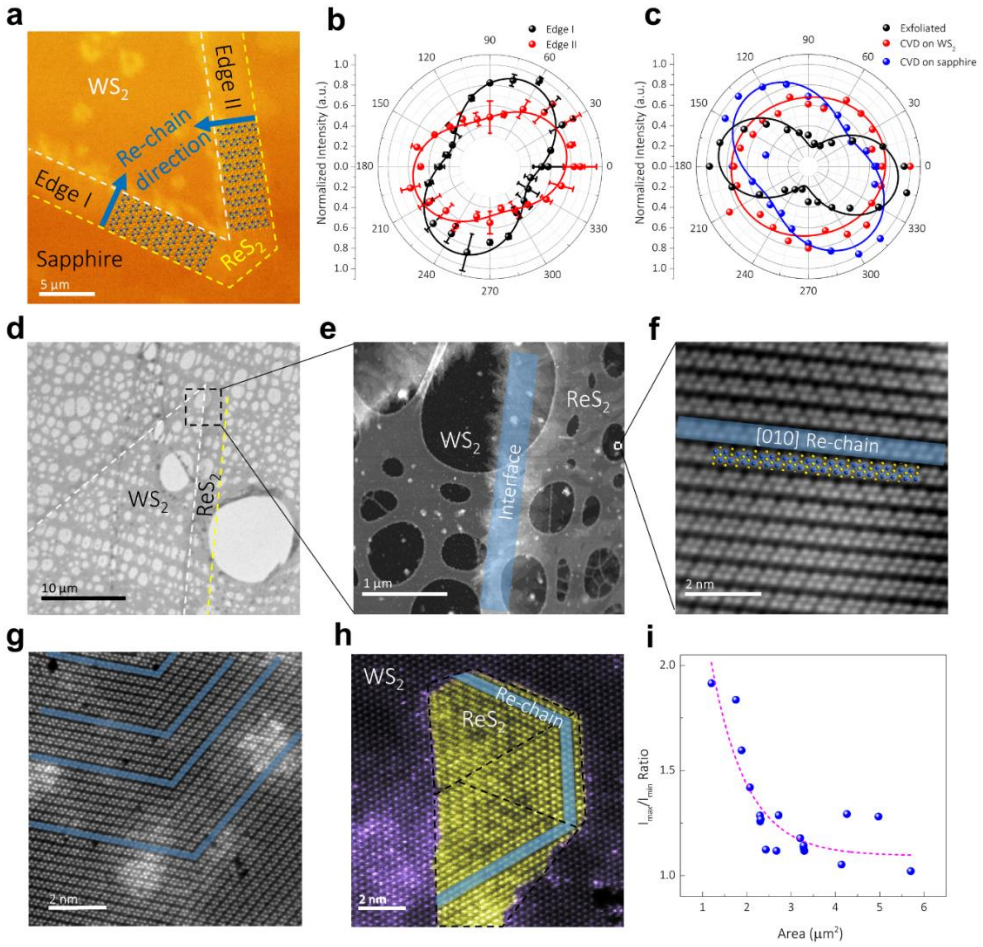


Figure 4-8 **a.** Optical image of ReS_2 layer grown along WS_2 edges extending towards sapphire substrates. **b.** Angle-resolved 214 cm^{-1} Raman peak of ReS_2 grown along the WS_2 edge I and II. **c.** Angle-resolved 214 cm^{-1} Raman of exfoliated ReS_2 and the ones grown on sapphire substrate and WS_2 sheets. **d.** Low-mag image of WS_2 monolayer triangle with lateral ReS_2 junction along edges. **e.** Zoom in HAADF STEM image of at the area squared by the black dash line in d. **f.** HAADF HRSTEM image of the white square area in e. **g.** HAADF HRSTEM image of larger scanning size at monolayer ReS_2 area. **h.** HAADF HRSTEM images of ReS_2 island on WS_2 surface and **i.** Maximum to a minimum intensity ratio of angle-resolved 214 cm^{-1} Raman peak of ReS_2/WS_2 vertical heterostructures with different ReS_2 sizes.

Figure 4-8a is a representative optical image showing the top down view of ReS_2 lateral junction grown along two adjacent WS_2 edges (labeled as edge I and edge II) which extend into the sapphire substrate with a width of around 5 μm. Angle-resolved Raman measurements on these two ReS_2 edge regions reveal much-desired anisotropic response as shown in Figure 4-8b. Surprisingly, the direction of the polar plot, i.e., b-axis Re-chain direction, always points perpendicular to WS_2 edges, as confirmed by a series of STEM images taken on lateral heterojunction area (Figure 4-8d-f). At some monolayer ReS_2 areas, rotations of Re-chain directions (Figure 4-8g) are observed probably due to electron beam irradiation and strain[105]. We note that atomic resolution STEM images only reflect crystal structures at the nanoscale, while angle resolved Raman measurements probe overall anisotropic effects at micro-size scale. This finding marks the very first observation where Re-chain direction can statistically be locked to grow in one crystalline direction. This is particularly exciting since control over anisotropy direction has been a major obstacle in pseudo-1D anisotropic material systems, and this finding sheds light on ways to achieve locked-in growth.

4.3.5 Size Dependent Anisotropy in Vertical Heterostructures

However, similar measurements on ReS_2/WS_2 vertical junctions (region C) appear rather isotropic (Figure 4-8c). This implies that the anisotropy is lost at laser probing scales (~3μm^2), which is in stark contrast to exfoliated sample and laterally grown ReS_2. To understand the origin of loss of anisotropy on ReS_2/WS_2 vertical junctions, we take a closer look at some representative high-resolution STEM images. It is found that for isolated monolayer ReS_2 islands on the WS_2 surface (Figure 4-8h), it contains several sub-domains (guided by black dash lines). Re-chains in these sub-domains are oriented in

different lattice directions (guided by blue lines) in comparison to neighboring sub-domains. Thus, at length scales comparable to laser excitation spot, anisotropic Raman signal is cancelled out by nearby sub-domains resulting in nearly zero anisotropy at micron scales[66]. This can be clearly seen in Figure 4-8i where the degree of anisotropy (defined as the ratio of maximum to minimum intensity in its polar Raman plot I_{max}/I_{min}) is plotted against the area of ReS_2 domains on WS_2 monolayers (vertical heterojunction).

One important observation is that Re-chains of ReS_2 are not randomly oriented[66,105], but instead, they orient themselves in multiples of 60 degrees (Figure 4-8h) which stems from the fact that Re-chains are aligned along WS_2 zigzag direction (Figure 4-7b) and unintentionally assume 3-fold symmetry of underlying WS_2. Thus, Re-chains are either anticipated to change their directions at multiples of 60 degrees each time Re-chain interacts with a defect site to lower total energy by remaining aligned along the zigzag direction of ML WS_2 (In a perfect crystal, however, Re-chains may extend infinitely along WS_2 chain direction). This suggests that underlying 3-fold symmetric 2H phase WS_2 monolayers dictate the ReS_2 growth dynamics even when ReS_2 monolayers are weakly coupled to WS_2 sheets by van der Waals epitaxy.

While large areas of vertical heterojunctions can be achieved between similar 2D materials (MoS_2/WS_2), ReS_2 sheets reach only few-microns in size and develop sub-domains with limited anisotropic responses. Within TLK (terrace-ledge-kink) model of layer-by-layer growth mode, this can be attributed to the surface reaction limited process and surface diffusion of reactive spices is slow for crystal growth[111] due to relatively low ReS_2 CVD process temperature (500 ^oC). The surface mobility is further limited potentially by the presence of defects which are injected into ML WS_2 during ReS_2

growth as the temperature required to create point defects (sulfur vacancy V_S) in ML WS_2 is close to ReS_2 growth temperature[112]. These defects can be identified in ML WS_2 Figure 4-7 and Figure 4-8. While vacancy sites promote the nucleation by offering chemically active sites on WS_2 monolayers, they adversely affect ReS_2 growth by a change in lattice direction at defect cite as observed in two recent work[66,105] resulting in loss of anisotropy. Since the sapphire is more thermal resistant, ReS_2 can grow more "freely" directly on sapphire substrate and therefore shows larger area growth and consistently higher degree of anisotropy.

4.4 Discussions

We developed a two-step CVD growth technique for the synthesis of highly anisotropic pseudo-1D/2D material lateral heterostructures for the first time. Results show that growth characteristics of these novel heterojunctions by structurally dissimilar materials differ significantly from heterostructures of isotropic 2D materials such as MoS_2/WS_2, largely due to the anisotropic interfacial energy of ReS_2. HRSTEM reveals that Re-chains (anisotropy) in vertical heterostructures orient themselves preferentially along WS_2 zigzag direction which has three important consequences for the heterostructure synthesis: 1) The direction of the Re-chains change (possibly due to presence of defects)[66,105] at multiples of 60 degrees in attempt to keep themselves closely aligned along WS_2 zigzag direction, 2) 60 degree Re-chain rotations impact micro- and macroscale anisotropic properties by reducing the anisotropy of vertical ReS_2/WS_2 junctions, and 3) Large scale synthesis of ReS_2/WS_2 heterostructures is limited as no clear ReS_2 growth direction can be assigned on WS_2 surface due to randomization of Re-chain directions. Most surprisingly when ML ReS_2 stitches to WS_2 and form lateral

junctions, Re-chain direction prefers to run perpendicular to WS_2 edges. Consequently, lateral grown ReS_2 sheets display remarkable macroscopic crystalline anisotropy. This means that strong crystalline anisotropy can be achieved when Re-chain direction is locked at a given lattice direction (For example, when Re-chain is vertical to WS_2 edges), and offers routes to both achieve and control anisotropy direction of pseudo-1D systems for the first time. Overall findings advance the fundamental understanding of the synthesis of dissimilar (anisotropic/isotropic) 2D materials with vastly different crystal structures and provide deeper insight into the fabrication of these novel 2D heterostructures, which are anticipated to be an integral part of 2D materials applications in optoelectronic and photonics.

Chapter 5 Tellurium/2D Layer Heterostructures

This chapter is mostly adapted from our submitted manuscript: Yang, S., Chen, B., Qin, Y., Zhou, Y., Liu, Lei., Durso, M., Zhuang, H., Shen, Y., Tongay, S. (2018). Highly Crystalline Synthesis of Tellurene Sheets on 2D Surfaces: Control over helical chain direction of tellurene.

5.1 Introduction

Recently, two-dimensional (2D) elemental tellurium attracted much interest owing to its superior electronic[113-116] and thermoelectric[117-119] properties all stemming from its unique pseudo-1D (anisotropic) crystalline structure. Helically arranged tellurium atoms form tellurium chains extending along the [001] lattice direction, and these individual chains couple relatively weakly to each other to form 2D-like tellurium sheets in 2D landscape[120]. Unlike other pseudo-1D materials, such as GaTe, WTe_2, ReS_2, and ZrS_3, tellurium sheets cannot be easily exfoliated from bulk to monolayers –presumably due to stronger interlayer coupling energy– thus bottom-up synthesis routes are needed to yield them in ultra-thin form. Before the (re)emergence of tellurium with a fresh approach and interpretation from 2D community, elemental tellurium thin films have been readily synthesized by a variety of techniques in the last fifty (50) years. These techniques include hydrothermal synthesis[35,121,122], physical vapor deposition (PVD)[123-125], molecular beam epitaxy (MBE)[126,127], and countless others[42]. However, these growth techniques produced amorphous or polycrystalline tellurium sheets that measured 100 nm – 10 μm in thickness without any concern over crystalline phase or thickness.

Most recently, it has been shown to assume 2D sheet-like form when grown by hydrothermal synthesis technique[35]. This innovative work demonstrated the efficacy of

the approach towards high-carrier mobility transistors solely based on these tellurium sheets. While hydrothermal synthesis is suitable to yielding potentially crystalline materials, it is well-known for its incompatibility with the manufacturing and scaling. It typically produces powder-like materials that require their further processing to be deposited onto desired substrates. As such, there is an urgent need for conventional and scalable synthesis methods for vdW tellurium sheets with desired crystallinity and controlled crystalline anisotropy. Controlled anisotropy and tellurium chain direction is particularly crucial for their easy integration and applications since most desired physical properties are attained along helical tellurium chains.

The aim of this work is to synthesize tellurium sheets on a large variety of vdW surfaces that can attain high crystallinity and controlled structural anisotropy

5.2 Experimental Details

5.2.1 Synthesis of Tellurium

Substrates were cleaned in a Tergeo plasma cleaner prior to use. 2D materials were exfoliated onto cleaned substrates with standard tape exfoliation. 10 mg Te powder (Sigma Aldrich, 99.997%, 30 mesh) was placed in a quartz boat at the center of a 1-inch tube furnace as Te source, and target substrates were placed 14~16 cm from the Te source on the downstream side. The pressure of the system was maintained at 8 Torr with 10 sccm Ar as carrier gas. Temperature of Te source was then ramped to 440 ^{o}C at 30 ^{o}C/min and then maintained at 440 ^{o}C for 15 min. Then the furnace was opened and cooled naturally to room temperature before removing the samples.

5.2.2 Raman Spectroscopy

Raman spectra were recorded on a home-made Raman spectrometer with a 532 nm excitation laser in the backscattering configuration with 2400/mm grating. The spot size of focused laser was ~1 μm and laser power was 230 μW. Angle resolved Raman spectra were recorded on the same system by rotating a half-wave plate that changes the polarization plane of laser while the sample is fixed. Raman maps were recorded on Renishaw in via Raman microscope with a 488 nm excitation laser in the backscattering configuration with 2400/mm grating. Step size is set to 0.5 μm. All measurements were performed under ambient conditions at room temperature.

5.2.3 Microscopy Characterization

FEI Titan 80-300 is used for the TEM negative Cs imaging, which operates at 300kV without objective aperture and the spherical aberration is set at ~ minus 15 microns. SAED patterns were collected by a 10 μm size aperture with a camera length of 380 mm. Results are processed by DigitalMicrograph 3 software. The cross-section sample was prepared by Nova 200 focused ion beam system. Prior to FIB cutting, it was deposited by a thin layer of carbon followed by an E-beam Pt layer, and followed by a layer of ion-beam deposited Pt.

5.3 Results

5.3.1 Synthesis and Growth Characteristics

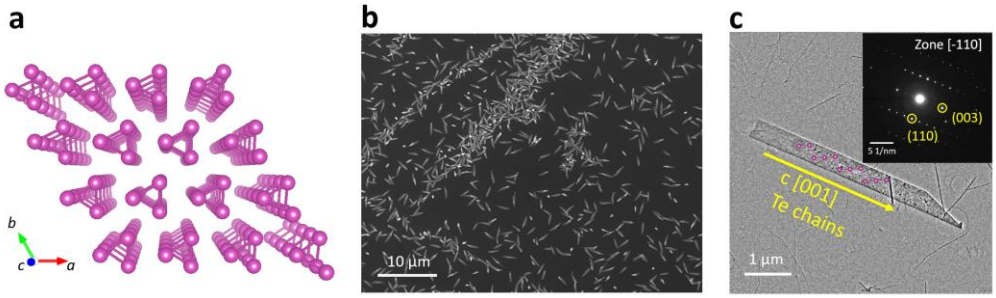


Figure 5-1 **a.** Crystal structure of Tellurium viewing down from c-axis. **b.** SEM images of randomly oriented Te grown on sapphire. **c.** Low-magnification TEM image and corresponding diffraction pattern showing the c-axis is along the longitudinal crystal grown direction.

We first discuss our results on sapphire substrates which enable the deposition of highly crystalline tellurium sheets, however, without any control over tellurium chain orientation as shown in Figure 5-1b. Low magnification TEM image clearly shows pseudo-1D nature (Figure 5-1c), and its corresponding SAED pattern ([-110] zone axis) concludes that *c*-axis is along the longitudinal direction of tellurium sheet, with lattice parameters of d(001)=0.589 nm and d(110)=0.221 nm (Figure 5-1c inset). This means when tellurium needles are on the substrate, helical tellurium chains [001] run along the geometrical anisotropy (high aspect ratio) direction and is parallel to substrate plane.

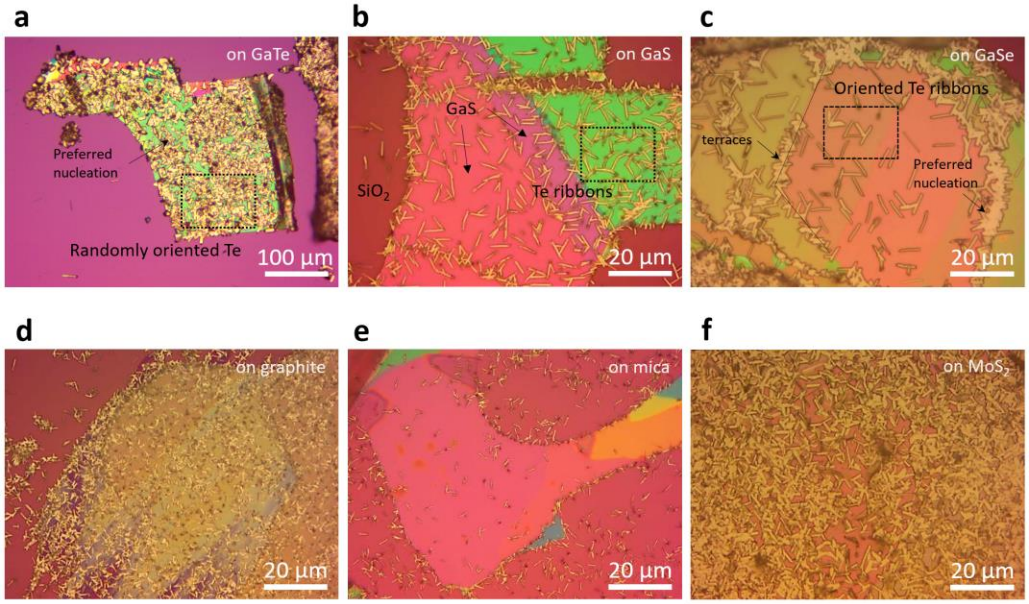


Figure 5-2 PVD results on different exfoliated 2D materials. **a.** GaS. **b.** GaSe. **c.** GaTe. **d.** mica. **e.** MoS_2. **f.** graphite.

To achieve layer-by-layer and self-oriented growth, we have performed similar growth processes onto a variety types of substrates such as GaS, GaSe, GaTe, mica, MoS_2, and graphite. Selected crystals all have thermal decomposition temperatures much higher than that of our growth temperatures (T_s=330 ^oC), and thus tellurium synthesis does not amorphized or alter 2D surface chemistry. GaS, GeSe, mica, graphite, and MoS_2 all crystallize in hexagonal phase but exhibit vastly different lattice constants. Largely different lattice constant values offer an ideal platform to investigate tellurium synthesis and help to reach the fundamental understanding of vdW or conventional epitaxy of tellurium sheets on these surfaces. Lastly, GaTe is energetically most stable in its monoclinic (anisotropic) phase and is well-known for its pseudo-1D nature[128-131] which could potentially help to orient Te chain directions owing to highly anisotropic nucleation and reaction rates stemming from its pseudo-1D crystalline nature. These vdW layers were exfoliated from chemical vapor transport grown crystals and deposited onto SiO_2/Si

substrates for easy handling. Direct synthesis on these vdW crystals produced the same results, and thus results on exfoliated sheets are well-representative of the growth dynamics.

In Figure 5-2, we show optical images on tellurium sheets synthesized on these 2D surfaces. We first notice that tellurium nucleation and growth is far more preferential on 2D surfaces (mica being the only exception) -especially near atomically sharp terraces- due to much smaller nucleation barrier or faster diffusion speed compared to amorphous SiO_2. While tellurium sheets adhere well to these 2D surfaces (layer-by-layer growth), they are randomly oriented on GaTe, mica, graphite, and MoS_2 without any registry or substrate induced effects. In contrast, Te synthesized on GaSe and GaS produce highly crystalline and oriented pseudo-1D tellurium chains. Pseudo-1D chains extend along three major lattice directions (3-fold symmetry), in particular along arm-chair direction of GaSe as experimentally and theoretically demonstrated later in the article. Te chains prefer to align themselves energetically either parallel or make $\pi/3$ angle to the terraces as shown in Figure 5-2b. On SiO_2/Si substrate, slightly away from GaSe sheets, tellurium immediately becomes randomly oriented further demonstrating the importance of the surface structure and chemistry. While Te on GaS exhibits certain growth characteristics, self-orientation (lock in growth) is not as prominent as in GaSe for the reasons that will be discussed later in the article.

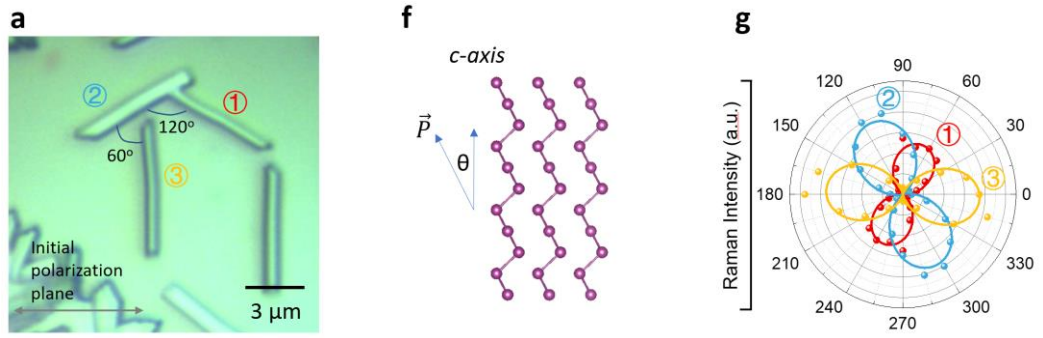


Figure 5-3 **a.** Optical image of Te on GaSe for angle resolved Raman measurements. **b.** Schematic of angle resolved Raman measurement. **c.** Polar plot of 92 cm-1 peak collected from Te ribbons.

Angle resolved Raman measurements on tellurium sheets in Figure 5-3 show that three (3) tellurium ribbons labelled as 1, 2 and 3 make 60^0 degrees with each other, and the tellurium sheets indeed align along the geometrical anisotropy axis as seen in Figure 5-3c.

5.3.2 Cross-sectional TEM and Tellurium Orientation

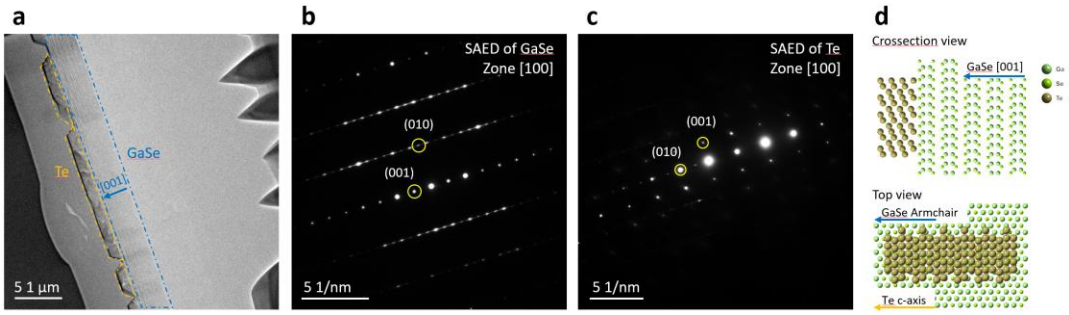


Figure 5-4 Cross-section TEM images collected from tellurium/GaSe 2D interfaces. **a.** Low magnification cross-sectional TEM image of Te/GaSe heterostack. **b.** SAED pattern of GaSe showing its zone axis is [100], which is fixed as a reference during the experiment. **c.** SAED pattern of Te crystal showing [100] zone axis. **d.** Structural models illustrating cross-sectional and top view of the heterostructure.

Considering self-oriented layer-by-layer synthesis of tellurium sheets on GaSe surfaces, two emerging questions arise: 1) What is the orientation of tellurium sheets on GaSe surfaces and 2) what is the reason behind self-oriented growth on GaSe but not other 2D surfaces? To answer the first question, we have performed cross-section TEM studies tellurium/GaSe heterostacks as shown in Figure 5-4a. It shows the cross-sectional view of the Te/GaSe structure, where the thickness of tellurium and GaSe are 0.23 μm and 0.64 μm, respectively. It is worth noting that the GaSe is a single crystal flake while there are several tellurium crystals on top separated by trapezoidal spaces in between (outlined by red dot), corresponding to cross-sectional cuts of Te crystals domains oriented differently. To determine the crystal alignment of the heterostructure, we first tilted the specimen and found the normal axis of GaSe flake to the cut plane, which is [100], as shown in Figure 5-4b. Then electron beam was moved to tellurium flakes to obtain their SAED patterns (Figure 5-4c). Since the zone axis of GaSe is kept fixed, the zone axis found in this case for tellurium must be parallel to [100] direction of GaSe. Thus, it can be deduced from these carefully collected SAED patterns that 1) the [100] directions of both GaSe and Te crystals are aligned; 2) the normal of (010) plane of GaSe coincides that of (001) plane of Te; 3) plane (001) normal of GaSe is aligned with (010) normal of Te. Strong crystal alignment information suggests robust registration between top Te and bottom GaSe layer.

To help visualizing the structure, a heterostructure model was built based on the diffraction analysis shown in Figure 5-4d. The top view clearly unveils the fact that the c-axis of Te is along the armchair direction of the underlying GaSe. This can be intuitively expected from the Figure 5-4b and c if the crystal structure is considered: the plane (010)

normal of GaSe is its [010] direction (armchair) and the plane (001) normal of Te aligns with its [001] direction (c-axis). Similar experiments and analysis performed on other Te flakes led to the same result (Figure 5-5).

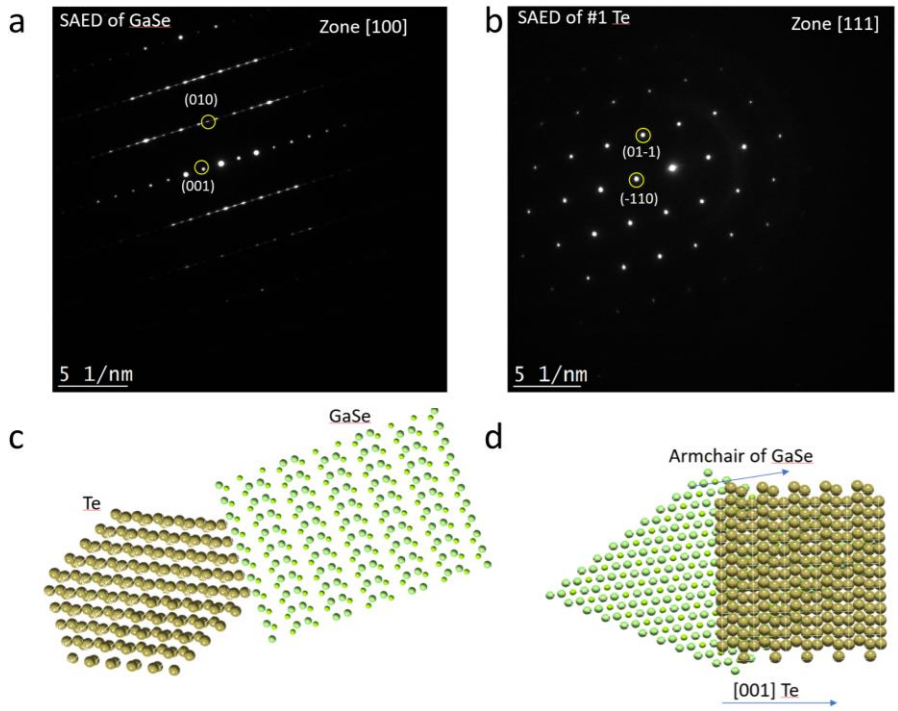


Figure 5-5 **a.** SAED pattern of GaSe showing its zone axis is [100], which is fixed as a reference during the experiment. **b.** SAED pattern of Te crystal showing [111] zone axis. **c.** Structural models illustrating cross-sectional and **d.** top view of the heterostructure showing the alignment of [001] Te chain and armchair direction in GaSe.

5.4 Discussions

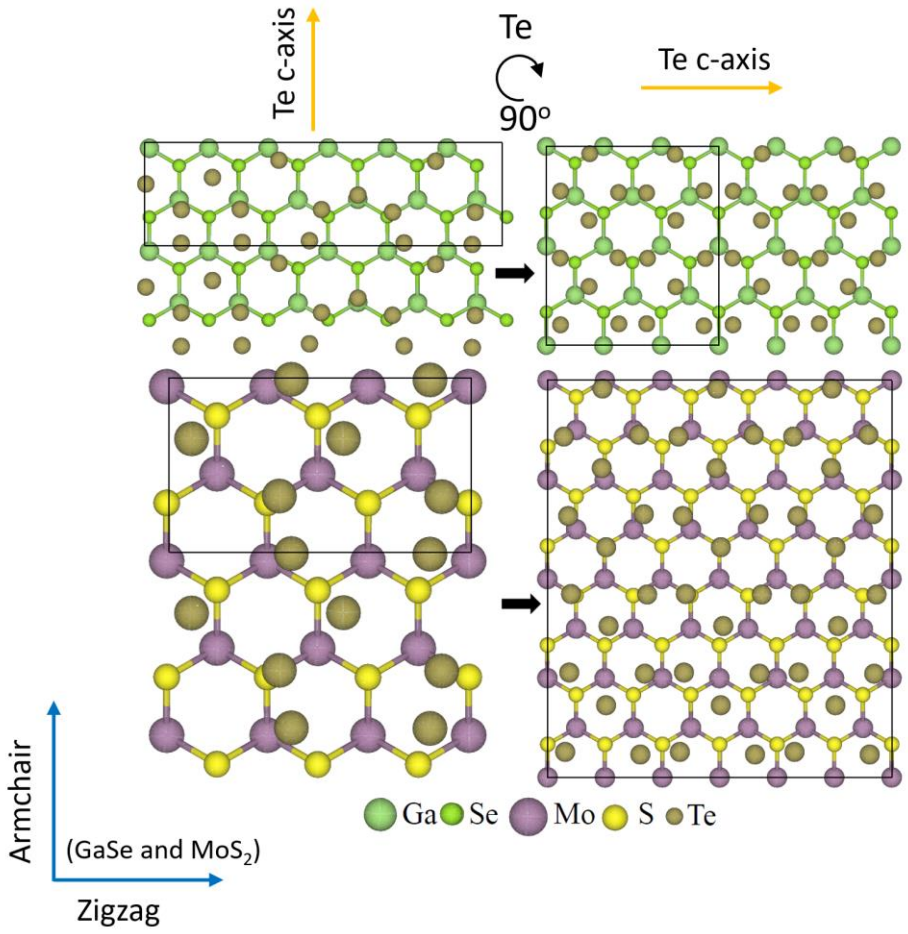


Figure 5-6 Schematic showing **a.** Te chain along armchair direction and **b.** zigzag direction of GaSe and MoS_2 substrates.

To gain a fundamental insight on the preferred tellurium orientation specifically on GaSe and GaS, we have focused on GaSe (oriented Te) and MoS_2 (random Te) surfaces and calculated the surface binding energy of these tellurium sheets when they are aligned along different crystallographic directions (Figure 5-6). The anisotropy energy is defined as the energy difference between two calculated binding energies when tellurium is aligned in different two directions. Firstly, tellurium on GaSe (tellurium/GaSe) heterostructure was relaxed to reach energetic minimal when the lattice vector $\vec{c}$ of

tellurium was aligned along the armchair edge of GaSe. This was directly compared to tellurium $\vec{c}$ vector perpendicular to armchair edge which aligns with the zigzag cut of GaSe. Here, the binding energy of tellurium/GaSe heterostructure is defined as $E_b = E_{GaSe/Te} - E_{GaSe} - E_{Te}$, where $E_{GaSe/Te}$ and E_{GaSe} are the energies of the surface slabs with and without tellurium, respectively, and E_{Te} is the energy of the surface slab of tellurium. The difference between these two tellurium orientations on GaSe can be directly correlated to tellurium ribbons' energetic ability to orient and lock-in in one particular lattice direction but not another. Theoretical results show that 1) tellurium sheets bind strongly to GaSe underlayers when tellurium chain direction is oriented along the armchair lattice cut of GaSe and 2) the difference between self-orientation along armchair and zigzag edges of GaSe is different by 46 mJ/m^2 (262 mJ/m^2 and 216 mJ/m^2 for armchair and zigzag respectively). This value for MoS_2 is only 28 mJ/m^2 (from 310 mJ/m^2 to 282 mJ/m^2 for armchair and zigzag cuts). While this difference might be partly responsible for the preferred orientation on GaSe (but not MoS_2), it is still less clear if other factors also play a role. We note that changing growth parameters for different 2D surfaces does not enable us to eventually attain oriented tellurium growth, but the observed phenomenon is only applicable to GaSe and in part to GaS. Another consideration that goes into preferred orientation of tellurium is related to lattice match across tellurium/2D interfaces. Using reported lattice parameters of GaSe and tellurium, we find that 10 unit cells of tellurium matches with 0.15% lattice mismatch to 9 unit cells of GaSe when tellurium c-axis (chain) is aligned with the armchair direction. In contrast, it takes 16 tellurium cells to fit into 25 GaSe cells when tellurium c-axis is aligned with

zigzag edges of GaSe. From thermodynamics and energetic view, the former case is much more attainable and may also help to explain the preferred orientation of tellurium.

Overall results show that preferentially oriented (lock-in) tellurium sheets can only be attained on GaSe and to a degree of GaS out of six (6) different 2D surfaces with vastly different surface chemistry and structural properties, as well as crystalline sapphire and amorphous SiO_2. From cross-sectional TEM together with theory calculations, we were able correlate how tellurium sheets align on GaSe surfaces, while angle resolved Raman, SEM, and EDS enabled us to correlate structural anisotropy to tellurium synthesis. The results herein mark the first demonstration of highly crystalline tellurium sheets with controlled anisotropy, and interpretations offer further understanding on the growth characteristics. Results lay the foundation of tellurium synthesis using conventional and manufacturing compatible growth routes, and our findings are anticipated to guide other researchers to understand the true potential of this new-class of 2D tellurium.

Chapter 6 Summary and Future Directions

6.1 Summary

In this dissertation, we have investigated the relationship between atomic structure and anisotropic responses of pseudo-1D at macroscopic level. Chapter 1 introduces the 2D and pseudo-1D materials and points out the challenges in practical application of anisotropic 2D materials. Chapter 2 reviews experimental techniques. Chapter 3 discussed vapor phase deposition of high quality ReS_2 monolayer. Chapter 4 and chapter 5 explore the possibility of controlling anisotropy directions in pseudo-1D materials by design of heteroepitaxial growth.

The main accomplishments are summarized in the following:

- Developed chemical vapor deposition technique for ReS_2 monolayer growth with retained high structural anisotropy (chapter 3).
- Developed vapor deposition technique for isotropic/pseudo-1D heterostructures (chapter 4 and chapter 5).
- Established the subdomain architectures in CVD ReS_2 monolayer samples (chapter 3).
- Revealed the possible connection between lost anisotropy at macroscopic scale and microscopic disorder by high resolution electron microscopy technique (chapter 3 and chapter 4).
- Demonstrated the controlled anisotropy in pseudo-1D materials by both lateral and vertical epitaxy (chapter 4 and chapter 5).

6.2 Future Directions

Results summarized above mark advances in understanding of novel anisotropic 2D materials and point towards future research directions at the same time.

6.2.1 Interface Structure and its Reliability

As pointed out in chapter 4, the dense nucleation and dendritic growth at the lateral junction interface between ReS_2 and WS_2 monolayer prevent further high resolution structural characterizations of the atomic bonding. The nature of locked-in growth of Re-chain direction perpendicular to WS_2 edges remains unexplored. Considering the stable configuration of zigzag terminating edge in MX_2 triangular flakes[132,133], the lattice match would predict the arm chair direction of ReS_2 runs perpendicular to WS_2 edges, in which case the anisotropic axis is parallel to WS_2 edges, similar to the 1-T' $MoTe_2/MoS_2$ lateral junction case[134]. It needs clarification that if there is highly non-equilibrium growth condition imposing a strong kinetic effect that forces ReS_2 to orient itself in the specific way, or if the edge of WS_2 is modified during growth so that it accommodates the arm chair direction of ReS_2. More importantly, defects and strain in conventional epitaxial interface have critical effects on device performance, and therefore robustness of the 2D heterojunction boundary for its applications in the presence of unintended defects and strain warrants future research.

6.2.2 Interface Diffusion

Previous studies on the isotropic lateral junction indicate the existence of bilateral diffusion in these systems[28,29,73]. Since lateral heterostructures are expected to work as p-n junctions for nanoscale electronics, it is critical to characterize the inter-diffusion to control device performance and reliability. On the other hand, considering the non-

equivalent interfacial energy along different crystal axes, how the diffusion processes differ in pseudo-1D heterojunction interface is of interest. For example, whether atoms in isotropic layers have preferential diffusion channel into ReS_2 remains further investigation.

6.2.3 Substrate Effects

The main difference between our CVD ReS_2 with strong anisotropy and subdomains and previous studies lies in substrates. Crystalline c-cut sapphire may play a key role in the growth process to help align Re-chain orientations in ReS_2. Together with complicated results of vertical epitaxy demonstrated in and chapter 5, it indicates that the choice of substrates is important for proper van der Waals epitaxial growth.

In conventional heteroepitaxy[69], lattice match is critical but in the case of vdW epitaxy, this requirement is relaxed[70,71], and the question is to what extent. Other factors needing further investigation includes: symmetry of substrate surface and electronic charges, etc.

REFERENCES

1 Novoselov, K. S. *et al.* Electric field effect in atomically thin carbon films. *Science* **306**, 666-669, doi:10.1126/science.1102896 (2004).

2 Castro Neto, A. H., Guinea, F., Peres, N. M. R., Novoselov, K. S. & Geim, A. K. The electronic properties of graphene. *Reviews of Modern Physics* **81**, 109-162, doi:10.1103/RevModPhys.81.109 (2009).

3 Panchal, V., Pearce, R., Yakimova, R., Tzalenchuk, A. & Kazakova, O. Standardization of surface potential measurements of graphene domains. *Sci Rep* **3**, 2597, doi:10.1038/srep02597 (2013).

4 Bolotin, K. I. *et al.* Ultrahigh electron mobility in suspended graphene. *Solid State Communications* **146**, 351-355, doi:10.1016/j.ssc.2008.02.024 (2008).

5 Balandin, A. A. *et al.* Superior thermal conductivity of single-layer graphene. *Nano Letters* **8**, 902-907, doi:10.1021/nl0731872 (2008).

6 Lee, C., Wei, X. D., Kysar, J. W. & Hone, J. Measurement of the elastic properties and intrinsic strength of monolayer graphene. *Science* **321**, 385-388, doi:10.1126/science.1157996 (2008).

7 Wang, Q. H., Kalantar-Zadeh, K., Kis, A., Coleman, J. N. & Strano, M. S. Electronics and optoelectronics of two-dimensional transition metal dichalcogenides. *Nat Nanotechnol* **7**, 699-712, doi:10.1038/nnano.2012.193 (2012).

8 Vogel, E. M. & Robinson, J. A. Two-dimensional layered transition-metal dichalcogenides for versatile properties and applications. *MRS Bulletin* **40**, 558-563, doi:10.1557/mrs.2015.120 (2015).

9 Scholes, G. D. & Rumbles, G. Excitons in nanoscale systems. *Nat Mater* **5**, 683-696, doi:10.1038/nmat1710 (2006).

10 Berkelbach, T. C., Hybertsen, M. S. & Reichman, D. R. Theory of neutral and charged excitons in monolayer transition metal dichalcogenides. *Physical Review B* **88**, 45318, doi:10.1103/PhysRevB.88.045318 (2013).

11 Banhart, F., Kotakoski, J. & Krasheninnikov, A. V. Structural defects in graphene. *ACS Nano* **5**, 26-41, doi:10.1021/nn102598m (2011).

12 Rasool, H. I., Ophus, C. & Zettl, A. Atomic Defects in Two Dimensional Materials. *Adv Mater* **27**, 5771-5777, doi:10.1002/adma.201500231 (2015).

13 Pant, A. *et al.* Fundamentals of lateral and vertical heterojunctions of atomically thin materials. *Nanoscale* **8**, 3870-3887, doi:10.1039/c5nr08982d (2016).

14 Duan, X., Wang, C., Pan, A., Yu, R. & Duan, X. Two-dimensional transition metal dichalcogenides as atomically thin semiconductors: opportunities and challenges. *Chem Soc Rev* **44**, 8859-8876, doi:10.1039/c5cs00507h (2015).

15 Tsai, M.-L. *et al.* Monolayer MoS2 Heterojunction Solar Cells. doi:10.1021/nn502776h (2014).

16 Britnell, L. *et al.* Strong light-matter interactions in heterostructures of atomically thin films. *Science* **340**, 1311-1314, doi:10.1126/science.1235547 (2013).

17 Britnell, L. *et al.* Field-effect tunneling transistor based on vertical graphene heterostructures. *Science* **335**, 947-950, doi:10.1126/science.1218461 (2012).

18 Wang, H. *et al.* Integrated circuits based on bilayer MoS(2) transistors. *Nano Lett* **12**, 4674-4680, doi:10.1021/nl302015v (2012).

19 Loan, P. T. *et al.* Graphene/MoS(2) heterostructures for ultrasensitive detection of DNA hybridisation. *Adv Mater* **26**, 4838-4844, doi:10.1002/adma.201401084 (2014).

20 Chang, Y. H. *et al.* Three-dimensional molybdenum sulfide sponges for electrocatalytic water splitting. *Small* **10**, 895-900, doi:10.1002/smll.201302407 (2014).

21 Smith, A. J. *et al.* Molybdenum sulfide supported on crumpled graphene balls for electrocatalytic hydrogen production. *Advanced Energy Materials* **4** (2014).

22 Shi, Y. *et al.* Self-assembly of hierarchical MoSx/CNT nanocomposites (2< x< 3): towards high performance anode materials for lithium ion batteries. *Scientific reports* **3**, 2169 (2013).

23 Cao, X. *et al.* Preparation of MoS2 - Coated Three - Dimensional Graphene Networks for High - Performance Anode Material in Lithium - Ion Batteries. *Small* **9**, 3433-3438 (2013).

24 Fang, H. *et al.* Strong interlayer coupling in van der Waals heterostructures built from single-layer chalcogenides. *Proc Natl Acad Sci U S A* **111**, 6198-6202, doi:10.1073/pnas.1405435111 (2014).

25 Pospischil, A., Furchi, M. M. & Mueller, T. Solar-energy conversion and light emission in an atomic monolayer pn diode. *Nature nanotechnology* **9**, 257-261 (2014).

26 Yamamoto, M. *et al.* Self-limiting layer-by-layer oxidation of atomically thin WSe2. *Nano Lett* **15**, 2067-2073, doi:10.1021/nl5049753 (2015).

27 Lee, C.-H. *et al.* Atomically thin p–n junctions with van der Waals heterointerfaces. *Nature nanotechnology* **9**, 676-681 (2014).

28 Gong, Y. *et al.* Vertical and in-plane heterostructures from WS2/MoS2 monolayers. *Nat Mater* **13**, 1135-1142, doi:10.1038/nmat4091 (2014).

29 Gong, Y. *et al.* Two-Step Growth of Two-Dimensional WSe2/MoSe2 Heterostructures. *Nano Lett* **15**, 6135-6141, doi:10.1021/acs.nanolett.5b02423 (2015).

30 Huang, C. *et al.* Lateral heterojunctions within monolayer MoSe2-WSe2 semiconductors. *Nat Mater* **13**, 1096-1101, doi:10.1038/nmat4064 (2014).

31 Duan, X. *et al.* Lateral epitaxial growth of two-dimensional layered semiconductor heterojunctions. *Nat Nanotechnol* **9**, 1024-1030, doi:10.1038/nnano.2014.222 (2014).

32 Tian, H. *et al.* Low-symmetry two-dimensional materials for electronic and photonic applications. *Nano Today* **11**, 763-777, doi:10.1016/j.nantod.2016.10.003 (2016).

33 Joshua, O. I. *et al.* Electronics and optoelectronics of quasi-1D layered transition metal trichalcogenides. *2D Materials* **4**, 022003 (2017).

34 Dai, J. & Zeng, X. C. Titanium trisulfide monolayer: theoretical prediction of a new direct-gap semiconductor with high and anisotropic carrier mobility. *Angew Chem Int Ed Engl* **54**, 7572-7576, doi:10.1002/anie.201502107 (2015).

35 Wang, Y. *et al.* Field-effect transistors made from solution-grown two-dimensional tellurene. *Nature Electronics* **1**, 228-236, doi:10.1038/s41928-018-0058-4 (2018).

36 Liu, F. *et al.* Highly Sensitive Detection of Polarized Light Using Anisotropic 2D ReS2. *Advanced Functional Materials* **26**, 1169-1177, doi:10.1002/adfm.201504546 (2016).

37 Gong, C. *et al.* Electronic and Optoelectronic Applications Based on 2D Novel Anisotropic Transition Metal Dichalcogenides. *Adv Sci (Weinh)* **4**, 1700231, doi:10.1002/advs.201700231 (2017).

38 Wang, Z. & Feng, P. X. L. Design of black phosphorus 2D nanomechanical resonators by exploiting the intrinsic mechanical anisotropy. *2D Materials* **2**, doi:10.1088/2053-1583/2/2/021001 (2015).

39 Xia, F., Wang, H. & Jia, Y. Rediscovering black phosphorus as an anisotropic layered material for optoelectronics and electronics. *Nature Communications,*

Published online: 21 July 2014; | doi:10.1038/ncomms5458, doi:doi:10.1038/ncomms5458 (2014).

40 Lee, S. *et al.* Anisotropic in-plane thermal conductivity of black phosphorus nanoribbons at temperatures higher than 100 K. *Nature Communications* **6**, 8573, doi:10.1038/ncomms9573 (2015).

41 Luo, Z. *et al.* Anisotropic in-plane thermal conductivity observed in few-layer black phosphorus. *Nat Commun* **6**, 8572, doi:10.1038/ncomms9572 (2015).

42 He, Z., Yang, Y., Liu, J.-W. & Yu, S.-H. Emerging tellurium nanostructures: controllable synthesis and their applications. *Chemical Society Reviews* **46**, 2732-2753, doi:10.1039/C7CS00013H (2017).

43 Qiao, J. *et al.* Few-layer Tellurium: one-dimensional-like layered elementary semiconductor with striking physical properties. *Sci Bull* **63**, 159-168, doi:10.1016/j.scib.2018.01.010 (2018).

44 Pant, A. *et al.* Strong dichroic emission in the pseudo one dimensional material ZrS3. *Nanoscale* **8**, 16259-16265, doi:10.1039/c6nr05238j (2016).

45 Dai, J., Li, M. & Zeng, X. C. Group IVB transition metal trichalcogenides: a new class of 2D layered materials beyond graphene. *Wiley Interdisciplinary Reviews: Computational Molecular Science* **6**, 211-222, doi:10.1002/wcms.1243 (2016).

46 Zhao, H. *et al.* Interlayer interactions in anisotropic atomically thin rhenium diselenide. *Nano Research* **8**, 3651-3661, doi:10.1007/s12274-015-0865-0 (2015).

47 Tongay, S. *et al.* Monolayer behaviour in bulk ReS2 due to electronic and vibrational decoupling. *Nat Commun* **5**, 3252, doi:10.1038/ncomms4252 (2014).

48 Aslan, O. B., Chenet, D. A., van der Zande, A. M., Hone, J. C. & Heinz, T. F. Linearly Polarized Excitons in Single- and Few-Layer ReS2 Crystals. *ACS Photonics* **3**, 96-101, doi:10.1021/acsphotonics.5b00486 (2015).

49 Chenet, D. A. *et al.* In-Plane Anisotropy in Mono- and Few-Layer ReS2 Probed by Raman Spectroscopy and Scanning Transmission Electron Microscopy. *Nano Lett* **15**, 5667-5672, doi:10.1021/acs.nanolett.5b00910 (2015).

50 Nagler, P., Plechinger, G., Schüller, C. & Korn, T. Observation of anisotropic interlayer Raman modes in few-layer ReS2. *physica status solidi (RRL) - Rapid Research Letters* **10**, 185-189, doi:10.1002/pssr.201510412 (2016).

51 Wolverson, D., Crampin, S., Kazemi, A. S., Ilie, A. & Bending, S. J. Raman spectra of monolayer, few-layer, and bulk ReSe(2): an anisotropic layered semiconductor. *ACS Nano* **8**, 11154-11164, doi:10.1021/nn5053926 (2014).

52 Chhowalla, M. *et al.* The chemistry of two-dimensional layered transition metal dichalcogenide nanosheets. *Nat Chem* **5**, 263-275, doi:10.1038/nchem.1589 (2013).

53 Duerloo, K. A., Li, Y. & Reed, E. J. Structural phase transitions in two-dimensional Mo- and W-dichalcogenide monolayers. *Nat Commun* **5**, 4214, doi:10.1038/ncomms5214 (2014).

54 Eda, G. *et al.* Photoluminescence from chemically exfoliated MoS2. *Nano Lett* **11**, 5111-5116, doi:10.1021/nl201874w (2011).

55 Fan, X. *et al.* Fast and Efficient Preparation of Exfoliated 2H MoS2 Nanosheets by Sonication-Assisted Lithium Intercalation and Infrared Laser-Induced 1T to 2H Phase Reversion. *Nano Lett* **15**, 5956-5960, doi:10.1021/acs.nanolett.5b02091 (2015).

56 Chhowalla, M., Voiry, D., Yang, J., Shin, H. S. & Loh, K. P. Phase-engineered transition-metal dichalcogenides for energy and electronics. *MRS Bulletin* **40**, 585-591, doi:10.1557/mrs.2015.142 (2015).

57 Mulhern, P. J. Lithium intercalation in crystalline LixMoS2. *Canadian Journal of Physics* **67**, 1049-1052, doi:10.1139/p89-184 (1989).

58 Kertesz, M. & Hoffmann, R. Octahedral vs. trigonal-prismatic coordination and clustering in transition-metal dichalcogenides. *Journal of the American Chemical Society* **106**, 3453-3460, doi:10.1021/ja00324a012 (1984).

59 Sun, X., Wang, Z., Li, Z. & Fu, Y. Q. Origin of Structural Transformation in Mono- and Bi-Layered Molybdenum Disulfide. *Sci Rep* **6**, 26666, doi:10.1038/srep26666 (2016).

60 Kan, M. *et al.* Structures and Phase Transition of a MoS2 Monolayer. *The Journal of Physical Chemistry C* **118**, 1515-1522, doi:10.1021/jp4076355 (2014).

61 Augustin, J. *et al.* Electronic band structure of the layered compoundTd−WTe2. *Physical Review B* **62**, 10812-10823, doi:10.1103/PhysRevB.62.10812 (2000).

62 Chang, T. R. *et al.* Prediction of an arc-tunable Weyl Fermion metallic state in Mo(x)W(1-x)Te2. *Nat Commun* **7**, 10639, doi:10.1038/ncomms10639 (2016).

63 Feng, Y. *et al.* Raman vibrational spectra of bulk to monolayerReS2with lower symmetry. *Physical Review B* **92**, 54110, doi:10.1103/PhysRevB.92.054110 (2015).

64 Mak, K. F., Lee, C., Hone, J., Shan, J. & Heinz, T. F. Atomically thin MoS(2): a new direct-gap semiconductor. *Phys Rev Lett* **105**, 136805, doi:10.1103/PhysRevLett.105.136805 (2010).

65 Keyshar, K. *et al.* Chemical Vapor Deposition of Monolayer Rhenium Disulfide (ReS2). *Adv Mater* **27**, 4640-4648, doi:10.1002/adma.201501795 (2015).

66 Wu, K. *et al.* Domain Architectures and Grain Boundaries in Chemical Vapor Deposited Highly Anisotropic ReS2 Monolayer Films. *Nano Lett* **16**, 5888-5894, doi:10.1021/acs.nanolett.6b02766 (2016).

67 Najmaei, S. *et al.* Vapour phase growth and grain boundary structure of molybdenum disulphide atomic layers. *Nat Mater* **12**, 754-759, doi:10.1038/nmat3673 (2013).

68 Gao, J., Yip, J., Zhao, J., Yakobson, B. I. & Ding, F. Graphene nucleation on transition metal surface: structure transformation and role of the metal step edge. *J Am Chem Soc* **133**, 5009-5015, doi:10.1021/ja110927p (2011).

69 Pohl, U. W. *Epitaxy of Semiconductors*. (2013).

70 Koma, A. Van der Waals epitaxy for highly lattice-mismatched systems. *Journal of Crystal Growth* **201-202**, 236-241, doi:10.1016/s0022-0248(98)01329-3 (1999).

71 Koma, A. Van der Waals epitaxy—a new epitaxial growth method for a highly lattice-mismatched system. *Thin Solid Films* **216**, 72-76, doi:10.1016/0040-6090(92)90872-9 (1992).

72 Zhang, X. *et al.* Vertical heterostructures of layered metal chalcogenides by van der Waals epitaxy. *Nano Lett* **14**, 3047-3054, doi:10.1021/nl501000k (2014).

73 Li, M. Y. *et al.* NANOELECTRONICS. Epitaxial growth of a monolayer WSe2-MoS2 lateral p-n junction with an atomically sharp interface. *Science* **349**, 524-528, doi:10.1126/science.aab4097 (2015).

74 Xie, S. *et al.* Coherent, atomically thin transition-metal dichalcogenide superlattices with engineered strain. *Science* **359**, 1131-1136, doi:10.1126/science.aao5360 (2018).

75 Kolobov, A. V. & Tominaga, J. *Two-Dimensional Transition-Metal Dichalcogenides*. (2016).

76 Magda, G. Z. *et al.* Exfoliation of large-area transition metal chalcogenide single layers. *Sci Rep* **5**, 14714, doi:10.1038/srep14714 (2015).

77 Tan, C. *et al.* Recent Advances in Ultrathin Two-Dimensional Nanomaterials. *Chem Rev* **117**, 6225-6331, doi:10.1021/acs.chemrev.6b00558 (2017).

78 Nicolosi, V., Chhowalla, M., Kanatzidis, M. G., Strano, M. S. & Coleman, J. N. Liquid Exfoliation of Layered Materials. *Science* **340**, 1226419-1226419, doi:10.1126/science.1226419 (2013).

79 Shi, Y., Li, H. & Li, L. J. Recent advances in controlled synthesis of two-dimensional transition metal dichalcogenides via vapour deposition techniques. *Chem Soc Rev* **44**, 2744-2756, doi:10.1039/c4cs00256c (2015).

80 Lin, Z. *et al.* Defect engineering of two-dimensional transition metal dichalcogenides. *2D Materials* **3**, 22002, doi:10.1088/2053-1583/3/2/022002 (2016).

81 Ferraro, J. R., Nakamoto, K. & Brown, C. W. in *Introductory Raman Spectroscopy* (eds John R. Ferraro, Kazuo Nakamoto, & Chris W. Brown) 1-94 (Academic Press, 2003).

82 Larkin, P. in *Infrared and Raman Spectroscopy* (ed Peter Larkin) 7-25 (Elsevier, 2011).

83 Fox, M. *Optical properties of solids*. (Oxford University Press, 2001).

84 Yang, J. C., Small, M. W., Grieshaber, R. V. & Nuzzo, R. G. Recent developments and applications of electron microscopy to heterogeneous catalysis. *Chem Soc Rev* **41**, 8179-8194, doi:10.1039/c2cs35371g (2012).

85 Williams, D. B. & Carter, C. B. Transmission electron microscopy: a textbook for materials science. *Transmission electron microscopy: a textbook for materials science*, doi:10.1007/978-0-387-76501-3 (2009).

86 Pennycook, S. J. *et al.* in *Scanning Microscopy for Nanotechnology* (eds Weilie Zhou & Zhong Lin Wang) Ch. Chapter 6, 152-191 (Springer New York, 2006).

87 Egerton, R. F. Control of radiation damage in the TEM. *Ultramicroscopy* **127**, 100-108, doi:10.1016/j.ultramic.2012.07.006 (2013).

88 Egerton, R. F. Mechanisms of radiation damage in beam-sensitive specimens, for TEM accelerating voltages between 10 and 300 kV. *Microsc Res Tech* **75**, 1550-1556, doi:10.1002/jemt.22099 (2012).

89 Komsa, H. P. *et al.* Two-dimensional transition metal dichalcogenides under electron irradiation: defect production and doping. *Phys Rev Lett* **109**, 035503, doi:10.1103/PhysRevLett.109.035503 (2012).

90 Carter, C. B. & Williams, D. B. *Transmission Electron Microscopy*. (2016).

91 Jalili, N. & Laxminarayana, K. A review of atomic force microscopy imaging systems: application to molecular metrology and biological sciences. *Mechatronics* **14**, 907-945, doi:10.1016/j.mechatronics.2004.04.005 (2004).

92 Zhang, H. *et al.* Atomic force microscopy for two-dimensional materials: A tutorial review. *Optics Communications* **406**, 3-17, doi:10.1016/j.optcom.2017.05.015 (2018).

93 Rahman, M., Davey, K. & Qiao, S. Z. Advent of 2D Rhenium Disulfide (ReS2): Fundamentals to Applications. *Advanced Functional Materials*, 1606129, doi:10.1002/adfm.201606129 (2017).

94 Hart, L., Dale, S., Hoye, S., Webb, J. L. & Wolverson, D. Rhenium Dichalcogenides: Layered Semiconductors with Two Vertical Orientations. *Nano Lett* **16**, 1381-1386, doi:10.1021/acs.nanolett.5b04838 (2016).

95 He, R. *et al.* Coupling and Stacking Order of ReS2 Atomic Layers Revealed by Ultralow-Frequency Raman Spectroscopy. *Nano Lett* **16**, 1404-1409, doi:10.1021/acs.nanolett.5b04925 (2016).

96 Hafeez, M., Gan, L., Li, H., Ma, Y. & Zhai, T. Large-Area Bilayer ReS2

Film/Multilayer ReS2

Flakes Synthesized by Chemical Vapor Deposition for High Performance Photodetectors. *Advanced Functional Materials* **26**, 4551-4560, doi:10.1002/adfm.201601019 (2016).

97 Duesberg, G. S. Heterojunctions in 2D semiconductors: A perfect match. *Nat Mater* **13**, 1075-1076, doi:10.1038/nmat4127 (2014).

98 Wang, K. *et al.* Interlayer Coupling in Twisted WSe2/WS2 Bilayer Heterostructures Revealed by Optical Spectroscopy. *ACS Nano*, doi:10.1021/acsnano.6b01486 (2016).

99 Su, W., Dou, H., Huo, D., Dai, N. & Yang, L. Enhancing photoluminescence of trion in single-layer MoS2 using p-type aromatic molecules. *Chemical Physics Letters* **635**, 40-44, doi:10.1016/j.cplett.2015.06.036 (2015).

100 Zhang, T. *et al.* Twinned growth behaviour of two-dimensional materials. *Nat Commun* **7**, 13911, doi:10.1038/ncomms13911 (2016).

101 Yuan, Q., Yakobson, B. I. & Ding, F. Edge-Catalyst Wetting and Orientation Control of Graphene Growth by Chemical Vapor Deposition Growth. *J Phys Chem Lett* **5**, 3093-3099, doi:10.1021/jz5015899 (2014).

102 Berkdemir, A. *et al.* Identification of individual and few layers of WS2 using Raman Spectroscopy. *Scientific Reports* **3**, 1755, doi:10.1038/srep01755 (2013).

103 Elias, A. L. *et al.* Controlled synthesis and transfer of large-area WS2 sheets: from single layer to few layers. *ACS Nano* **7**, 5235-5242, doi:10.1021/nn400971k (2013).

104 He, Z. *et al.* Biexciton Formation in Bilayer Tungsten Disulfide. *ACS Nano* **10**, 2176-2183, doi:10.1021/acsnano.5b06678 (2016).

105 Lin, Y. C. *et al.* Single-Layer ReS(2): Two-Dimensional Semiconductor with Tunable In-Plane Anisotropy. *ACS Nano* **9**, 11249-11257, doi:10.1021/acsnano.5b04851 (2015).

106 Zhu, B., Chen, X. & Cui, X. Exciton binding energy of monolayer WS(2). *Sci Rep* **5**, 9218, doi:10.1038/srep09218 (2015).

107 Tizei, L. H. *et al.* Exciton mapping at subwavelength scales in two-dimensional materials. *Phys Rev Lett* **114**, 107601, doi:10.1103/PhysRevLett.114.107601 (2015).

108 Hong, X. *et al.* Ultrafast charge transfer in atomically thin MoS(2)/WS(2) heterostructures. *Nat Nanotechnol* **9**, 682-686, doi:10.1038/nnano.2014.167 (2014).

109 Barthel, J. Dr. Probe: A software for high-resolution STEM image simulation. *Ultramicroscopy* **193**, 1-11, doi:10.1016/j.ultramic.2018.06.003 (2018).

110 Wen, W. *et al.* Anisotropic Spectroscopy and Electrical Properties of 2D ReS2(1-x) Se2x Alloys with Distorted 1T Structure. *Small* **13**, 1603788, doi:10.1002/smll.201603788 (2017).

111 Pierson, H. O. *Handbook of chemical vapor deposition: principles, technology and applications*. (William Andrew, 1999).

112 Tongay, S. *et al.* Broad-range modulation of light emission in two-dimensional semiconductors by molecular physisorption gating. *Nano Lett* **13**, 2831-2836, doi:10.1021/nl4011172 (2013).

113 Shengjie, G., Yixiu, W., Ruoxing, W. & Wenzhuo, W. Piezotronic effect in 1D van der Waals solid of elemental tellurium nanobelt for smart adaptive electronics. *Semiconductor Science and Technology* **32**, 104004 (2017).

114 Ikari, T., Berger, H. & Levy, F. Electrical properties of vapour grown tellurium single crystals. *Materials Research Bulletin* **21**, 99-105, doi:10.1016/0025-5408(86)90035-8 (1986).

115 Weihong, X. *et al.* Structural, Electrical, and Photoconductive Properties of Individual Single‐Crystalline Tellurium Nanotubes Synthesized by a Chemical Route: Doping Effects on Electrical Structure. *Small* **4**, 888-893, doi:doi:10.1002/smll.200701227 (2008).

116 Royer, D. & Dieulesaint, E. Elastic and piezoelectric constants of trigonal selenium and tellurium crystals. *Journal of Applied Physics* **50**, 4042-4045, doi:10.1063/1.326485 (1979).

117 Peng, H., Kioussis, N. & Snyder, G. J. Elemental tellurium as a chiral p-type thermoelectric material. *Physical Review B* **89**, 195206, doi:10.1103/PhysRevB.89.195206 (2014).

118 Dun, C. *et al.* Flexible thermoelectric fabrics based on self-assembled tellurium nanorods with a large power factor. *Physical Chemistry Chemical Physics* **17**, 8591-8595, doi:10.1039/C4CP05390G (2015).

119 Lin, S. *et al.* Tellurium as a high-performance elemental thermoelectric. *Nature Communications* **7**, 10287, doi:doi:10.1038/ncomms10287 (2016).

120 Hippel, A. v. Structure and Conductivity in the VIb Group of the Periodic System. *The Journal of Chemical Physics* **16**, 372-380, doi:10.1063/1.1746893 (1948).

121 Mayers, B. & Xia, Y. One-dimensional nanostructures of trigonal tellurium with various morphologies can be synthesized using a solution-phase approach. *Journal of Materials Chemistry* **12**, 1875-1881, doi:10.1039/B201058E (2002).

122 He, Z., Yu, S.-H. & Zhu, J. Amino Acids Controlled Growth of Shuttle-Like Scrolled Tellurium Nanotubes and Nanowires with Sharp Tips. *Chemistry of Materials* **17**, 2785-2788, doi:10.1021/cm0503228 (2005).

123 Sen, S. *et al.* Synthesis of Tellurium Nanostructures by Physical Vapor Deposition and Their Growth Mechanism. *Crystal Growth & Design* **8**, 238-242, doi:10.1021/cg070185m (2008).

124 Métraux, C. & Grobéty, B. Tellurium nanotubes and nanorods synthesized by physical vapor deposition. *Journal of Materials Research* **19**, 2159-2164, doi:10.1557/JMR.2004.0277 (2011).

125 Wang, Q. *et al.* Van der Waals Epitaxy and Photoresponse of Hexagonal Tellurium Nanoplates on Flexible Mica Sheets. *ACS Nano* **8**, 7497-7505, doi:10.1021/nn5028104 (2014).

126 Huang, X. *et al.* Epitaxial Growth and Band Structure of Te Film on Graphene. *Nano Letters* **17**, 4619-4623, doi:10.1021/acs.nanolett.7b01029 (2017).

127 Chen, J. *et al.* Ultrathin [small beta]-tellurium layers grown on highly oriented pyrolytic graphite by molecular-beam epitaxy. *Nanoscale* **9**, 15945-15948, doi:10.1039/C7NR04085G (2017).

128 Cai, H. *et al.* Synthesis of Highly Anisotropic Semiconducting GaTe Nanomaterials and Emerging Properties Enabled by Epitaxy. *Advanced Materials* **29**, 1605551, doi:10.1002/adma.201605551 (2017).

129 Yang, S. *et al.* Self-Driven Photodetector and Ambipolar Transistor in Atomically Thin GaTe-MoS2 p–n vdW Heterostructure. *ACS Applied Materials & Interfaces* **8**, 2533-2539, doi:10.1021/acsami.5b10001 (2016).

130 Yamamoto, A. *et al.* Excitons and band structure of highly anisotropic GaTe single crystals. *Physical Review B* **64**, 035210 (2001).

131 Yang, S. *et al.* Environmental stability of 2D anisotropic tellurium containing nanomaterials: anisotropic to isotropic transition. *Nanoscale* **9**, 12288-12294, doi:10.1039/C7NR02397A (2017).

132 Wang, S. *et al.* Shape Evolution of Monolayer MoS2 Crystals Grown by Chemical Vapor Deposition. *Chemistry of Materials* **26**, 6371-6379, doi:10.1021/cm5025662 (2014).

133 Cao, D., Shen, T., Liang, P., Chen, X. & Shu, H. Role of Chemical Potential in Flake Shape and Edge Properties of Monolayer MoS2. *The Journal of Physical Chemistry C* **119**, 4294-4301, doi:10.1021/jp5097713 (2015).

134 Naylor, C. H. *et al.* Synthesis and Physical Properties of Phase-Engineered Transition Metal Dichalcogenide Monolayer Heterostructures. *ACS Nano* **11**, 8619-8627, doi:10.1021/acsnano.7b03828 (2017).